Title

Microfluidics for blood component separation, medium exchange, response latency measurements, and single molecule fluorescence microscopy

Author

VanDelinder, Virginia Alison

Publication Date

2009

Peer reviewed|Thesis/dissertation

UNIVERSITY OF CALIFORNIA, SAN DIEGO

Microfluidics for blood component separation, medium exchange, response latency measurements, and single molecule fluorescence microscopy

A dissertation submitted in partial satisfaction of the
requirements for the degree
Doctor of Philosophy

in

Physics (Biophysics)

by

Virginia Alison VanDelinder

Committee in charge:

Professor Alex Groisman, Chair
Professor Patrick Diamond
Professor Olga Dudko
Professor Eric Lauga
Professor Efim Zelmanov

2009

The dissertation of Virginia Alison VanDelinder is approved, and it is acceptable in quality and form for publication on microfilm:

Chair

University of California, San Diego

2009

TABLE OF CONTENTS

LIST OF FIGURES

LIST OF TABLES

ACKNOWLEDGEMENTS

I would like to thank my advisor, Dr. Alex Groisman, for his support and for everything he taught me about being an experimentalist. I would like to thank my committee members for all of their patience, support, and encouragement. I would like to thank the graduate students and post docs in the Groisman lab, J. Kyle Campbell, Claire Simonnet, Edgar Gutierrez, Micha Adler, and Mark Polinkowski, for their help and friendship. I would like to thank my collaborators in the group of Ashok Deniz at the Scripps Research Institute: Yann Gambin for his friendship, sharing his ideas, and making science exciting; Edward Lemke, for his tenacity and for teaching me about single molecule fluorescence microscopy; and Allan Ferreon for the most meticulously prepared protein samples. I would like to thank the faculty of the UCSD Physics Department for their support, encouragement, and excellent teaching. Professors Hwa and Diamond, in particular, taught many fascinating, challenging classes. Grad school would have been an entirely different place without the friends I made here, especially Aleksandra Walczak for all the good advice and long walks; Jacob Stevenson and Chad Kishimoto, the best homework and tennis buddies; and Paul Whitford. I am truly appreciative of my family for their love, encouragement, and understanding. Finally, I would like to thank my husband Nathan for his love and support.

Chapter 2.1, in full, is a reprint of the journal article Separation of plasma from whole human blood in a continuous cross-flow in a molded microfluidic device, Analytical Chemistry, 2006. VanDelinder, Virginia; Groisman, Alex. Dissertation author was the first author and a leading contributor of this paper.

Chapter 2.2, in full, is a reprint of the journal article Perfusion in microfluidic cross-flow: separation of white blood cells from whole blood and exchange of medium in a continuous flow, Analytical Chemistry, 2007. VanDelinder, Virginia; Groisman, Alex. Dissertation author was the first author and a leading contributor of this paper.

Chapter 3, in full, is a reprint of the journal article Bioluminescent response of individual dinoflagellate cells to hydrodynamic stress measured with millisecond resolution in a microfluidic device in Journal of Experimental Biology, 2008. Latz, Michael; Bovard, Michelle; VanDelinder, Virginia; Segre, Enrico; Rohr, Jim; Groisman, Alex. Dissertation

author was a participating investigator of this paper.

Chapter 4.1 is in preparation for publication in Microfluidic device for single-molecule fluorescence experiments with high photostability. Lemke, Edward*; Gambin, Yann*; Vandelinder, Virginia*; Brustad, Eric; Schultz, Peter; Groisman, Alex; Deniz, Ashok. Dissertation author was one of the principal investigators of this paper.

Chapter 4.2 is in preparation for publication in Non-reversible folding pathway in a-Synuclein revealed in a single-molecule microfluidic mixer. Gambin, Yann; Ferreon, Allan; VanDelinder, Virginia; Lemke, Edward; Groisman, Alex; Deniz, Ashok. Dissertation author was a participating investigator of this paper.

VITA

2001	Bachelor of Science in Physics and Mathematics, New Mexico Institute of Mining and Technology, Socorro
2003-2004	Graduate Teaching Assistant, Physics Department, University of California, San Diego
2005	Master of Science in Physics, University of California, San Diego
2004-2009	Graduate Research Assistant, Physics Department, University of California, San Diego
2009	Doctor of Philosophy in Physics (Biophysics), University of California, San Diego

PUBLICATIONS

K. Minschwaner, V. Starke, "Photodissociation of nitric oxide in the middle and upper atmosphere", *Physics and Chemistry of the Earth*, **29**, 2001.

V. VanDelinder, A. Groisman, "Separation of plasma from whole human blood in a continuous cross-flow in a molded microfluidic device", *Analytical Cemistry*, **78**, 2006.

V. VanDelinder, A. Groisman, "Perfusion in microfluidic cross-flow: separation of leukocytes from whole blood and exchange of medium in a continuous flow", *Analytical Cemistry*, **79**, 2007.

M. Latz, M. Bovard, V. VanDelinder, E. Segre, J. Rohr, A. Groisman, "Bioluminescent response of individual dinoflagellate cells to hydrodynamic stress measured with millisecond resolution in a microfluidic device", *Journal of Experimental Biology*, **211**, 2008.

ABSTRACT OF THE DISSERTATION

Microfluidics for blood component separation, medium exchange, response latency measurements, and single molecule fluorescence microscopy

by

Virginia Alison VanDelinder

Doctor of Philosophy in Physics (Biophysics)

University of California San Diego, 2009

Professor Alex Groisman, Chair

Recent years have seen considerable development of microscale fluid handling systems for use in chemistry and biology. These microfluidic devices offer many advantages over their macroscale counterparts, including better control of experiment parameters and much smaller sample and reagent usage. With the advent of rapid-prototyping techniques, testing new microchannel designs is quick and inexpensive.

Highly integrated microdevices have applications in basic biomedical and pharmaceutical research, as well as in robust and portable point-of-care systems that could be used in clinical settings. In this dissertation, I describe the development of microfluidic devices to perform sample preparation crucial for many point-of-care systems that require separation of blood components. Another application presented is a microfluidic platform that exploits precise flow control to measure the response latency of bioluminescent dinoflagellates.

The precise fluid manipulation possible in microfluidics also offers much potential to expand the reach of single molecule techniques. Two microfluidic tools to improve single molecule fluorescence studies of protein folding are presented: a device for sample deoxygenation and rapid buffer exchange designed to increase photostability and circumvent sample sticking issues; and a device for rapid medium exchange for ultrafast protein folding

kinetics measurements.

Chapter 1

Introduction

Microfluidics is the science of systems that manipulate fluids in channels with dimension on the scale of micrometers.[Whi06] Microfluidics is a very interdisciplinary field at the intersection of physics, engineering, biology, and chemistry. The field has rapidly expanded since its beginning in the late 1980's as an offshoot from microelectronics and micro-electrical-mechanical systems (MEMS). Indeed, most of the early fabrication techniques and materials were borrowed directly from those fields. The introduction of fluid channels to MEMS devices opened up many new areas of research, especially in biology.[SQ05, Whi06, Bru08]

The boom in microfluidics in the recent years was facilitated by the development of soft lithography and rapid prototyping. By making soft plastic replicas of a lithographically-fabricated master mold, many copies of a device can be produced quickly and cheaply in a small lab space. The rapidity of soft lithography enables researchers to go from idea to device in just a few days. In contrast, the hard materials common in MEMS and microelectronics, such as silicon and glass, are time consuming and expensive to micromachine.[SW03, Whi06, KKP$^+$08]

One of the most popular materials in microfluidics, the silicon elastomer polydimethylsiloxane (PDMS), is especially suited to applications with live cells due to its biocompatibility, chemical inertness, and air permeability. Because PDMS is optically clear,

has low autofluorescence, and can seal reversibly with microscope glass cover slips, PDMS devices are compatible with standard microscopes. The small volumes inherent to microfluidics are attractive for applications with expensive or otherwise limited amounts of sample and reagents. The flexibility of PDMS makes it possible to incorporate on-chip valves for precise flow control.[MDA$^+$00, UCT$^+$00, SW03, Whi06]

Microfluidics can be used both to study physical phenomena that occur in microchannels and as precise tool to facilitate the study of other fields, such as biology and biochemistry. Careful microchannel design and utilization of the properties of laminar flow make it possible to precisely control the location of cells in the microfluidic device and the medium conditions around the cells.[EAGG$^+$05] Completely novel experiments are possible that go far beyond simple miniaturization of macroscale techniques.[Cra06, deM06, JFM06] A major application of microfluidics is the development of lab on a chip and point of care diagnostics, which are handheld systems that can perform all the sample preparation, processing, and detection steps in one unit.[EAGG$^+$05, YEF$^+$06]

The work presented in this thesis is directed at the creation of microfluidic devices to perform sample preparation steps and to enable novel biological experiments. The first two projects presented focus on separating blood components, which is a necessary step for many types of blood tests. The third project uses a microfluidic device to study the response latency of dinoflagellate luminescence at a single cell level under precisely controlled flow conditions. The final two projects use microfluidics to make better tools for single-molecule fluorescence microscopy. In the introduction, background common to all the projects is presented: fluid flow in microchannels, device design, fabrication techniques, and a general description of an experimental setup. Then background specific to the Chapter 4 is presented: proteins, protein folding, the protein αS, and single molecule fluorescence microscopy.

1.1 Fluid flow in microchannels

The Navier Stokes equation, $\partial_t \mathbf{v} + (\mathbf{v} \cdot \nabla)\mathbf{v} = -\nabla p/\rho + \nu \nabla^2 \mathbf{v}$, which is Newton's second law as applied to fluids, together with the continuity equation, $\nabla \cdot \mathbf{v} = 0$, are the most fundamental equations in fluid dynamics (both equations are given in the form for incompressible fluids). It is possible to make the Navier Stokes equation dimensionless by expressing the physical quantities in terms of a characteristic length and velocity scale, L_0 and V_0. Then it becomes, $Re(\tilde{\partial}_t \tilde{\mathbf{v}} + (\tilde{\mathbf{v}} \cdot \tilde{\nabla})\tilde{\mathbf{v}}) = -\tilde{\nabla}\tilde{p} + \tilde{\nabla}^2 \tilde{\mathbf{v}}$, where $Re \equiv L_0 V_0/\nu$ is the dimensionless Reynolds number. When $Re \gg 1$, the inertial term $(\tilde{\mathbf{v}} \cdot \tilde{\nabla})\tilde{\mathbf{v}}$ dominates, and turbulence can occur. When $Re \ll 1$, the viscous term $\tilde{\nabla}^2 \tilde{\mathbf{v}}$ term dominates, and flow is laminar. For a typical microfluidic channel, $L_0 \sim 10\mu m$, $V_0 \sim 1mm/s$, and $\nu \sim 1mm^2/s$ (the kinematic viscosity), resulting in $Re \sim 10^{-2}$. Consequently, fluid flows in microchannels are generally laminar and stable. However, even in microchannels, flow speeds of $> 1m/s$ can result in $Re > 1$, leading to substantial inertial effects and changes in flow patterns.

The most common situation in microfluidics is a steady low Re flow in a channel with a rectangular cross section driven solely by an applied pressure difference. This type of flow is called Poisueille flow, where the non-linear Navier Stokes equation becomes a linear Stokes equation $\nabla p/\rho + \nu \nabla^2 \mathbf{v} = 0$. Assuming our channel is oriented lengthwise in the x-direction, since there is no pressure drop in the y or z direction, only the x component of the velocity is nonzero. For a channel with a width w, height h, and pressure drop ΔP in length L, the Navier-Stokes equation with no-slip boundary conditions then becomes

$$\begin{aligned} \left[\partial_y^2 + \partial_z^2\right] v_x(y,z) = -\frac{\Delta p}{\eta L}, \qquad & \text{for } -\frac{1}{2}w < y < \frac{1}{2}, 0 < z < h, \\ v_x(y,z) = 0, \qquad & \text{for } y = \pm\frac{1}{2}w, z = 0, z = h, \end{aligned} \tag{1.1}$$

where η is the dynamic viscosity. Despite the symmetry of boundary, no analytical solution is known; the best that can be done is to represent the solution as a Fourier series. Solving these equations for the velocity in the x direction as a function of y and z, we find

$$v_x(y,z) = \frac{4h^2 \Delta p}{\pi^3 \eta L} \sum_{n,odd}^{\infty} \frac{1}{n^3} \left[1 - \frac{\cosh(n\pi y/h)}{\cosh(n\pi w/(2h))}\right] \sin(n\pi z/h), \tag{1.2}$$

where it is assumed that $w > h$, which can always be achieved by rotation. This solution is shown in Fig. 1.1. We can integrate the velocity to find the volumetric flow rate,

$$Q = 2\int_0^{w/2} dy \int_0^h dz v_x(y,z) = \frac{h^3 w \Delta p}{12\eta L}\left[1 - \sum_{n,odd}^{\infty} \frac{192h}{n^5\pi^5 w} \tanh\left(n\pi\frac{w}{2h}\right)\right] \tag{1.3}$$

This equation can be grouped using

$$k = 1 - \sum_{n,odd}^{\infty} \frac{192h}{n^5\pi^5 w} \tanh\left(n\pi\frac{w}{2h}\right), \tag{1.4}$$

where k is solely a function of the aspect ratio w/h. Then the volumetric flow rate becomes $Q = h^3 w k \Delta p/(12\eta L)$. This is one of the most useful equations for designing microfluidic devices. It is often written as $Q = \Delta p/R$, where $R = 12\eta L/(h^3 w k)$ is the hydraulic resistance, simply called resistance from here on out.[DMB56, Bru08]

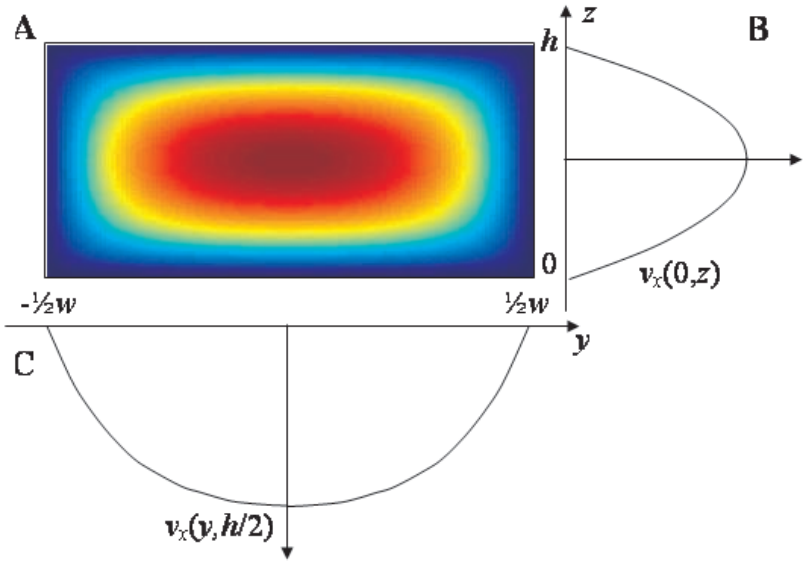

Figure 1.1: Velocity profile in a microchannel with a rectangular cross-section. A) Contour plot of the velocity field $v_x(y,z)$, in a rectangular channel of height h and width w. B) Plot of $v_x(0,z)$. C) Plot of $v_x(y,h/2)$.

For two channels connected in series, Q is the same through each channel and the pressure drops are additive, hence the resistances are also additive, $R_{\text{total}} = R_1 + R_2$. For channels in parallel, the pressure drop along each channel is the same, and $Q_{\text{total}} = Q_1 + Q_2$. We then find $R_{\text{total}} = \left(R_1^{-1} + R_2^{-1}\right)^{-1}$. (These relations are only valid for low Re and long narrow channels.)

Diffusion is often an important consideration in microfluidics. Using a one dimensional random walk model, it can be shown that the distance x a molecule will diffuse in time t is $x = \sqrt{Dt}$, where D is the diffusion coefficient. In two dimensions, $x = \sqrt{2Dt}$. Typical value of D and the corresponding times to diffuse across a distance $x = 100\mu m$ in water are the following:

$D \sim 2 \times 10^{-9} m^2/s,$	$t \sim 5s,$	for small ions,
$D \sim 7 \times 10^{-12} m^2/s,$	$t \sim 23min,$	2 MDa dextran molecule

In cases where there is both diffusion and convection, such as when fluid streams with different solutes are flowing side-by-side through a channel, it is instructive to compare the characteristic time of convection, $\tau_{\text{conv}} = L/v$, to the characteristic time of diffusion, $\tau_{\text{diff}} = w^2/4D$, where L is the length of the channel, v is the average velocity of fluid flow through the channel, and w is the channel width. If $\tau_{\text{diff}} \gg \tau_{\text{conv}}$, the solutes almost completely stay in the original streams. If $\tau_{\text{diff}} > \tau_{\text{conv}}$, the solutes will diffuse all the way across the channel, and the streams will be mixed.[Bru08]

1.2 Basic microfluidic device design

The main equations necessary to design a microfluidic device were presented in the previous section. In many ways, device design is an underdetermined problem, with multiple viable solutions. There are two types of constraints on designing a microfluidic device: ones from the fabrication techniques and ones that are self-imposed for the specific application. With soft lithography fabrication, channels can be produced with depths ranging from 250 μm to 0.5 μm. It is difficult to make channels with depth/width ratios of more than 5. The microchannel width can be made as small as 1 - 2 μm, but unless truly necessary for the application, to minimize the costs and time of fabrication, it is highly preferable to have microchannel widths larger than 5 μm. Channels and chambers that are very wide and shallow (aspect ratio $\geq$ 20) are prone to collapse. Many applications require two different depths of channels. More rarely are three depths needed, but beyond that is not prudent in terms of fabrication. A driving pressure from 5 cm water to 4 psi is practical. Inlets and outlets must be located at least 3 mm apart.

In applications involving high-resolution microscopy, it is important to match the size of the channels with the field of view of a video-microscopy system, including the light source, microscope objective, video-relay lens, and camera, in order to provide sufficient optical and pixelate resolution and sufficient level of (fluorescence) light. In applications with cells, the cell size imposes obvious constraints on the depth and width of the channels. The presence of cells quite often puts limits on the flow velocity, since the shear stress at higher flow rates can damage cells. Velocity constraints frequently arise from a need for flow to be slow enough for diffusive mixing to occur, or contrarily, fast enough that diffusive mixing does not occur, depending on the application. Once channel dimensions and flow velocity are determined, the lengths of the channels are adjusted to get the pressure drop in the desired range (optimally, in the middle of it) using the equations from the preceding section.

The equations are very useful for approximating the resistance of simple networks of channels; however, especially with non-rectangular channels and more complicated network configurations, the flow through the designed microchannels should be modeled with

finite element software. It is also useful to make multiple designs of the device with somewhat varying parameters, such as channel resistance or shape. The fabrication process is not exact, so resistance always differs somewhat from planned, and one is more likely to get the desired effect if a range of versions of the device are made.

1.3 Device fabrication

I used standard soft lithography techniques to fabricate devices. The basic flow of fabrication is shown in Fig. 1.2. Essentially, a drawing of the device is transferred to a photomask. One or more photomasks are used to make an epoxy pattern on a flat silicon master mold. The microfluidic device is a PDMS replica of the master mold.

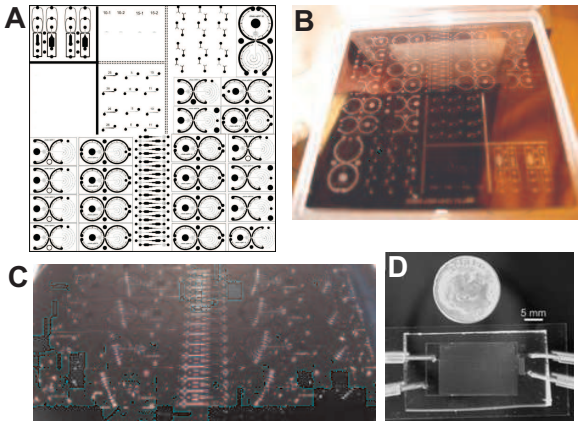

Figure 1.2: The device fabrication process. A) A drawing of a set of devices. B) A photomask printed from the drawings in (A). C) A patterned epoxy relief on silicon master mold. D) A PDMS device created by casting a master mold.

Drawings of the desired device are made using computer drawing or drafting software. Although we use Freehand (Adobe, San Jose, California), I would recommend SolidWorks (Dassault Systmes SolidWorks Corp., Concord, Massachusetts) because drawings can be imported directly into FEMLAB (COMSOL, California), the most common finite element modeling software for microfluidics. The drawings are sent via email to a company that photo-plots the designs onto transparencies at high resolution, up to 50,000 dpi, which is sufficient for 5 μm minimum feature size. Smaller design features can be achieved with a chrome mask, which can support a minimum feature size of 2 μm, although at a significantly increased cost ($400 for a 4" by 4" area, versus $35-130 for a 20" by 10" area transparency). If the designed device has channels of more than one depth, a separate mask is used for each depth and alignment marks are placed on the masks to assure that the channels are created

with the desired orientation and placement with respect to each other. The photomask, either transparency or chrome, is the only fabrication step done outside the lab.

In the next step of the fabrication, the photomask is used to make an epoxy on silicon master mold. First, a layer of photoresist is spin-coated onto a polished silicon wafer. The thickness of the layer can be precisely controlled by selecting appropriate type of photoresist and coating speed. Thicknesses from less than 0.5 μm up to 250 μm are achievable. The wafer with a layer of uncured epoxy is baked on a hot plate first at 65 °C and then at 95 °C (called a pre-bake), with the baking time depending on the photoresist type and thickness. The photoresist on the wafer is then placed in contact with the printed side of the photomask. The wafer is exposed to UV light through the photomask. The wafer is then post-baked on the hot plate at 65 °C and 95 °C and then uncured resist is removed with a developer.

There are 2 types of photoresist: positive and negative. With positive photoresists, the areas that were exposed to UV radiation are washed away in the developing solution. With negative photoresists, such as UV-curable epoxies of the SU8 family, areas that were not exposed are washed away and areas that were exposed become a sturdy cross-linked material. Positive photoresists are necessary for certain applications where channels with rounded cross sections are desired, as in microfluidic devices with integrated membrane valves. Otherwise, negative photoresist is generally used, because more thickness options are available and because multi-level patterns are easy to implement. In addition, negative resists produce features with nearly rectangular cross-sections that are more amenable to flow modeling, and the fidelity and reproducibility of fabrication with the UV-curable epoxies is generally better. The choice of the photoresist must be made at the photomaks design stage, since it determines whether the channels in the device will appear clear with an opaque background (for use with a negative photoresist) or opaque with a clear background (positive photoresist). The devices in this work generally used a negative photoresist from SU8 family.

In order to make master molds with relief features of more than one thickness for multiple channel depths, another layer of photoresist is spin-coated on top of the existing layer. The wafer is once again pre-baked. The photomask for the second layer is aligned

with respect to pattern of the first layer before being exposed to UV light. The wafer is then post-baked and developed to remove excess photoresist. More iterations are possible, but practically, three channel depths are sufficient for almost all designs. There is some error in each alignment, $\sim$10 μm in x and y, and it is prudent to take this into account when designing devices with more than one channel depth. The finished master mold is often baked in a 150 °C oven for 1 hr to increase adhesion between the epoxy and silicon. The surface of the master mold is also passivated by exposure to vapor of trichloromethylsiloxane (TCMS).

The final step of the fabrication process is making a PDMS replica of the master mold. PDMS pre-polymer is made by mixing together two liquid components, a base and a crosslinking agent. Although the manufacturer recommended ratio is 1:10, other ratios are sometimes used when making devices with multiple layers of PDMS stacked atop each other. The liquid PDMS pre-polymer is poured onto the master mold, the PDMS is degassed to remove bubbles, and the whole thing is baked in an 80 °C oven for $\sim$1 hr to quicken the curing of the pre-polymer into a solid. Once cured, the PDMS is gently peeled off of the master mold. The PDMS is cut into "chips" that will conveniently fit on a microscope cover glass; each chip contains one to several devices. Holes for access ports to the channels are punched using a sharpened luer stub. The chips are hermetically sealed to glass cover slips by baking in an 80 °C oven for 1 hr to 1 day.

The preceding description applies to devices with a single channel layer. However, for many applications it is useful to have two layers of channels separated by a PDMS membrane. This configuration is of particular use for incorporating membrane valves or circulation channels for gas or temperature control. To make such devices, two separate master molds are fabricated, one for the layer of channels exposed on the chip surface (flow layer) and one for the layer embedded in the chip (control layer). A replica of the control layer is made as described previously, but with a 1:5 base to crosslinker ratio. The PDMS chips are cut apart and holes are punched. Simultaneously, a thin layer of PDMS (1:20 base to crosslinker ratio) is spin-coated onto the flow layer master mold and then placed in a 80 °C oven until the PDMS is solid, but still tacky, typically $\sim$20 min. Using alignment marks, the control layer chips are placed precisely on top of the PDMS on the flow layer master

mold, and the conglomerate is baked at 80 °C for several hours to produce a two-layer monolith chip. The chips are then trimmed and peeled off the master mold. Holes for the ports in the flow layer are punched, and the chips are bonded to cover slips.

For some applications, it is useful to have PDMS on all sides of the channel. To achieve this, cover slips are spin-coated with a thin layer of PDMS and baked at 80 °C for 1 hr. After experiments, devices can be separated from cover slips, washed, and rebonded to new cover slips for reuse.

1.4 Standard experimental setup

For most of the experiments presented in this work, the device characterization and often the experiments themselves are carried out on either a Nikon TE2000 or TE300 inverted fluorescence microscope. The microscopes are equipped with a tungsten lamp for brightfield illumination and either a mercury lamp or an LED for fluorescence illumination. Images of device channels are recorded with a digital CCD camera.

Liquids fed to the device and drawn off from them are kept either in modified plastic syringes, which are held vertically with their luer connectors down, or in upright microcentrifuge tubes. Both syringes and tubes are connected to microfluidic devices through plastic tubing. The microcentrifuge tubes are sealed with PDMS stoppers with two holes in them. One hole holds tubing that hangs down into the fluid, and a luer stub is inserted in the other hole to connect to a source of pressurized air. The tubing is inserted directly into the ports of the device. Fluid flow is driven by either hydrostatic pressure or air pressure. For hydrostatic pressure, the vessels containing fluids fed to the inlets of the device are raised with respect to the outlet vessels. Both inlet and outlet vessels are kept above the level of the device to avoid bubble creation by negative pressure. In addition, the interior of both syringes and tubes can be pressurized by connecting them to sources of compressed air with pressure regulators.

1.5 Proteins

1.5.1 Protein folding

Researchers in biology, chemistry, and physics have spent decades studying how an unfolded polypeptide chain becomes a natively folded and functional protein [Dob03, OW04, JR05, OW05]. In the late 1980's, Wolynes and Bryngelson introduced the use of statistical mechanical theory of spin glasses to explain protein folding. Other researchers elaborated upon this to develop the current prevalent view of protein folding as comformational diffusion on a funneled energy landscape. The depth of the funnel represents the free energy of a conformational state, and the width is a measure of the comformational entropy. In this approach [BW87, BOSW95, DC97], the folding of a protein encompasses distributions of folding trajectories through different conformations, rather than a single folding pathway. This theoretical description has proved very apt, but advancements in the experimental techniques used to study protein folding continue to reveal conceptual surprises.

An intriguing finding in recent years that goes against the standard dogma is that the final structure of a protein is not solely determined by its amino acid sequence. Called intrinsically disordered proteins (IDP), this new class of proteins will only fold in the presence of binding partners, so the final 3D structure of the protein is encoded by a combination of the protein sequence and its binding partner(s). Even more strikingly, it has been shown in some cases that alternate binding partners induce alternate folded conformations in the same IDP [DMYDG$^+$02, EHM$^+$03]. IDPs are estimated to comprise up to 30% of the human genome. They have been discovered in various contexts, including signal transduction and amyloid formation [DCR$^+$05]. Amyloids are fibrous protein aggregates.

In addition to being important from a basic scientific standpoint, protein misfolding and amyloid formation have been implicated in multiple diseases, including Alzheimer's, Parkinson's, and Huntington's diseases and type II diabetes [CD06]. Therefore, there is significant impetus to understand both the folding process of individual proteins and the biological and biophysical mechanisms of amyloid formation.

1.5.2 α-Synuclein

The protein α-Synuclein (αS) is the focus of the research presented in Chapter 4.2. αS is a small, highly acidic protein 140 amino acids in length ($\sim$14 kDa) that is expressed predominantly in the human brain and concentrated in presynaptic nerve terminals. The aggregation of αS proteins into insoluble amyloid fibrils has been implicated in Parkinson's disease, dementia with Lewy's bodies, and multiple system atrophy. The central region of the protein, also called the non-Aβ component (NAC), is a minor component of neuritic plaque amyloids in Alzheimer's disease. Alzheimer's disease and Parkinson's disease are the first and second most common neurodegenerative disorders, respectively. The pathology mechanism and aggregation pathway of αS in these diseases is unknown. The physiological function of the protein appears to be in neurotransmitter release and vesicle recycling. It is unknown if the amyloid form of the protein is toxic, or if its formation is a defensive mechanism on the part of the cell, as has also been theorized.[FD07]

αS is unstructured in dilute buffer conditions [WZP$^+$96, FD07], and, as is characteristic of IDPs, has low hydrophobicity and high net charge. αS can be considered as having three subdomains (see Fig. 1.3). The N-terminal region (amino acids 1-60) contains the start of seven 11-amino-acid imperfect repeats that form amphipathic helices. Amphipathic compounds are ones that display both lipophilic and hydrophilic properties. The amphipathic helices are involved in membrane binding and likely play a key role in αS binding to synaptic vesicles [DJCG98, CCR$^+$03, JDSCL04]. The central hydrophobic region (amino acids 61-95) contains the amyloid forming NAC [DSJCL03, DMGM$^+$05, HHB$^+$05]. The C-terminal region (amino acids 96-140) is highly negatively charged, proline rich, and predominantly unstructured [UF02, JDSCL04].

MDVFMKGLSK AKEGVVAAA E KTKQGVAEAA GKTKEGVLYV G SKTKEGVVH 50
GVATVAEKTK EQVTNVG GAV VTGVTAVA QK TVEGAGSIA A ATGFVKKDQL 100
GKNEEGAPQE GILEDMPVDP DNEAYEMPSE EGYGDYEPEA 140

Figure 1.3: The sequence of amino acids in α-synuclein showing the subdomains (N/NAC/C respectively) and imperfect repeats (underlined).

The Deniz laboratory at Scripps Research Institution has investigated the complex conformational space of αS. Various conformations of αS are shown in Fig. 1.4. Which conformation the protein assumes depends upon the concentration of the lipid binding partner. At low lipid concentrations, the protein is unstructured (U-state). Above a certain threshold, helices form in the N-terminal and NAC regions, with a pronounced kink between two helical sections (I-state). An even higher concentration of binding partner induces a shift to a fully extended helical structure (F-state). Once the lipid reaches concentrations at which micelle formation occurs, the protein again adopts a kinked configuration (Im-state) bound to the micelle.[Fer09] These conformations were ascertained in experiments at equilibrium by varying the lipid binding partner concentration. Chapter 4.2 examines the kinetics of the folding pathway of αS when transferred from a low to a high lipid concentration and vice versa.

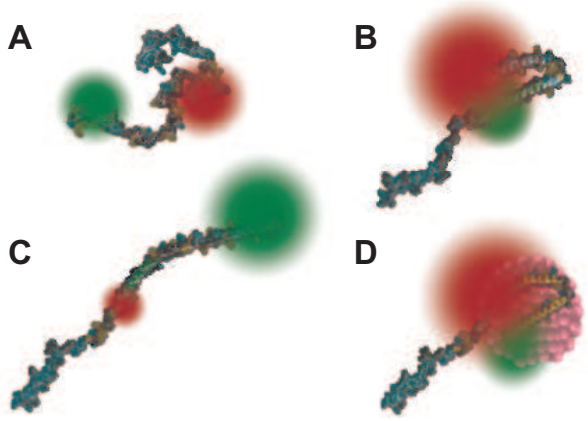

Figure 1.4: Conformations of αS. A) The unfolded protein, with the fluorescent donor (green) and acceptor (red) molecules (explained in section 1.6) B) I-state. C) F-state. D) Micelle and bound I_m-state protein.

1.6 Single-molecule fluorescence microscopy

During the past two decades, the development of new technology capable of performing measurements on single molecules has created the potential to obtain previously unattainable types of data [BT96, MRS+99, MO99, Wei99, TMLO00, Wei00, Moe02, Sch05, MWJ06, MSS+06, CH07, MD07, DML08]. In conventional experiments, measurements are performed on large numbers of molecules and the results depend on ensemble-averaged values of the properties that are measured.

Protein folding is a particularly intractable problem to study with ensemble measurements because of the complex energy landscapes of the folding, various timescales of the folding, and multiple possible pathways and intermediates.[OW05] The advantages of single-molecule methods for the study of this complex process include the following. First, distributions of molecular properties are built up directly by measuring a single molecule at a time. For instance, the proportions of protein molecules in particular folding states can be measured directly with single-molecule techniques, whereas they can only be inferred indirectly from ensemble measurements. Second, it is possible to observe conformational fluctuations of individual molecules (or small ensembles) under equilibrium conditions. This makes it possible to directly determine the connectivity between different states of a complex protein folding landscape. Finally, the high sensitivity of single-molecule methods is very useful when studying amyloidogenic proteins, such as αS, because they can be prone to aggregation at ensemble concentrations. Single-molecule measurements are performed at low protein concentrations (or with immobilized molecules), where aggregation is much less likely to occur.

There are multiple approaches and systems for performing single molecule measurements, including atomic force microscopy (AFM), optical tweezers, and fluorescence microscopy. Optical tweezers and AFM are used to pull protein molecules apart and measure their length as a function of the pulling force in different environments. Interpreting the results of pulling experiments can be problematic, however, because the results do not relate directly to a physical variable, such as the size of the protein. Further, complex experiments to study aggregation or protein interaction with binding partners are difficult to implement

with AFM or optical tweezers. In contrast, certain types of fluorescence measurements, such as F$\ddot{o}$rster Resonance Energy Transfer (FRET), directly measure the distance between two small molecules attached to different spots of a protein chain.[DML08]

FRET is the non-radiative transfer of excited-state energy from a fluorescent donor molecule to a fluorescent acceptor molecule. The transfer efficiency has a very strong dependence on the distance between the two molecules, in a range up to $\sim 100\mathring{A}$. As illustrated in Fig. 4, when the molecules are close together, the transfer efficiency is high and most of the fluorescent emission comes from the acceptor, I_a. Conversely, when the molecules are far apart, the donor fluorescence, I_d, dominates. By recording the amount of donor and acceptor fluorescence, the transfer efficiency, E, is calculated as $E = \frac{I_a}{I_a + \gamma I_d}$, where γ is a correction factor that depends on donor and acceptor properties and on instrumentation. The efficiency can be converted into a distance using the formula $R = R_0(\frac{1}{E} - 1)^{\frac{1}{6}}$, where R_0 is the Forster distance (54 $\mathring{A}$ for the Alexa488/594 donor/acceptor pair and in the 45-65 $\mathring{A}$ range for other single molecule dye pairs; see Fig. 5). By judicious choice of attachment locations, FRET is a valuable tool for studying protein conformations.[BLSD08]

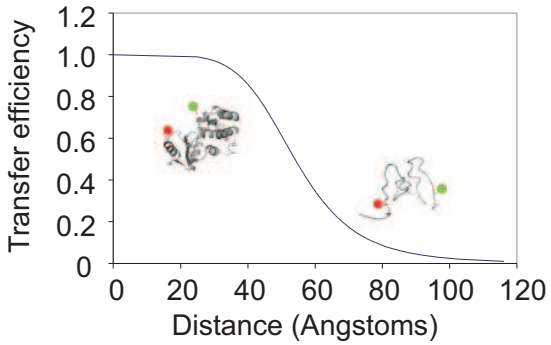

Figure 1.5: The relation between the transfer efficiency, E, and the distance between the donor and acceptor molecules. $R_0 = 54\mathring{A}$ is the distance at which the energy transfer is 50% efficient ($E = 0.5$).

Single molecule FRET experiments can be divided into two categories: those where

the molecule is immobilized on a surface and those where it is freely diffusing in solution [MD07, DML08]. Most studies are carried out on surface-immobilized molecules, using either TIRF (total internal reflection fluorescence) or confocal optical setups. Although these experiments have yielded many interesting results, surface-induced perturbations are problematic for small and dynamic molecular systems. This is especially true for protein experiments, where folding landscapes and dynamics could be easily altered by interactions with a surface.[FBS06] Also, in order to immobilize the protein to a substrate, a third attachment site on the protein is required in addition to the attachment sites for the donor and acceptor molecules.

An alternative to immobilization is to use confocal detection with a low ($\sim$100 pM) concentration of freely diffusing molecules in solution [DDG$^+$99, DLB$^+$00]. A diagram of the setup used for experiments in Chapter 4 of this thesis is shown in Fig. 6A. When a molecule passes through the confocal volume, a burst of photons is recorded. This fluorescence emission is spatially filtered by a pinhole of the confocal setup and separated by a dichroic filter into donor and acceptor components that are detected using two avalanche photodiodes. The intensities of donor and acceptor fluorescence are recorded as a function of time, Fig. 6B. For a low concentration solution (50 - 100 pM), the bursts of photons in these time-traces correspond to individual molecules diffusing through the confocal volume (Fig. 6B, the probability of having two or more molecules in the confocal volume at the same time is very small at these concentrations). The time-traces are processed using a threshold algorithm to obtain corrected donor and acceptor intensities (I_d and I_a), which are used to calculate the FRET efficiency, E, for each molecule that passed through the confocal volume. A histogram of the E values is compiled (Fig. 6C), showing the distribution of values for a large set of molecules.[BLSD08] A common problem in single molecule FRET is the "zero peak" signal arising from either proteins that have been incorrectly labeled with only the donor, or proteins where the acceptor has photobleached or transitioned into a dark state.[EWB$^+$06, RMH06, KNHW07, VKS$^+$08] A microfluidic systems used to reduce photobleaching is presented in Chapter 4.1.

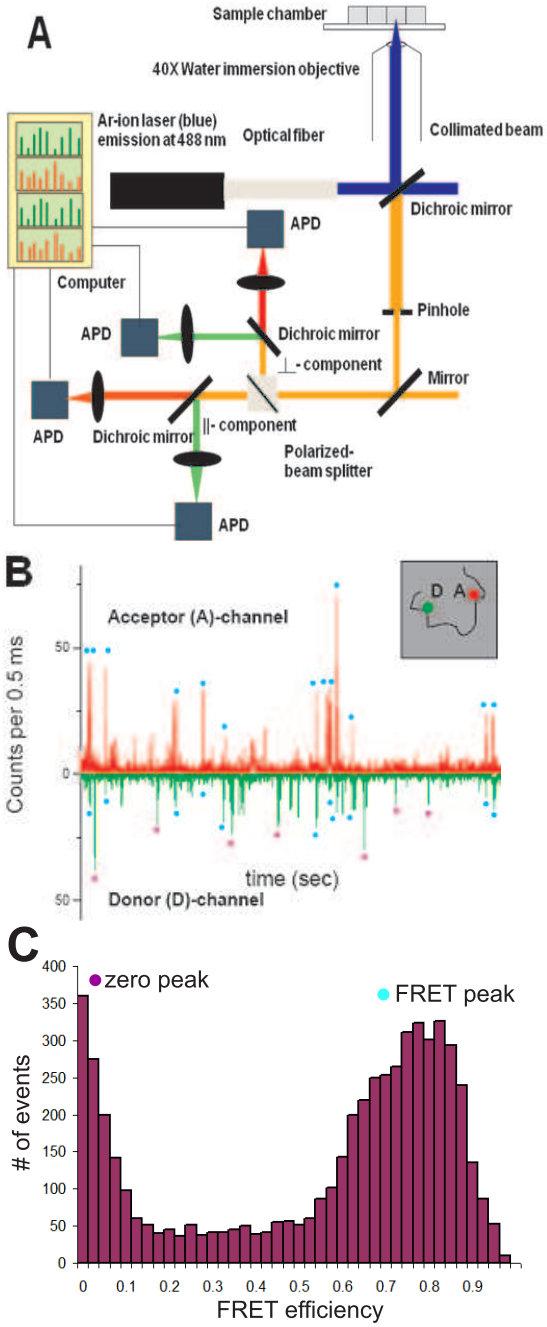

Figure 1.6: Schematic of single-molecule setup for single molecule FRET measurements on molecules freely diffusing in solution. B) Time series of donor/acceptor fluorescence bursts. Bursts contributing to the true FRET peak and the zero-peak are marked with blue and purple dots, respectively. C) FRET histogram. Permission to reproduce panels A and B has been granted by Ashok Deniz.

1.7 Organization of dissertation

Most of the projects I have been involved with are described in this dissertation. My contribution to collaborative projects is stated. A copy of the published or in preparation results follows. Chapters describing projects where I was the leading contributor only include reprints of the published articles without separate introductions.

Chapter 2 reviews the projects where I built and tested microfluidic devices for performing sample preparation of whole blood. The first project in this chapter is a device and method to separate plasma from whole blood using cross-flow filtration. The second project involves using a new cross-flow technique, which we call prefusion in a cross-flow, for both white blood cell separation from whole blood and exchange of the medium of a carrier suspension. I was the only junior contributor to both projects and had unshared first authorship of the published papers.

The project detailed in Chapter 3 was a collaboration with a research group at the Scripps Institute of Oceanography. My major contribution to this project was the fabrication and characterization of the microfluidic devices, development of the experimental set-up, performing preliminary experiments, and data analysis. I was one of two junior authors of the published research paper with shared equal contributions.

Chapter 4 includes the use of microfluidics to develop devices for studying protein folding and improving single molecule fluorescence microscopy, done in collaboration with the Deniz Group at the Scripps Research Insititution. The first project, on which I am shared first author, describes a microfluidic device that rapidly removes protein denaturants for efficient single-molecule measurements and deoxygenates solutions fed to it to reduce photobleaching. My contribution was device design, fabrication, and characterization. The second project in this section describes a microfluidic device to study protein folding kinetics at very fast time scales (200 μs), and my major contribution was device fabrication and characterization.

Chapter 2

Microfluidics for blood component separation and medium exchange

2.1 Plasma separation

We designed, fabricated, and tested a microfluidic device for separation of plasma from whole human blood by size exclusion in a cross-flow. The device is made of a single mold of a silicone elastomer poly(dimethylsiloxane) (PDMS) sealed with a cover glass and is essentially disposable. When loaded with blood diluted to 20% hematocrit and driven with pulsatile pressure to prevent clogging of the channels with blood cells, the device can operate for at least 1 h, extracting ∼8% of blood volume as plasma at an average rate of 0.65 μl/min. The flow in the device causes very little hemolysis; the extracted plasma meets the standards for common assays and is delivered to the device outlet ∼30 s after injection of blood to the inlet. Integration of the cross-flow microchannel array with on-chip assay elements would create a microanalysis system for point-of-care diagnostics, reducing costs, turn-around times, and volumes of blood sample and reagents required for the assays.

Blood tests are one of the most widespread types of medical laboratory diagnostics. Biochemical blood tests are normally performed on blood serum or plasma, the liquid portion of blood without cells. Separation of plasma from whole blood for diagnostics is commonly achieved using centrifugation and typically involves drawing samples of a few milliliters of blood from a patient by venipuncture.[WG04] Recently, significant effort has been invested into miniaturization of biological and chemical assays, which has resulted in the rapid development of microfluidic technologies. Assays on various proteins contained in blood plasma have been successfully performed in microfluidic devices.[CTF$^+$02, JMHD04] Combining onchip assays with on-chip separation of plasma from whole blood would produce a micro-analysis system, which would dramatically reduce the amount of blood and reagents needed for tests. Integrated microfluidic chips would also reduce the amount of time needed to perform an assay, thus minimizing variation in biochemical composition of the blood between sample collection and assay.

Partial separation of plasma from blood was shown in a microchannel flow with a standing acoustic wave.[PNH$^+$05] The wave had a node in the middle of the microchannel, leading to enrichment of red blood cell (RBC) concentration in the middle and depletion of their concentration in the periphery of the microchannel. In another microfluidic device, filtration was implemented with a plug of porous material that was permeable for fluid but impenetrable for particles or cells larger than $\sim$3 μm.[MB03] The fabrication of the device was a multistep process with in situ polymerization to form the porous plug. As the device used dead-end filtration, it became clogged with blood cells, and the efficiency of filtration rapidly decreased. Before the device ceased functioning due to clogging, it separated plasma from 20 μL of rabbit blood that had been diluted by a factor of 20 in a hypotonic solution to increase the rigidity of the RBCs.[MB03]

Clogging of pores of a filter can be substantially diminished and the life of the filter extended by using cross-flow filtration.[BDZ94] In this filtration method, the flow of the particle suspension is directed at a grazing angle to the surface of the filter. The flow near the filter has a strong longitudinal component advecting particles and preventing them from getting stuck on the rough surface of the filter. Cross-flow filtration is the one of the standard methods of separating large volumes of plasma (2-6 L) from blood

in plasmapheresis.[ZC82, Hen86] Cross-flow filtration has also been implemented in microscopic channels [MESS05] and has lately been applied to enriching the fraction of white blood cells (WBC) in the blood.[YS05, SMM$^+$06a] (Enrichment of the WBC fraction had also been shown earlier with a different microfluidic design.[SYMB05]) Recently Crowley and Pizziconi demonstrated separation of plasma from bovine blood in cross-flow driven by capillary forces in a microfluidic device machined in etched silicon bonded to glass.[CP05] However, the amount of plasma collected in the device was inherently limited to ∼50 nL, and the plasma could not be extracted from the device, which prevented testing its quality.[CP05] In this paper we describe design and operation of a microfluidic device for separating plasma from whole blood in a continuous cross-flow. The architecture of microchannels in the device is similar to that in refs [CP05] and [GLC$^+$05]. The filter can operate continuously for at least 1 h with an average plasma yield of ∼0.65 μL/min and, when loaded with freshly drawn human blood, generates high-quality plasma. The microfluidic device is made of a single mold of a silicone elastomer poly(dimethylsiloxane) (PDMS) sealed with a cover glass, is optically clear and compatible with standard microscope objective lenses, and is disposable.

EXPERIMENTAL SECTION

Microfabrication. The device was cast of PDMS using a UV lithography machined master mold.[XW98] A micrograph, a magnified image of part of the filter region, and a schematic diagram of the cross section of the device are shown in Fig. 2.1, panels a-c, respectively. The device has three ports: the inlet, port 1; the blood outlet, port 2; and the plasma outlet, port 3 (Fig. 2.1a). Channels in the device are of three different depths (Fig. 2.1c), the fabrication of which required a master mold with relief elements of three different heights. The master mold was made in a three-step procedure that required multiple formulations of the SU8 UV-curable epoxy (MicroChem, Newton, MA). For the first step, a special low viscosity formulation containing 18% SU8 resin was prepared by diluting commercial SU8 2015 epoxy with SU8 2000 thinner.[GLC$^+$05] A 0.5 μm layer of this epoxy was spin-coated onto a 4 in. silicon wafer and exposed to UV light through a specially designed photomask (a laser-printed film with a resolution of 20 000 dpi). In the second step, a 4 μm thick layer of the epoxy (SU8 2005) was spin-coated on top of the

patterned 0.5 μm layer. A second photomask was aligned with respect to the existing SU8 pattern and the wafer was again exposed to UV light. In the third step, this procedure was repeated with a 25 μm epoxy layer (SU8 2015) exposed through yet another photomask. The wafer was then developed, and the complete mold was baked at 150 °C for 1 h to improve bonding between the silicon and epoxy. To facilitate release of the PDMS replica, the mold was silanized by exposure to a vapor of chlorotrimethylsilane (Sigma-Aldrich, St. Louis, MO) at room temperature for 90 s.

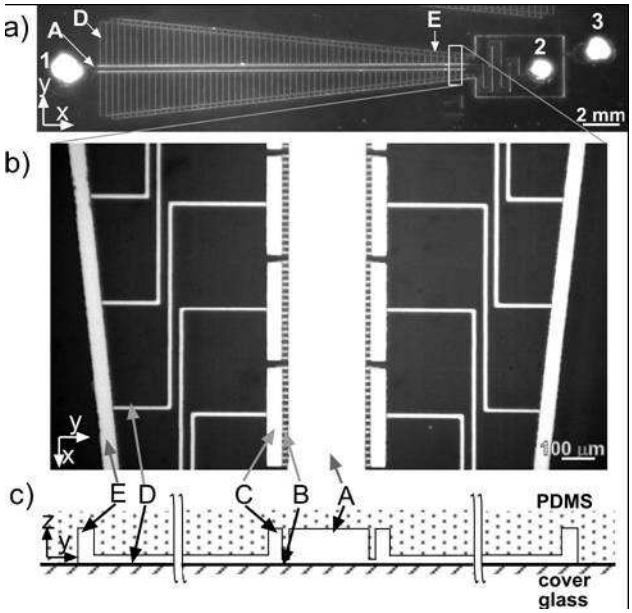

Figure 2.1: Micrographs and a schematic drawing of the microfluidic device. Numbers 1-3 designate the ports, and the capital letters A-E designate channels of different types. (a) Micrograph showing the inlet, port 1; the blood outlet, port 2; and the plasma outlet, port 3. (b) Magnified image of the fragment of the filter region, marked by a rectangle in panel a. This image is rotated 90° from the view shown in panel a. (c) Schematic diagram showing a cross-sectional view of the device (not to scale).

The replica was made out of thin layer of a hard formulation of PDMS (h-PDMS) supported by a thick layer of commercial PDMS (Sylgard 182, Dow Corning, Midland, MI) using a protocol adapted from Schmid and Michel.[SM00] The first part of the h-PDMS prepolymer was composed of vinyl-substituted PDMS (VDT-731, Gelest, Morrisville,

PA) with 35 ppm platinum catalyst (platinumdivinyltetramethyldisiloxane complex in xylene, Gelest) and 0.25% modulator (2,4,6,8-tetramethyltetravinylcyclotetrasiloxane, Fluka Chemie, Switzerland) added to it. It was mixed with the second part, hydrogen-substituted PDMS (HMS-301, Gelest), in a 3.4:1 ratio. A $\sim$140 μm thick layer of the h-PDMS prepolymer was spincoated onto the mold and baked at 85 °C for 2 min, which resulted in partial curing of the h-PDMS. Subsequently, a 5 mm layer of Sylgard 182 PDMS prepolymer was added onto it, and the mold with the h-PDMS-PDMS sandwich was baked at 85 °C for 45 min. (The curing of the elastomers was still incomplete at this stage.) The thick PDMS support was essential since h-PDMS is prone to cracking and has low toughness and low flexibility.[SM00] The h-PDMS-PDMS cast was peeled off the mold, punched with lure stubs for port holes, hermetically sealed to a No. 1.5 microscope cover glass, and baked in an 85 °C oven for a further 2 h to complete curing of the elastomers and enhance adhesion to cover glass. After experiments with blood, elastomer chips were separated from cover glasses, washed in a mild detergent and ethanol, and bonded to new clean cover glasses. An elastomer chip could typically be reused $\sim$5 times.

Samples. Professional phlebotomists drew blood by venipuncture from healthy volunteers. The volunteers consisted of 2 females and 3 males. Blood was collected in heparinized vacutainer tubes (6 mL, 86 USP heparin, BD, Franklin Lakes, NJ). Blood samples were used within 5 h of collection. The hematocrit (volume fraction of blood comprised of red blood cells) of each sample of blood was measured with a Crit-Spin micro-hematocrit centrifuge (StatSpin, Norwood, MA). Phosphate buffered saline (PBS) was added to dilute the sample to a specified hematocrit.

Hemolysis Test Protocol. To estimate hemolysis of plasma samples obtained from the microfluidic device, we measured the concentration of hemoglobin in the plasma. The concentration was measured in relative units, using a sample of lysed whole blood as a reference liquid. The lysed sample was made by diluting whole blood by a factor of 40 with water, which caused all the hemoglobin contained in the RBCs to be released into the solution. Therefore, hemoglobin content in the reference liquid cor-responded to 2.5% hemolysis. Relative hemoglobin concentrations were evaluated using a ND-1000 spectrophotometer (NanoDrop Technologies, Wilmington, DE) via Cripps method.[Cri68] In

this method, background absorption from other proteins, such as bilirubin, is subtracted from the signal using the fact that the concentration of hemoglobin in a sample is proportional to twice absorbance at 576 nm minus that at 560 and 592 nm.

Experimental Setup. Blood was held in 0.02 in. i.d. Tygon tubing attached to the device via a short blunt hypodermic needle inserted into port 1 of the PDMS chip (Fig. 2.1a). The tubing filled with blood was connected to compressed air with pressure P_1. Ports 2 and 3 (Fig. 2.1a) were linked to 100 and 10 μL Hamilton syringes, respectively, through short blunt hypodermic needles and 0.02 in. i.d. Tygon tubing. In pulsatile flow tests, both syringes were connected through a solenoid valve to compressed air at a pressure P_3 that was different from P_1. The valve was powered by a homemade driver and controlled by a computer using a binary data acquisition card (NI-6503, National Instruments, TX) and a LabView program (National Instruments). The fluid levels in the syringes and tubing were kept equal to avoid variations in hydrostatic pressure, so the differential pressure between the inlet and outlets was entirely due to the compressed air pressures P_1 and P_3.

Before blood was injected into the device, the channels were filled with PBS containing 0.1% of Tween 20 (Sigma, St. Louis, MO). The osmolarity of the PBS matched that of blood. The device was mounted on a Nikon TE300 inverted fluorescence microscope equipped with a Sony XCD X700 IEEE 1394 camera. Measurements of fluorescence in microchannels were made with fluoresceinconjugated dextran (FITCD; MW $\sim$77 kDa, Sigma, St. Louis, MO). Variations of the channel depth with pressure were estimated by measuring the intensity of fluorescence in the channels, following the procedure described in detail in ref [GLC$^+$05]. During long (more than 10 min) separation tests, blood injected into the device was continuously mixed to prevent sedimentation. Measurements of flow velocities in microchannels were performed by seeding liquid injected into the inlet with 0.2 μm yellowgreen fluorescent polystyrene beads (Polysciences, Warrington, PA) and using them as tracer particles. Streaklines produced by the particles were photographed on a Nikon Diaphot inverted microscope with a 63x/1.25 objective, under fluorescence illumination derived from a 15 mW single-line 488 nm argon-ion laser (163-A1202, Spectra Physics, Mountain View, CA). (The laser light was focused to a spot with a diameter of $\sim$50 μm in the object plane for high illumination intensity.) To estimate the maximal flow velocities,

we analyzed the longest streaklines, corresponding to beads moving near the central axes of the channels.

Device Design and Operation. Separation of plasma from blood in the device was based on size exclusion. Blood is a suspension of RBCs, WBCs, and platelets in plasma. RBCs are discoid, anuclear cells ∼8 μm in diameter and ∼2.5 μm in thickness, WBCs are spherical cells 8-12 μm in diameter, and platelets are discoid particles 1-3 μm in diameter. In the device, blood was conducted from the inlet to the blood outlet through the A channel (Fig. 2.1), which was 25 μm deep and 240 μm wide and was readily passable for all types of cells. The A channel was 3 cm long, and the first 2 cm of it constituted the filter region. In this region, ∼10 μm wide channels (B in Fig. 2.1) branched perpendicularly off both sides of the A channel in a cross-flow formation. As the B channels were 0.5 μm deep, they were permeable for plasma but not for blood cells. The device contained 1920 of the B channels, each designed to draw off only ∼0.005% of the flux in the A channel. From the B channels, plasma was directed into channels that were 25 μm deep, 310 μm long, and 50 μm wide (C in Fig. 2.1). Each C channel collected plasma from a cluster of 16 parallel B channels and was drained by a single 4 μm deep and 12.5 μm wide channel (D in Fig. 2.1). The D channels fed into two 25 μm deep and 50 μm wide channels (E in Fig. 2.1), which were connected to the plasma outlet. The networks of the B, C, D, and E channels were symmetric about the A channel (Fig. 2.1).

The device was designed with the aim of removing ∼10% of the volume of blood and directing it to the plasma outlet with equal flow rates through all B channels and through all D channels. Calculations of flow rates were made assuming rectangular channels, laminar flow, and constant viscosity fluids, which was a reasonable approximation considering the dilution of blood and high values of shear rate in the whole operational range. For a fluid with viscosity η, the volumetric rate (Q) of flow driven by a differential pressure (ΔP) through a channel of width (w), depth (h), and length (l) is given by $Q = k\Delta P w h^3/l\eta$, where k is a constant that depends on the ratio w/h.[DMB56] For the A, B, D, and E channels, k was 0.078, 0.081, 0.068, and 0.057, respectively. Viscosity of liquid in the A channel was taken to be 1.5 cP corresponding to human blood with a hematocrit of 20% in a 25 μm deep channel.[PNG92] Viscosity of liquid in all other channels was taken to

be 1.2 cP, corresponding to plasma extracted from 40% hematocrit blood diluted 1:1 with PBS.[WMG62] The pressure in the A channel was assumed to vary linearly with distance from the inlet, from P_1 to 0, with a pressure drop of 2/3 P_1 in the filter region. Since the E channels had a large cross-sectional area and low expected volumetric flow rate (on average, 2.5% of the volumetric flow rate in the A channel), pressure variations along the E channels were neglected, and the pressure was taken to be zero everywhere in the E channels.

To ensure the same volumetric flow rate in all B channels, the cumulative resistance, and hence the length, of the B and D channels was varied proportionally to the local pressure in the A channel (Fig. 2.1). Accordingly, B and D channels at the end of the filter region were 1/3 as long as those at the beginning. Each C channel set a uniform pressure at the end of all 16 B channels of the cluster that fed into it. The resistance of the cluster as a whole was 1/16 the resistance of each individual B channel and was 1.5 times lower than the resistance of the D channel connected to it. The drop of pressure in the A channel between the first and last B channel in a cluster was $0.01P_1$, while the minimal pressure drop across a B channel (at the end of the filter region) was expected to be $0.13P_1$. Therefore, the flow rates through individual B channels in a cluster were expected to vary by less than 8%. The device is designed to operate at driving pressures, P_1, up to 4 psi, implying pressure differences as high as 2.67 psi along the filter region. When pressurized, the PDMS walls of channels deform,[GLC$^+$05] making channel profiles more rounded and reducing channel resistances. The effects of compliance are particularly significant in shallow and wide channels, such as the B channels, whose roofs readily deform under pressure and whose resistance decreases as a cube of the depth. The reduction of channel resistance under pressure can lead to redistribution of pressures and flow rates, uneven and excessive draining of plasma, and nonlinear operation of the device. Also, large compliance of the B channels could make them more accessible to RBCs and undermine their size exclusion capability.

To reduce compliance of the B channels, they were made as narrow as the resolution of the photomask allowed (10 μm wide).[GLC$^+$05] Furthermore, the compliance of all channels in the device was reduced by casting it of h-PDMS. The Young's modulus and surface hardness of h-PDMS have been reported to be $\sim$4 times higher than those of a com-

mercial PDMS Sylgard 184 (Dow Corning, Midland, MI; prepared following manufacturer recommendations), which is one of the most common materials for molded microfluidic devices.[SM00]

We found that the depth of the B channels increased linearly with gauge pressure in them,[GLC$^+$05] from 0.5 μm at zero gauge pressure to 1.0 μm at 4 psi (for the depth in the middle). The depth increase was about the same for the D channels, 0.5 μm at 4 psi. For comparison, in a device cast of Sylgard 182 PDMS (Dow Corning, Midland, MI), cured at 80 °C and post-baked at 150 °C for 30 min, the depth of B channels increased from 0.5 to 1.35 m between gauge pressures of 0 and 4 psi. It was not possible to test the compliance of the B channels in the devices cast of Sylgard 182 or 184 cured at 80 °C for 2 h and not exposed to a higher temperature after curing, since the B channels collapsed shortly after bonding of the PDMS chips to cover glasses. We measured the Young's modulus of h-PDMS, Sylgard 184 baked at 80 °C for 2 h, Sylgard 182 baked at 80 °C for 2 h, and Sylgard 182 additionally baked at 150 °C for 30 min to be 10, 1.6, 1.5, and 2.5 MPa, respectively. For the h-PDMS microfluidic device driven at $P_1 = 4$ psi, the compliance was expected to lead to reduction of resistance of the B and D channels by 80% and 10%, respectively, at the beginning and by 45% and 3%, respectively, at the end of the filter region. (The estimates were made assuming parabolic bulging of the channel roofs and taking pressure values averaged along the channels.) Since 60% of flow resistance of the lines connecting the A and E channels (at zero gauge pressure) was provided by the D channels, the overall dependence of distribution of flows in the device on P_1 was expected to be moderate. In order for plasma to arrive at the plasma outlet, it must first pass through the network of B, C, D, and E channels. To reduce the time required for plasma to reach the outlet, an effort was made to minimize volume of the channels of this network. To this end, there is only one D channel per cluster of 16 B channels, and the E channels are narrower than the A channel. The total volume of the side channel network is 0.14 μL, with 0.003, 0.047, 0.013, and 0.075 μL in B, C, D, and E channels, respectively.

RESULTS AND DISCUSSION

To assess the effect of channel wall compliance on the distribution of flows in the device, the volumetric flow rates at the outlets at various driving pressures, P_1, were

measured with pure water injected into the inlet. The ratio of flux directed to the plasma outlet to that directed to the blood outlet increased ∼50% from 0.1 to 0.15 when P_1 was raised from 0.5 to 4 psi. To check whether the flow directed to the plasma outlet was distributed evenly along the filter region, we measured maximal flow velocities in the D channels (which all had the same cross-section of 12.5 x 4 μm) at three separate locations: the beginning, middle, and end of the filter region. At $P_1 = 1$ psi, there was no systematic variation in the flow velocities at the three locations to within 10%, which was the error of the measurement. At $P_1 = 4$ psi, the maximal flow velocity in the D channels dropped by ∼10% between the beginning and the middle, and by another ∼10% between the middle and end of the filter. The results on dependence of the total flow rates and velocity distribution on P_1 indicated that changes in the resistances of the channels with P_1 were consistent with the estimates and tolerable for practical purposes. Initial tests with blood of various hematocrits and P_1 in the range 0.5-4 psi showed that plasma separation was efficient at the outset, but the B channels were quickly clogged with RBCs and platelets (Fig. 2.2), and the plasma flow rate rapidly decayed. A typical dependence of the plasma flow rate on time, measured for 20% hematocrit blood driven at $P_1 = 4$ psi, is shown in Fig. 2.3. In the beginning, the plasma flow rate was 0.95 μL/s; however, it dropped to 50% of the initial value after 5 min, to 20% after 20 min, and to 10% after 40 min.

Clogging of the filter with particles is an endemic problem in cross-flow filtration [BDZ94]. Due to the substantial disparity in size between platelets and RBCs, their modes of clogging the B channels were essentially different. Platelets were small enough to enter the B channels, where some became stuck, effectively reducing the cross-section of the B channels and increasing their resistance. In contrast, RBCs accumulated at the entrances of the B channels with part of the cell protruding into the B channel (Fig. 2.2). (Additional fouling of the B channels might have resulted from accumulation of cell fragments and macromolecules.[BDZ94]) Two factors that apparently exacerbated the clogging were the high deformability of RBCs and reduced rates of the longitudinal flow and shear in the corners of the A channel in front of the B channel entrances (Fig. 2.1c). The unfavorable location of the B channels at the bottom of the A channel, rather than the middle, is a downside of the simple process of the device fabrication by molding.

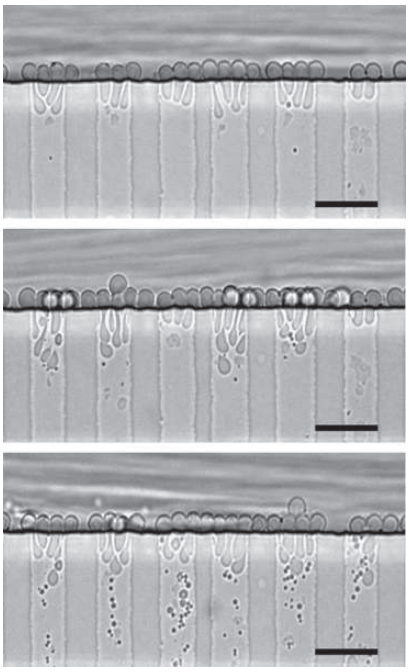

Figure 2.2: Images of the interface between the A and B channels.Panels a-c correspond to 1, 25, and 50 min, respectively, after the injection of blood into the inlet. The flow was driven at $P_1 = 4$ psi with constant zero pressure at the outlets. Blood was flowing from left to right (top part of each panel). As time progressed, RBCs extended increasingly far into the B channels; some RBCs ruptured; and higher numbers of RBCs, platelets, and microparticles (dark dots; possibly cell fragments) were visible clogging the B channels. Scale bar is 20 μm.

Performance of the device was substantially improved with pulsatile pressure (back-pulsing),[BDZ94, RD95, WW02] which is one of the common methods of increasing efficiency in macroscale cross-flow filters. To purge RBCs from the entrances of the B channels, it was sufficient to reverse the direction of flow in the B channels for a short time. The flow was reversed periodically by applying $P_3 = 1.5P_1$ for 100 ms every 3 s (a duty cycle of 1/30). Images of the interface between the B channels and A channel at various phases during the back-pulsing cycle are shown in Fig. 2.4. The periodic flow reversals substantially delayed the decay of the plasma flow rate (Fig. 2.3). Due to the much lower concentration of platelets in blood as compared to RBCs, accumulation of platelets in the

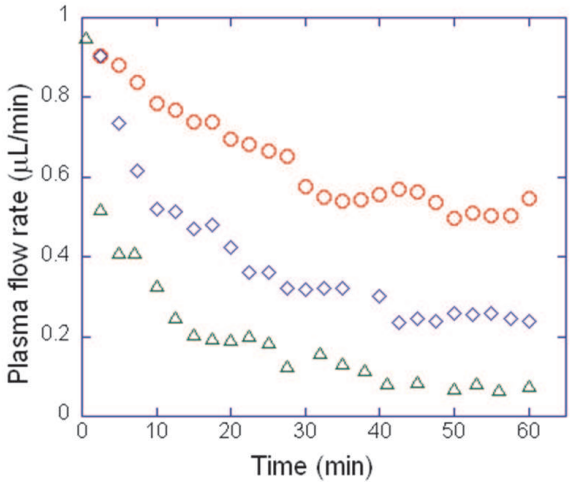

Figure 2.3: Rate of flow of plasma through the plasma outlet as a function of time at P_1 = 4 psi with constant zero pressure at the outlets (triangles) and with two different modes of back-pulsing (diamonds and circles). P_3 = 6 psi was applied to the outlets for 100 ms every 3 s (diamonds and circles) and also for 5 s every 2.5 min (circles). Each curve is an average of two individual tests.

B channels occurred over a longer time scale. Their removal from the B channels required more extended flow reversals. Therefore, in addition to the 3 s reversal cycle, we applied P_3 = 1.5P_1 for 5 s every 2.5 min. We empirically selected this operation mode as a compromise to invert the plasma flow during as small fraction of the cycle as possible, while still maintaining clearance of the B channels during a large part of the cycle.[RD95] The application of the 2.5 min pulsing cycle caused a substantial further retardation in the degradation of the performance of the device (Fig. 2.3). After an hour of operation the plasma flow rate decreased by only ∼45% from 0.9 to 0.5 μL/min. The decay in the plasma flow rate could be partly due to fouling of the B channels by macromolecules or cell fragments that are undetectable under the microscope.[BDZ94] In addition to removal of platelets, the 2.5 min back-pulsing could have slowed the fouling. The total amount of plasma delivered to the device outlet in 1 h was ∼38 μL (equivalent to ∼14 μL of plasma before the dilution to 20% hematocrit), and the mean flow rate was 0.65 μL/min.

The plasma flow rate with back-pulsing was measured for various P_1 and hemat-

ocrits (Fig. 2.5). We only used a short pulsing cycle (directed against the RBC clogging) with $P_3 = 1.5P_1$ applied to the plasma outlet for 100 ms every 3 s. (The blood outlet was not pressurized in this series of tests.) The measurements were carried out during the time interval between 2 and 10 min from injection of blood into the device in order to avoid inconsistencies related to either the presence of the buffer solution in the microchannels at early times or deterioration of the device performance during prolonged operation. The results in Fig. 2.5 are particularly relevant for applications requiring small total amounts of plasma.

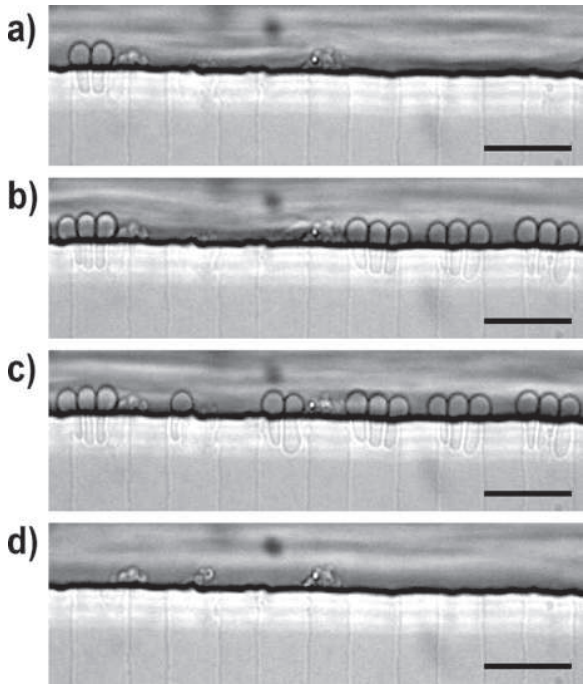

Figure 2.4: Images of the interface between the A and B channels with blood flowing from left to right (top part of each panel) at different phases of a 3-s back-pulsing cycle. The flow was driven by $P_1 = 4$ psi. Micrographs in panels a-d were taken 0.5, 1.5, 2.5, and 0 s, respectively, after the flow was inverted by application of $P_3 = 6$ psi for 100 ms to the outlets. As time after flow inversion progresses, an increasing number of RBCs deformed from their normal biconcave shape are fouling the B channel entrances. Scale bar is 20 μm.

The plasma flow rate was close to linear in P_1 for every value of hematocrit tested

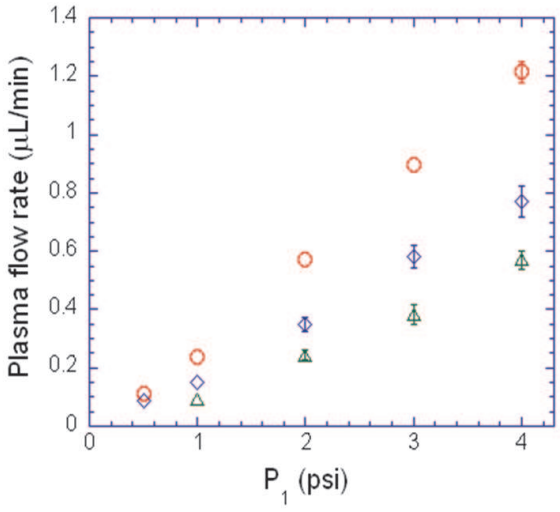

Figure 2.5: Rate of flow through the plasma outlet (plasma flow rate) for blood with hematocrits of 10% (circles), 20% (diamonds), and 30% (triangles) as a function of driving pressure, P_1, with $P_3 = 1.5\ P_1$ applied for 100 ms every 3 s. For each hematocrit the data points show averages of at least five individual tests, and the error bars show the standard errors of the mean. (The error bars are not shown when they are smaller than the symbols.) There was no systematic deviation between results obtained with blood drawn from different subjects.

for P_1 in the range from 1 to 4 psi. As expected from macroscale cross-flow filtration studies,[ZC82, Hen86] blood with a lower hematocrit had a higher plasma flow rate. The percentage of blood volume removed as plasma was also higher at lower hematocrits. It was 14%, 9%, and 8% on average for hematocrits of 10%, 20%, and 30%, respectively. These findings can be explained by slower clogging of the B channels at lower hematocrits. (As a result of the slower RBC clogging, the entrances of the B channels remained clear of RBCs for a larger fraction of the pulsing cycle.) The characteristic wall shear rate of flow in the A channel was estimated as $\dot{\gamma} = \frac{6Q_2}{wh^2}$, where Q_2 is the measured volumetric flow rate through the blood outlet. For blood with 20% hematocrit, $\dot{\gamma}$ varied between 840 and 5100 s^{-1} for P_1 between 1 and 4 psi, respectively. The increase of Q_2 with P_1 was faster than linear, whch might be due to shear thinning of blood and to the compliance of the PDMS walls of the A channel reducing its flow resistance with pressure.

Exposure to high shear rates can activate platelets and WBCs, leading to aggregation. Activation can also be caused by exposure to hydrophilic surfaces (glass and PDMS). Specific tests for activation of blood cells were not performed. However, if present, activation did not seem to affect the operation of the device, as neither platelets nor WBCs were observed to adhere to the PDMS or glass surfaces. Activation might have been mitigated by the short residence time of blood in the microfluidic device, 1.4 and 10 s at $P_1 = 4$ and 1 psi, respectively. Nevertheless, characterization of the degree of activation at various shear rates would be desirable if the plasma were to be used for tests influenced by activation, such as coagulation studies. Ultimately, the choice of type of blood anticoagulant (heparin, citrate, EDTA, etc.), treatment of microchannel surfaces (hydrophilic, hydrophobic, polymer coating, etc.), and suitable range of shear rates in the microchannels should be determined by the intended use of plasma.

The shear rate value of 5100 s^{-1} reached at $P_1 = 4$ psi could be damaging for RBCs.[Ska87, Fun93] Therefore, it was important to test for possible hemolysis in the device. We measured the hemolysis to be 0.08% $\pm$0.06% (mean $\pm$ standard deviation) averaged over twelve plasma samples obtained from the device while operating with 20% hematocrit blood at $P_1 = 4$ psi (with $P_3 = 6$ psi applied for 100 ms every 3 s). Plasma was collected within the first 10 min of operation of the device after injection of blood. The results showed no systematic variation between measurements on samples from different subjects. The measured hemolysis corresponds to a plasma hemoglobin concentration of $\sim$11 mg/dL. This number is higher than the concentration of hemoglobin naturally present in human plasma, $\sim$1 mg/dL, which corresponds to a constitutive hemolysis of $\sim$0.01%.[Rod02] It is also higher than hemoglobin concentration in plasma we obtained by centrifugation of the same blood samples, $\sim$2.5 mg/dL. Nevertheless, the hemoglobin release due to hemolysis induced by the device was far below the level that causes interference in most assays (500 mg/dL).[VTdJ05] Since hemolysis is a general measure of the damage to blood cells, the low levels of hemolysis indicated that the device produced plasma of high quality.

Another important parameter of the device performance was the time required to obtain plasma. To measure this time, 0.1% of FITCD was added to 20% hematocrit blood, which was driven at $P_1 = 4$ psi (with $P_3 = 6$ psi applied for 100 ms every 3 s), and

intensity of fluorescence in a channel immediately prior to the plasma outlet was recorded as a function of time. (As usual, the device was filled with nonfluorescent PBS before blood was injected.) The fluorescence measured at the plasma outlet reached 90% of its saturated value after 33 s ± 4 (mean ± standard deviation) from the moment of blood injection. Thus, 3 μL of plasma from 20% hematocrit blood (equivalent to 1 μL of undiluted blood plasma) can be obtained in ∼4 min, with driving pressure $P_1 = 4$ psi.

CONCLUSIONS

Size exclusion of RBCs, which are only ∼2.5 μm thick and highly deformable, in a device made of a compliant polymer material, such as PDMS, is a challenging task. To reduce the effects of compliance, especially in the B channels acting as filter pores, it was vital to cast the device out of h-PDMS, which has a Young's modulus several times higher than that of commonly used commercial PDMS formulations. Another important element in the device design introduced to counteract the effects of material compliance was the D channels with an intermediate depth of 4 μm and small total volume (∼10% of the volume of the side channel networks). Their specific role was to provide stable resistance for flow of plasma between the A and E channels, ensuring reliable operation of the device over a wide range of driving pressures. An important factor in extending performance of the device was periodic inversion of flow and cleaning of the size-excluding B channels that was implemented by the application of pulsatile pressure to the device outlets (back-pulsing). After 1 h of operation in the pulsatile regime, the plasma flow rate dropped by less than 50% and was ∼7 times higher than in tests without back-pulsing. It is instructive to compare the proposed device with existing miniature filters, such as single hollow-fiber membranes. A hollow fiber membrane normally has a lumen diameter >200 μm; bundles of them are used in many cross-flow filtration systems, including some plasmapheresis machines that handle large blood volumes.

First we note that the total volume of microchannels in the proposed device, ∼0.3 μL, is much smaller than the typical volume of a hollow-fiber membrane lumen. The small internal volume is essential for separating plasma from droplet amounts of blood. In addition, unlike hollow-fiber membranes, the proposed device is easy to combine with other microchannel elements. For example, the only off-chip preprocessing step, dilution

of whole blood, could be eliminated by adding an on-chip mixer [SDA$^+$02, SG05] without significantly changing the device fabrication protocol.

In summary, we constructed and characterized a pressure driven microfluidic device that separated plasma from whole human blood in a continuous cross-flow. The device was made of a single mold of a silicone elastomer sealed by a cover glass, was simple and inexpensive to fabricate, and was disposable (or reusable). The proposed device separated rather large fraction of plasma ($\sim$10%), which was of high quality and contained very little hemoglobin. The plasma flow rate reached $\sim$1 μL/min and plasma arrived at the plasma outlet $\sim$30 s after the injection of blood. The simple method of fabrication of the cross-flow separation microchannel array should facilitate its integration with onchip biochemical plasma assay elements. The integrated chips could then be used for point-of-care clinical diagnostics to perform rapid biochemical tests with only a droplet of blood, which could be obtained by fingerprick instead of venipuncture.

ACKNOWLEDGMENT

We thank Geert Schmidt-Schoenbein, David Schultz, and Edgar Gutierrez for useful advice and suggestions. We also thank Mila Angert for assistance with hemolysis measurements. Funding for this work was provided by NSF Grant OCE-0428900.

Chapter 2.1, in full, is a reprint of the journal article Separation of plasma from whole human blood in a continuous cross-flow in a molded microfluidic device, Analytical Chemistry, 2006. VanDelinder, Virginia; Groisman, Alex. Dissertation author was the first author and a leading contributor of this paper.

2.2 White blood cell separation and medium exchange

We describe a microfluidic technique for separation of particles and cells and a device that employs this technique to separate white blood cells (WBC) from whole human blood. The separation is performed in cross-flow in an array of micro-channels with a deep main channel and large number of orthogonal, shallow side channels. As a suspension of particles advances through the main channel, a perfusion flow through the side channels gradually exchanges the medium of the suspension and washes away particles that are sufficiently small to enter the shallow side channels. The microfluidic device is tested with a suspension of polystyrene beads and is shown to efficaciously exchange the carrier medium while retaining all beads. In tests with whole human blood, the device is shown to reduce the content of red blood cells (RBC) by a factor of about 4000 with retention of 98% of WBCs. The ratio between WBCs and RBCs reached at an outlet of the device is 2.4 on average. The device is made of a single cast of polydimethylsiloxane sealed with a cover glass and is simple to fabricate. The proposed technique of separation by perfusion in continuous cross-flow could be used to enrich rare populations of cells based on differences in size, shape, and deformability.

Many clinical and research assays on white blood cells (WBC) require their prior separation from whole blood, as the presence of other elements of blood can interfere with the assays.[TI05] In human blood, there is only one WBC for every thousand red blood cells (RBC);[WG04] therefore, efficient separation of WBCs is a challenge. The separation of WBCs from whole blood is commonly accomplished either by density-gradient centrifugation or by hypotonic or acidic lysis of RBCs.[RT92, DP98]

Implementation of WBC separation in a microfluidic chip is important for development of WBC assays in self-contained micro total analysis systems (μTAS), requiring only microliter samples of whole blood.[TI05] Exposure of whole blood to deionized water

in a microchannel was shown to cause complete and well-controlled lysis of RBCs with little effect on WBCs.[SAM$^+$04, SMM$^+$06a] However, the subsequent genomic analysis of the WBCs required off-chip centrifugation to remove the RBC debris.[SST06] Other microfluidic separation techniques include dielectrophoresis, which achieved 35-fold enrichment of WBCs in suspension,[HET$^+$01] and specific attachment of WBCs to a substrate or micropillar array.[CGC$^+$97, CLL05, SMR$^+$05]

A specific advantage of microfabricated flow systems is the possibility of accurately defining channel dimensions. Therefore, microfluidic separation devices can exploit intrinsic differences in size, shape, and deformability of blood cells. RBCs are discoid, anuclear cells $\sim$8 μm in diameter and $\sim$2.5 μm in thickness; WBCs are spherical cells 8-12 μm in diameter. In addition to their smaller size, RBCs are much more deformable that WBCs and can enter small capillaries (down to $\sim$2.5 μm in diameter).[Fun93] WBC fractions have been enriched using microfluidic dead-end filters with narrow slits impermeable for RBCs.[CGC$^+$97, WKC$^+$98, PLF$^+$05] In a microfluidic device of another type, blood was driven through a wide and shallow micro-channel, where interactions between RBCs and WBCs led to marginalization of WBCs.[SYMB05] A 34-fold enrichment of the WBC fraction was reported, but the WBC enrichment became less efficient as more RBCs were removed. In still another device, separation was based on the larger minimal distance between WBC centers and the wall of a microchannel, as compared with RBCs. With this method, 29-fold enrichment was achieved after two consecutive separation steps.[YS05] A different microfluidic device that separated RBCs and WBCs was designed for leukapheresis, the removal of WBCs from whole blood, and employed separation in a cross-flow. The WBC-depleted fraction contained as little as 3% of the initial amount of WBCs while retaining 50% of RBCs.[SST06]

A problem related to separation of cells based on size is exchanging the carrier medium in a suspension of cells (or particles). This problem has been approached before with several microfluidic designs, including "leaky valves",[HSH$^+$04, IT06] weirs,[DCAL06] and semi-permeable chambers.[GLC$^+$05] A common feature of these designs is that cells are immobilized at a barrier or trapped in a chamber. Thus, the flow of the suspension through the device needs to be stopped for the time of the medium exchange. The use of physical

barriers for medium exchange can be avoided by application of dielectrophoretic or acoustic forces to cells.[SGJ+04, PNH+05] However, the efficiency of the dielectrophoretic technique depends on dielectric properties of the cells and medium, while the acoustic technique requires integration of piezo-transducers with the chip and is sensitive to the response of cells to an acoustic wave.

Here we describe a technique for separation of cells by size and for exchange of carrier medium in suspensions of particles and cells by perfusion in continuous cross-flow. The technique is used in a device for separation of WBCs from whole blood. The layout of the device is similar to several previous devices for microfluidic cross-flow separation, with a deep main channel and an array of shallow side channels.[BOFY96, CP05, SST06, VG06] However, instead of simply extracting liquid from the main channel into the side channels, the device employs a perfusion flow through side channels directed perpendicularly to the flow in the main channel. The perfusion gradually exchanges the medium in the main channel and washes away particles that are sufficiently small to enter the shallow side channels. The device is shown to efficaciously exchange the carrier medium in a suspension of polystyrene beads with retention of all beads. When loaded with whole human blood, the device produces a suspension of cells with 2.4:1 ratio of WBCs to RBCs. The RBC content is reduced ∼4000-fold with respect to the blood loaded into the device, whereas 98% of WBCs are retained. The device is made of a single cast of silicone elastomer polydimethylsiloxane (PDMS) and thus is inexpensive and simple to fabricate. In addition to separation of WBCs, the proposed technique could be used for enrichment of other rare populations of cells in suspension.

EXPERIMENTAL SECTION

Device design. The device has four ports, consisting of two inlets and two outlets, and a separation network, consisting of microchannels of three different depths, 3, 9 and 25 μm (Fig. 2.6). The separation network has a length L = 24 mm and consists of three main parts: an array of channels for buffer perfusion, a complementary array for the extraction of buffer and RBCs, and a 25 μm deep and 30 μm wide channel (A in Fig. 2.6; also called main channel) in the middle. The network is fed by the two device inlets: port 1 (blood inlet) feeds whole blood into the A channel and port 2 (perfusion inlet) feeds

buffer into a 25 μm deep channel that tapers in width from 45 μm at the beginning to 15 μm at the end of the network (D_1 in Fig. 2.6). There are 200 identical 9 μm deep, 15 μm wide channels (C_1 in Fig. 2.6) branching perpendicularly from the D_1 channel at 160 μm intervals. The C_1 channels are 17.7 mm long and have 4 switchbacks in them to reduce the footprint of the device. Each C_1 channel is connected to a cluster of four 20 μm wide, 3 μm deep, and 0.79 mm long channels (B_1 in Fig. 2.6). The B_1 channels intersect the A channel with a period of 30 μm. There are 800 B_1 channels in all. The perfusion array (B_1, C_1, D_1 channels) and the extraction array are symmetric about the A channel with a 180otation, so complementary channels in the extraction array are labeled as B_2, C_2, and D_2 (Fig. 2.6a, b). The D_2 channel connects to port 4 (RBC outlet). The A channel feeds into a cluster of 8 parallel channels (E_{1-8} in Fig. 2.6a, d), which are each 250 μm wide, 25 μm deep, and 4 mm long. These channels rejoin into a 12 mm long, 25 μm deep, 30 μm wide channel which connects to port 3 (WBC outlet). The E channels are numbered from 1 to 8 starting with the channel closest to the extraction array side of the device.

Blood is injected through port 1 into the A channel, which is large enough to allow unimpeded transit of both RBCs and WBCs. Buffer solution is injected into the perfusion array through port 2. Buffer solution enters the A channel through the B_1 channels, displacing the RBCs in the A channel into the opposing B_2 channels. RBCs proceed through the extraction array to the RBC outlet. WBCs, which are larger and less flexible than RBCs, do not enter the B_2 channels but travel directly through the A channel to the WBC outlet.

Calculations of flow rates in all channels were made assuming rectangular channel profiles; laminar flow; and a fluid with viscosity $\eta = 10^{-3}$ Pas, corresponding to viscosity of water at 20 °C. The volumetric rate, Q, of flow driven by a differential pressure ΔP through a channel of width w, depth h, and length l was calculated as $Q = k\frac{\Delta P w h^3}{l\eta}$, where k is a constant that depends on the ratio w/h.(Dryden, Murnaghan et al. 1956) The device was operated with the pressure applied at the perfusion inlet at 4/3 of the pressure applied at the blood inlet, with neither outlet pressurized. Under these conditions, the calculations predicted constant volumetric flow rate along the A channel, uniform flow rates through all B and all C channels, and equal volumetric flow rates through the perfusion and extraction

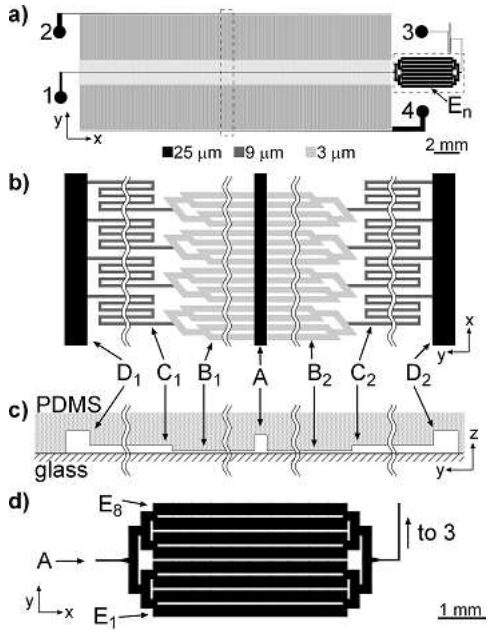

Figure 2.6: a) Drawing of the microfluidic device. Ports labeled with numbers 1- 4 are blood inlet, perfusion inlet, WBC outlet, and RBC outlet, respectively. b) Blow up of a fragment of the separation network outlined with dotted line in (a) turned counterclockwise by 90^{circ} with respect to (a). c) Cross sectional view of channels in the separation network. Dimensions are not to scale. d) Blow-up of E channels outlined with dotted line in (a). Channel depths, 25, 9 and 3 μm, are grey scale coded in (a), (b), and (d).

arrays (and thus through ports 2 and 4). The calculations also predicted the volumetric flow rate through the perfusion network to be $\sim$3 times the volumetric flow rate through the A channel (henceforth referred to as the perfusion ratio).

The distribution of flow rates in the device with blood injected into port 1 was expected to be different from the predictions for water, due to the substantially higher viscosity of blood compared with water. However, we did not attempt to model the flow rate distribution with blood because of the dependence of the viscosity of blood on hematocrit (and thus on dilution by the perfusion buffer) and on microchannel depth, particularly in the 3-25 μm range.[PNG92] Especially large differences between the calculations and experiments with blood were expected for B_2 channels, which have a depth (3 μm) very

close to the thickness and substantially smaller than the diameter of RBCs. In order to minimize inconsistencies, the B channels were designed to account for only 10% of the flow resistance between A and D channels, as calculated for water. The remaining 90% was provided by the C channels, which had both cross-sectional dimensions larger than the diameter of RBCs.

The cluster of E channels was included in the device for characterization purposes and was not integral to WBC separation. These channels had a total width ∼66 times larger than the A channel, which slowed down the flow and allowed reliable discernment of WBCs from RBCs.

Microfabrication. The device was cast of PDMS from a UV-lithography machined master mold. The three different depths of channels in the device (Fig. 2.6) required a master mold with relief elements of three different heights. The master mold was made in a three step procedure that entailed multiple formulations of the SU8 UV-curable epoxy (MicroChem, Newton, MA). Firstly, a 3 μm layer of epoxy (SU8 2002) was spin-coated onto a 4" silicon wafer and exposed to UV-light through a specially designed photomask (a laser-printed film with a resolution of 40,000 dpi). Secondly, a 9 μm thick layer of epoxy (SU8 2005) was spin-coated on top of the patterned 3 μm layer. A second photomask was aligned with respect to the existing SU8 pattern and the wafer was again exposed to UV-light. Thirdly, this procedure was repeated with a 25 μm epoxy layer (SU8-2015) exposed through yet another photomask. The wafer was then developed, and the completed mold was baked at 150 °C for one hour to improve bonding between the silicon and epoxy. To facilitate release of the PDMS replica, the mold was silanized by exposure to a vapor of chlorotrimethylsilane (Sigma-Aldrich, St. Louis, MO) at room temperature for 90 s.

The elastomer cast was produced by pouring a 5 mm layer of PDMS pre-polymer (Sylgard 184, Dow Corning, Midland, MI; 10:1 ratio of base to curing agent component) onto the master mold and baking it at 85 °C for 45 min. The cast was then peeled off the mold and cut into individual chips. The chips were punched with a gauge 20 lure stub for port holes, hermetically sealed to #1.5 microscope cover glasses, and baked in an 85 °C oven for a further 2 hrs to complete curing of PDMS and enhance adhesion to the cover glass. After experiments with blood, elastomer chips were sterilized with ethanol, separated

from cover glasses, washed in a mild detergent, and bonded to new clean cover glasses for reuse.

Blood samples. Professional phlebotomists drew blood by venipuncture from healthy volunteers, consisting of 2 females and 3 males. Blood was collected in heparinized vacutainer tubes (6 mL, 86 USP heparin, BD, Franklin Lakes, NJ). Blood samples were used within 5 hours of collection. The hematocrit (volume fraction of blood comprised of RBCs) of each sample of blood was determined with a Crit-Spin micro-hematocrit centrifuge (StatSpin, Norwood, MA). The WBC count of each sample was determined with an improved Neubauer hemacytometer.

Experimental set-up. Prior to use, devices were air plasma treated for 45 s. The channels of the device were then filled with Dulbecco's phosphate buffer saline (PBS) containing 0.1% Tween 20 (Sigma) and 1% bovine serum albumin (Sigma). The osmolarity of the PBS matched that of blood.

Liquids were fed into and drawn off from the microfluidic device through 0.5 mm ID plastic tubing and short blunt hypodermic needles inserted into the ports. Blood was held inside a segment of tubing, which was connected to port 1 (Fig. 2.6a) at one end and to a source of compressed air with pressure $P_1 = 1.00$ Psi and the other end. Blood injected into the device was continuously mixed to prevent sedimentation. Perfusion buffer (PBS) was held in a 100 μL Hamilton syringe connected to port 2 and pressurized at $P_2 = 4/3P_1 = 1.33$ Psi. Ports 3 and 4 (Fig. 2.6a) were linked to 50 μL Hamilton syringes, which were open to atmosphere. All three syringes were held upright and the fluid levels in them as well as the level of blood were kept equal to avoid variations in hydrostatic pressure; therefore, the differential pressure between the inlets and outlets was entirely due to the compressed air pressures P_1 and P_2.

The device was mounted on a Nikon TE300 inverted fluorescence microscope equipped with a Sony XCD X700 IEEE 1394 camera. Characterization of flow velocities in microchannels was performed by seeding liquid injected into the inlets with 1 μm fluorescent polystyrene beads (Bangs Laboratories, Inc.; Fishers, IN) and using them as tracer particles. Streaklines produced by the beads were photographed under the microscope using fluorescence illumination. To estimate the maximal flow velocities, we analyzed the longest

streaklines, corresponding to beads moving near the central axes of the channels.

For visualization and measurement of WBC fluxes, acridine orange (Sigma) was added to whole blood at a concentration of 0.1 μM and allowed to incubate for 30 min before injection of the blood into the device. The numbers of WBCs and RBCs directed to the WBC outlet were evaluated in the E channels using one of two imaging methods. Either we took sequences of images under brightfield illumination with a blue-violet filter (407 $\pm$ 52 nm, Edmund Industrial Optics, Barrington, NJ) to increase contrast between WBCs and RBCs, or we took sequences of matching pairs of images under brightfield and fluorescent illumination. Measurements made with the two methods were consistent. Measurements of WBC fluxes at the blood inlet and the RBC outlet were performed with fluorescence illumination.

RESULTS AND DISCUSSION

The performance of the device was first characterized with water injected into both inlets. We measured the volumetric flow rates to be 0.21, 0.60, 0.21, and 0.62 μL/min at the blood inlet, perfusion inlet, WBC outlet, and RBC outlet, respectively (Fig. 2.6a). The uncertainty on each measurement was 5%. The volumetric flow rate in the A channel was uniform to within 10% along its length, suggesting a nearly exact balance of flow rates through the perfusion and extraction arrays, in agreement with the calculations. The ratio of the volumetric flow rate at the RBC outlet to that at the WBC outlet (perfusion ratio) was $\alpha = 3.05$. Therefore, the distribution of volumetric flow rates in the device closely matched the results of the calculations for water.

Next, we explored effects of perfusion on composition of the carrier medium and concentration of the particles in a suspension injected into the blood inlet. We used 9.6 μm green fluorescent polystyrene beads suspended in an aqueous solution with 0.12% FITC-dextran (FITCD; 2 MDa, Sigma) and 6.5% NaBr (added for neutral buoyancy of the beads). A plain salt solution of 6.5% NaBr in water was injected into the perfusion inlet. The mean flow velocity in the A channel was $\bar{\nu} = 4.7$ mm/s, corresponding to a characteristic residence time $t_r = L/\bar{\nu} \approx 5$ s in the separation network and a characteristic perfusion time $t_p = t_r/\alpha \approx 1.7$ s. As the suspension advanced along the A channel, the plain salt solution injected from the B_1 channels gradually displaced the FITCD solution into the B_2 channels,

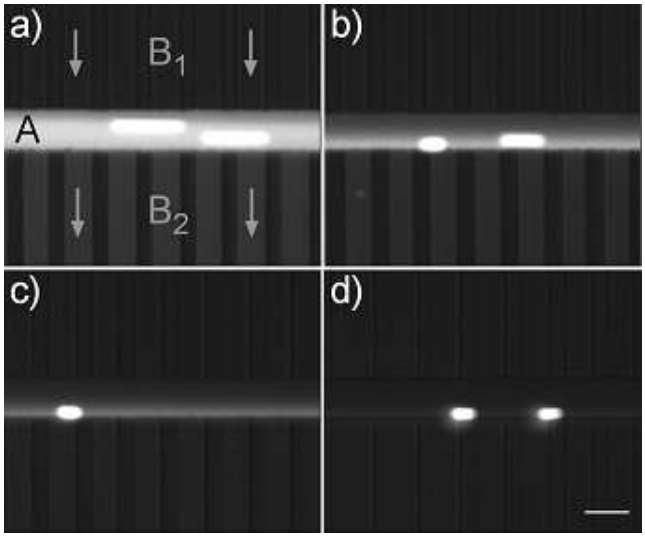

Figure 2.7: Suspension of fluorescent beads (9.6 μm diameter) in solution of FITC-dextran in 6.5% NaBr injected at blood inlet is perfused by a 6.5% NaBr solution injected at the perfusion inlet. (a), (b), (c), and (d) are fluorescence images taken at distances $x = 0$, $0.25L$, $0.5L$, and L, respectively, from the beginning of the separation network. A weak brightfield illumination is added to make the contours of the microchannels perceivable. Streaklines generated by the beads become shorter at the end of the channel, as the beads are displaced towards the entrances of the B2 channels. Scale bar is 30 μm.

whereas the beads, although displaced toward the B_2 channels, were all retained in the A channel (Fig. 2.7). Because of the low diffusion coefficient of FITCD, D $\approx$ 7 μm^2/s, and small characteristic length of diffusion during the perfusion time, $\Delta y = \sqrt{2Dt_p} \approx 5$ μm, the distribution of FITCD across the A channel was highly non-uniform with a visible boundary between regions with high and low concentrations of FITCD.

The mean concentration of FITCD in the A channel at the exit of the separation network was estimated by measuring the intensity of fluorescence in the cluster of E channels, where the distribution of FITCD was substantially smoother than in the A channel. The mean intensity of fluorescence in the E channels was found to be 64 times lower than in the case when all E channels were filled with the source suspension with 0.12% FITCD. This reduction in the fluorescence suggested 64-fold reduction in the mean concentration of

FITCD in the A channel as a result of the passage through the separation network.

To test the effect of the perfusion on a concentration of small molecules, we injected a solution of $c_0 = 50$ ppm of FITC (Sigma) in a pH = 7.5 phosphate buffer into the blood inlet and injected buffer without FITC into the perfusion inlet. The diffusion coefficient of FITC, $D \approx 450$ μm^2/s, corresponds to a characteristic diffusion length $\Delta y = \sqrt{2Dt_p} \approx 40$ μm, which is larger than the diameter of the A channel. Therefore, the distribution of FITC across the A channel was close to uniform along the entire channel (Fig. 2.8), which enabled us to estimate the local mean concentration of FITC, c , by measuring the mean intensity of fluorescence in the channel. For a solution that remains well mixed during perfusion, the fractional reduction in the concentration is equal to the ratio of the injected volume to the total volume of the solution, $\frac{dc}{c} = -\frac{dV}{V}$. For the A channel, with the perfusion evenly distributed along the separation network and the total perfusion ratio $\frac{\Delta V}{V} = \alpha$, we have $\frac{dV}{V} = (\frac{\alpha}{L})dx$, where x is the distance from the beginning of the separation network. Combining these equations, we obtain $dc/c = -(\alpha/L)dx$ and $c(x) = c_0 \exp(\frac{-\alpha x}{L})$, where $\alpha = 3.05$. The measured dependence of c on x was well fitted by an exponential curve $c(x) = c_0 \exp(\frac{-3.03x}{L})$, closely matching the expected dependence of c on x (Fig. 2.9). The dilution of the FITC concentration at the end of A channel was $\frac{c(L)}{c_0} = 20.5 \approx e^{-\alpha}$.

We also tested the device with a 0.005% (by volume) suspension of 2 μm fluorescent polystyrene beads injected into the blood inlet and plain buffer injected into the perfusion inlet. The flux of beads measured at the exit of the separation network was 58 times lower than the bead flux at the entrance. Because of the very low diffusivity of the beads ($D \approx 0.4$ μm^2/s corresponding to $\Delta y = \sqrt{2Dt_p} \approx 1$ μm), they are expected to closely follow the A channel streamlines. These streamlines can be approximated as vector sums of two orthogonal steady flows: longitudinal flow along the x-axis and transverse flow in the yz-plane, from B_1 channels to B_2 channels (Fig. 2.10). A bead moving along a typical flow trajectory should traverse the A channel in the distance $x = L/\alpha \approx L/3$ from the beginning of the separation network. However, the transverse flow is highly non-uniform with particularly low flow velocities in the upper corners of the A channel (Fig. 2.6c and Supporting Information, Fig. 2.10b-d). Therefore, beads moving along flow trajectories with substantially lower than average ratios between the transverse and longitudinal flow

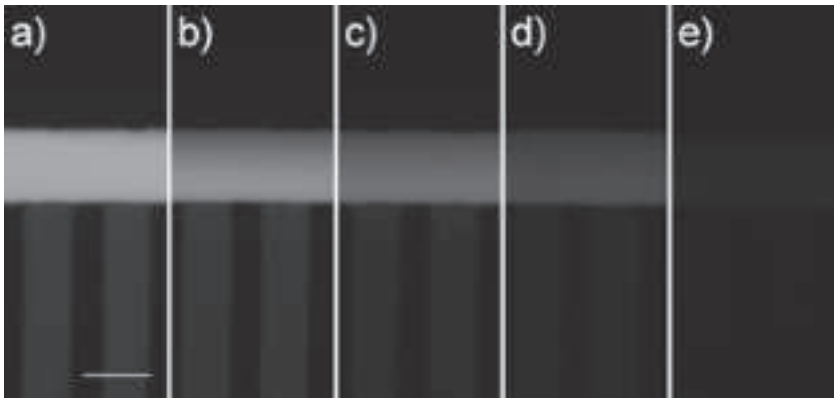

Figure 2.8: Solution of fluorescent dye, FITC, injected at blood inlet is perfused by a plain buffer injected at the perfusion inlet. (a)-(e) fluorescence images of the A channel with adjacent B_1 and B_2 channels at distances $x = 0$, $0.125L$, $0.25L$, $0.5L$, and L, respectively, from the beginning of the separation network (cf. Fig. 2 and 4 in the main text). The A channel is the horizontal strip in the middle. Vertical strips in the lower halves of the frames are B_2 channels. B_1 channels above the A channel are not seen, because the liquid in them is the perfusion buffer solution without fluorescence dye. The amount of fluorescent dye in the A channel exponentially decreases with x. Scale bar is 30 μm.

velocity could remain in the A channel even at the end of the separation network ($x = L$). Similar arguments also apply to other low diffusivity species, in particular FITCD molecules (Fig. 2.7). It is worth noting that lower diffusivity of beads and FITCD compared with FITC leads to higher dilution of the beads and FITCD by the end of the separation network (58- and 64-fold vs. 20.5-fold).

The operation of the device with blood is illustrated in Fig. 2.11 and 2.12. With whole blood injected at the blood inlet and buffer injected at the perfusion inlet, the volumetric flow rates at the blood inlet, perfusion inlet, WBC outlet, and RBC outlet, were 0.06 ± 0.015, 0.80 ± 0.025, 0.27 ± 0.04, and 0.61 ± 0.04 μL per minute, respectively (mean $\pm$ standard deviation of 9 separate trials with different blood samples). The scatter in the data was caused in part by the slightly discrepant hematocrits of the blood samples used in different trials. The error on individual measurements due to instrumental uncertainties and fluctuations of the mean flow rate was 5%. The volumetric flow rates were calculated by

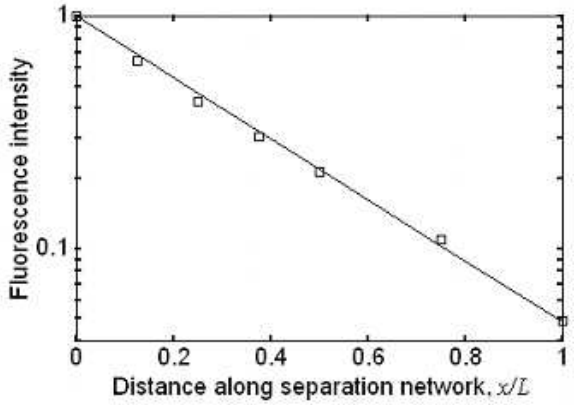

Figure 2.9: Intensity of fluorescence of a FITC solution in the A channel as a function of distance, x, from the beginning of the separation network in semi-logarithmic coordinates. The intensity is normalized with its maximal value measured at the beginning of the network and x is normalized with the length of the network, L. Fluorescence intensity is proportional to dye concentration. The solid line is an exponential fit to the data.

measuring maximal flow velocities in the 25 μm deep channels connected to the respective inlets and outlets. Velocity profiles were assumed to be identical to those for a Newtonian fluid and were calculated using equations from ref [Whi91]. The presence of blood cells at the blood inlet was expected to modify the velocity profile making it blunter compared with that for a Newtonian fluid. Nevertheless, according to an existing model of blood flow [SP01] applied to the actual dimensions of the channel and hematocrit, the effect of the profile blunting on the volumetric flow rate calculation was expected to be negligible (less than the measurement error). When measured over a period of 15 min, the volumetric flow rate of blood was found to fluctuate by less than 15%, with no discernable drift of the mean. The maximal shear stress in the A channel occurred at the end of the separation network near the top and bottom walls of the channel (cf. Fig. 2.10a) and was calculated to be 2.4 $\mathrm{N/m^2}$.

Values of various parameters measured in representative individual experiments with blood are shown in Table 2.1, along with the average values of these parameters from 20 trials. The RBC concentrations were measured directly with a Neubauer cytometer once

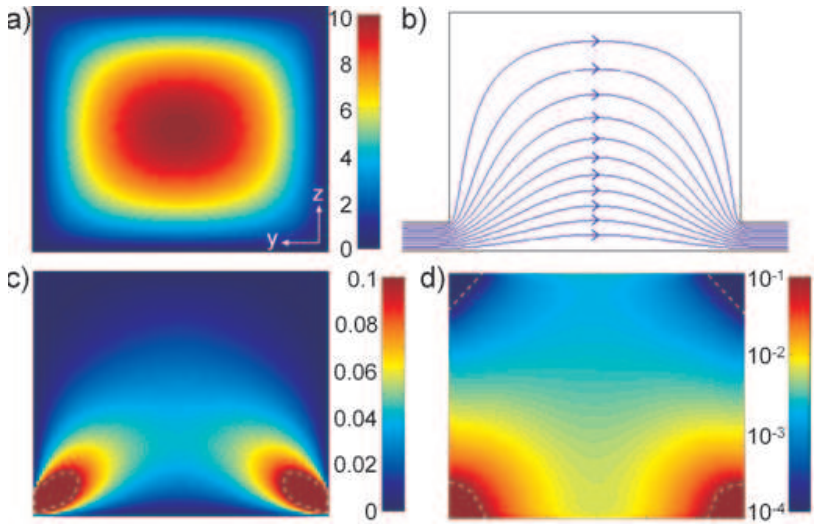

Figure 2.10: Longitudinal and transverse flow in the yz-cross-section of the A channel. The velocity profile of the longitudinal flow is calculated with MatLab (MathWorks, Natick, MA) using equations from [Whi91]. The transverse velocity profile is calculated with FemLab assuming a two-dimensional flow in the yz-plane. a) Distribution of longitudinal flow velocity; velocity scale in the color map is in mm/s. b) Flow lines of transverse flow. Fragments of the B_1 and B_2 channels are shown in the left and right bottom corners, respectively. c) Distribution of the absolute value of the transverse flow velocity, $\sqrt{v_y^2 + v_z^2}$. The velocity scale in the color map is in mm/s; velocity in the regions inside dashed lines is above 0.1 mm/s. d) Distribution of the ratio of transverse to longitudinal velocity. Color map is in a logarithmic scale. Dashed lines designate regions with ratios above 10^{-1} and below 10^{-4}.

for each donor, and thereafter were calculated from the hematocrit assuming an average volume per RBC of 92 fL. On average, only 2% of the WBCs went to the RBC outlet. At the WBC outlet there were 2.4 times as many WBCs as RBCs on average. Only 0.025% of the RBCs went into the WBC outlet, corresponding to a 4,000-fold reduction of the RBC content and a 4,000-fold increase in the ratio of WBCs to RBCs after the passage through the separation network. The device operated continuously without clogging or deterioration of separation efficiency for the whole time of tests, which was typically 1 hour. We did not perform any tests for shear-induced hemolysis in the device. However, based on the results of our previous experiments with blood in a similar range of shear stresses in a cross-flow

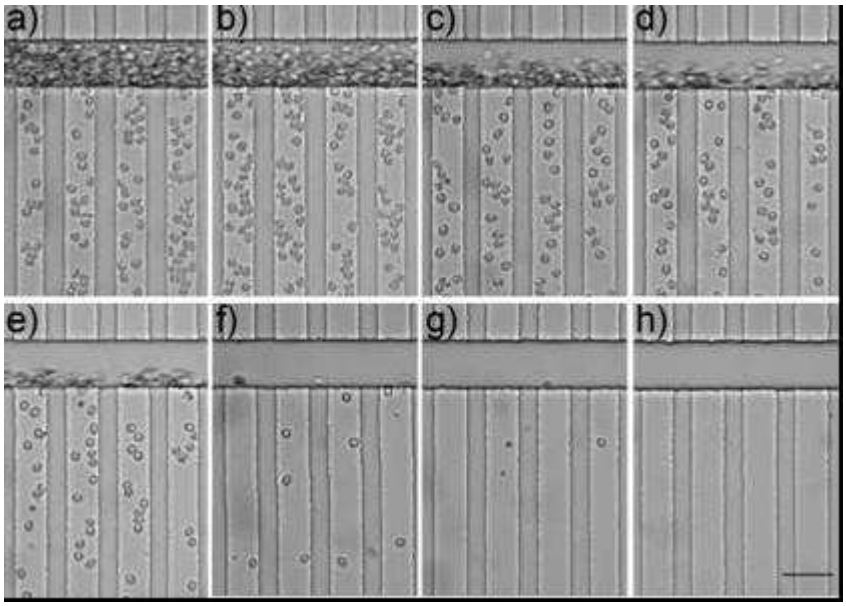

Figure 2.11: Images of RBCs entering B_2 channels from the A channel. (a)-(h) are micrographs at distances between $x = 0$ and $x = 0.7L$ from the beginning of the separation network with increments of $0.1L$. The horizontal channel (A channel) is 25 μm deep and the vertical channels (B_1 and B_2 channels) are 3 μm deep. No WBCs are seen in (h) due to their low concentration and short exposure time. Scale bar is 30 μm.

microchannel array [VG06], the hemolysis in the device and the hemoglobin concentration at the WBC outlet were expected to be minimal.

The concentration of WBCs at the inlet was calculated from the flow rate and the number of WBCs going through the channel per unit time (WBC flux) to be 2700 WBCs/μL on average (Table 2.1). The average concentration of WBCs at the inlet was ∼50% of their average concentration in the blood samples as measured with the hemacytometer. Therefore, the ratio of WBCs to RBCs at the WBC outlet was on average only ∼2100 higher than in the original blood samples. The reasons for the reduced concentration of WBCs at the blood inlet could be adhesion of WBCs to the walls of the tubing and non-uniform distribution of WBCs across the tubing, resulting in their slower than average flow velocity. Better agreement between the concentration of WBCs at the blood inlet and the original concentration could be achieved by directly loading a small blood sample into the

Table 2.1: Values of parameters measured in experiments with blood.

	Data from 5 representative trials					Average of the 5 trials	Average of all (20) trials	Standard deviation of all trials
Hematocrit	41	45	43	40	40	42	42	2
RBC concentration in initial blood sample, 10^6 cells/μL	4.5	4.9	4.7	4.3	4.3	4.5	4.5	0.2
WBC concentration in initial blood sample, 10^3 cells/μL	6.0	4.2	6.5	4.1	4.1	5.0	5.4	1.0
WBC flux at blood inlet, cells/s	3.1	2.1	1.5	2.2	1.9	2.2	2.9	1.6
WBC flux at WBC outlet, cells/s	4.0	2.7	2.6	2.0	2.0	2.7	2.8	1.6
WBC flux at RBC outlet, cells/s	0.02	0.03	0.02	0.02	0.06	0.03	0.03	0.02
Ratio of WBCs to RBCc at WBC outlet	5.8	2.4	3.7	1.5	1.2	2.9	2.4	1.2
Fraction of RBCs directed to WBC outlet, %	0.04	0.02	0.05	0.02	0.01	0.03	0.025	0.02
Fraction of WBCs directed to RBC outlet, %	0.3	1.3	0.4	1.3	5.0	1.7	1.9	1.8

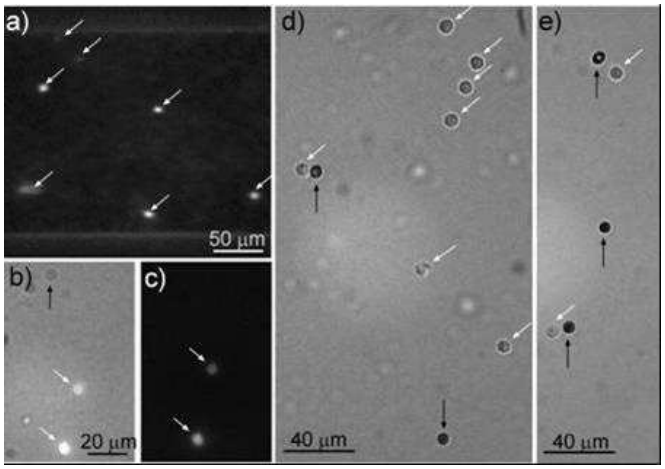

Figure 2.12: Images of blood cells at various areas of the microfluidic device. WBCs are highlighted with white arrows; RBCs are highlighted with black arrows. a) Fluorescence image of blood near blood inlet. b) Image of two WBCs and one RBC in E_1 channel taken under mixed illumination, brightfield and fluorescence. c) Fluorescence image of same cells as in (b); the RBC is not fluorescent. d-e) Brightfield images of portion of E_1 channel taken with blue-violet filter; (d) shows seven WBCs, one of which has an RBC attached to it, and one spherical RBC; (e) shows two WBCs, two spherical RBCs, and one bi-concave RBC with the characteristic light spot at its center.

blood inlet and completing the separation within a short time after the loading.

At the blood inlet, the WBC flux was typically measured for ∼40 seconds with ∼120 individual cells counted. Optical detection of WBCs at the blood inlet was hindered by obstruction of WBCs by RBCs (Fig. 2.11a). Moreover, although the flow rate at the blood inlet was stable, there were large fluctuations in the WBC flux over time. These factors contributed to substantial uncertainty in the measurement of the WBC flux at the blood inlet (Table 2.1). At the RBC outlet, WBC detection was relatively easy, because the concentration of RBCs there was reduced by a factor of ∼10 compared with whole blood. However, measurements of WBC flux at the RBC outlet had large uncertainty (Table 1) due to the small number of WBCs arriving at this outlet. Typically, only ∼6 WBCs were counted during a 3 minute measurement.

As WBCs and RBCs moved through the A channel, they were displaced toward

the extraction array side of the channel (cf. Fig. 2.7 and 2.11). Therefore, WBCs were only found in the first four of the eight E channels (Fig. 2.6). The fluxes of WBCs and RBCs were measured in each of the first four E channels by counting cells entering a channel for at least 30 seconds, and the measured values were summed to calculate the total fluxes of the two cell types at the device outlet. As measurements of WBC fluxes at the blood inlet and the outlets were not performed simultaneously, the fluctuations at the blood inlet also made it difficult to verify the balance of WBC fluxes into and out of the device. In some experiments, the measurements of WBC fluxes at the blood inlet and the outlets resulted in appreciably different values (Table 2.1). Nevertheless, the WBC flux values averaged over a large number of tests were very close, with the ratio of WBC fluxes between the inlets and outlets at 1.02. This nearly exact WBC balance suggested that WBCs were neither destroyed nor accumulated inside the device.

The reduction in the flux of RBCs between the blood inlet and the WBC outlet by the factor of 4000 was drastically higher that the 58-fold reduction measured in the experiment with the suspension of 2 μm beads. Moreover, removal of RBCs from the A channel was completed by $x = 0.7L$; the number of RBCs entering the B_2 channels (Fig. 2.11) decreased approximately linearly between $x = 0$ and $x = 0.6L$ and was close to zero at $x > 0.7L$ (data not shown). An apparent reason for the larger reduction in flux of RBCs as compared with beads is the higher perfusion ratio in experiments with blood. Perfusion ratio estimates based on the volumetric flow rates in the A channel at the beginning and end of the separation network (0.06 and 0.27 nL/s) are $\sim$13 and $\sim$3, respectively. Taking an average of these two values, we can estimate the perfusion ratio at the point where removal of RBCs is completed ($x = 0.7L$) as $\sim$5.5, which is significantly higher than $a \approx 3$ in the experiment with 2 μm beads. Another possible factor contributing to the higher reduction of RBC flux is the size exclusion of RBCs (because of their relatively large diameter) from the upper corner regions of the A channel, where the ratio between flow velocities in the yz-plane and along the x-direction is particularly low (Fig. 2.10). This exclusion is expected to result in more uniform motion of RBCs across the A channel, which seems to be consistent with the observed dependence of the number of RBCs in B_2 channels on x. Faster motion of RBCs across the channel due to size-exclusion from the upper corners is analogous to

the behavior of suspended particles in flows used in hydrodynamic chromatography. In this separation technique, suspensions are driven through narrow capillaries or porous media. Large particles are size-excluded from the slow flow near-wall regions and thus are eluted faster than small particles.

Because of the 4.5-fold increase in the volumetric flow rate from the blood inlet to the WBC outlet, the mean concentration of WBCs at the outlet decreased 4.5 times to 600 cells/μL. Nevertheless, $\sim$85% of the WBCs were found in the first two of the eight E channels, so the mean concentration of WBCs in these two channels was 2040 cells/μL, close to their concentration at the blood inlet. This finding shows that the displacement of cells and particles toward the extraction side of the A channel (Fig. 2.7 and Fig. 2.11) can be used to collect them at higher concentration. This type of displacement of cells and particles is similar to the displacement of particles towards a semi-permeable wall of the main channel by cross-flow in flow field-flow fractionation systems.[Gid93]

The population of RBCs at the WBC outlet was saliently different than the original RBC population (Fig. 2.12d, e). On average, 39% of RBCs at the WBC outlet were either stuck to WBCs or in clumps of several RBCs stuck together (Fig. 2.12d), only 13% of the RBCs (0.003% of the original sample) were lone cells with a biconcave shape, and the remaining 48% of the RBCs (0.015% of the original RBC sample) appeared spherical in shape (Fig. 2.12d, e). The number of spherical RBCs at the WBC outlet increased an average of 25% for each subsequent trial (typically performed $\sim$1 hr later) with the same blood sample. Therefore, a major reason for the spherical shapes of RBCs was aging of the blood sample. Additionally, some spherical RBCs could have been present in the original blood sample or could have been RBCs injured during transit through the device or during prior handling of the sample. Spherical RBCs seemed to be too thick and too inflexible to enter the B_2 channels. The fraction of spherical RBCs at the WBC outlet varied among tests, but was always substantial ($>$ 57% of lone RBCs were spherical in 90% of the trials), whereas they were hard to find in the original blood samples and among cells flowing to the RBC outlet. We examined a series of micrographs of RBCs in the B_2 channels (cf. Fig. 2.11) with a total of a few thousands cells and estimated that the fraction of spherical RBCs was less than 0.1%.

The technique of separation by perfusion in continuous cross-flow implemented in the proposed device has multiple applications. As demonstrated in the experiment with the suspension of 9.6 μm beads (Fig. 2.7), the technique can be used to exchange medium in a suspension of particles (or cells) in continuous flow without changing the volume of the suspension and with retention of all particles. For the least efficient medium exchange, as occurs with highly diffusive chemicals in the medium (and slow flow), a 1000-fold dilution of the medium requires a perfusion ratio of only $\ln(1000) \approx 10$. The medium exchange could be used to induce or stain live cells. Cells or particles could be exposed to multiple media in succession in a device with multiple perfusion inlets feeding various fluids into a sequence of perfusion microchannel arrays. In this manner, a sequence of chemical reactions with molecules attached to the particles could be carried out in continuous flow in a microfluidic chip.

For efficient separation of WBCs, it was important to choose an appropriate depth of B channels (size exclusion cutoff). The depth of 3 μm both allowed retention of 98% of WBCs and made B channels permeable to $\sim$99.997% of lone RBCs with regular bi-concave shapes. Another factor crucial for efficient separation of WBCs was perfusing blood in the main channel with a volume of buffer several times higher than the volume of blood (perfusion ratio of $\sim$5.5). The possibility to use high perfusion ratios to achieve high degree of separation makes the proposed technique advantageous compared with regular cross-flow filtration for separation of cells and particles by size.

It is worth noting that the configuration implemented in the proposed microfluidic device, with perfusion in a cross-flow, is not commonly used in large-scale cross-flow separation systems.[BDZ94] Setups with perfusion in a cross-flow are common in the flow field-flow fractionation (FlFFF).[Gid93] However, in FlFFF systems, the counterpart of the extraction side of the main channel is usually only permeable for the carrier medium and impermeable for all particles. The particles are separated by the difference in their times of elution from the main channel.[Gid93] Thus, separation with FlFFF cannot be performed continuously, as opposed to the proposed technique.

The ratio of WBCs to RBCs reached at the WBC outlet was 2.4 on average, which we expect to be sufficiently high for assays on WBCs. In contrast to ref [SAM$^+$04,

SMM$^+$06a], the final WBC suspension did not contain the products of the hypotonic or acidic lysis of RBCs, making it potentially more suitable for on-chip assays. In addition, the concentration of WBCs at the outlet of our device was substantially (∼40-fold) higher than in the devices using RBC lysis.[SAM$^+$04, SMM$^+$06a] The WBC concentration could be further increased by readjusting the resistances of the channels to change the flow distribution in the device and to eliminate the increase in the flow rate along the A channel. The rate of flow of blood through the device could be increased by applying a higher driving pressure, widening the main channel, and optimizing the rate of perfusion flow.

The large number of spherical cells among the RBCs at the WBC outlet indicated that in addition to the separation of WBCs, the device has the capacity to enrich sub-populations of RBCs that differ from other RBCs in size, shape, and deformability. This capacity is of particular interest, because enrichment of rare sub-populations of RBCs cannot be achieved using lysis or centrifugation, the usual methods of separation for WBCs. Therefore, the proposed technique of perfusion in continuous cross-flow could be used to separate rare cell types, which are difficult to separate with other methods, with potential applications to cell harvesting and medical diagnostics. For example, the presence in blood of RBCs with reduced flexibility is associated with such deceases as malaria, sickle cell anemia, and hereditary elliptocytosis.

CONCLUSIONS

We constructed and tested a microfluidic device that employs a new technique, perfusion in continuous cross-flow, to separate WBCs from whole human blood. The fraction of WBCs was enriched ∼4000-fold in a single passage through the device, which is two orders of magnitude higher than reported previously in microfluidic devices with continuous flow and without RBC lysis; 98% of WBCs were retained. The device could be used as a part of μTAS to perform initial sample preparation for subsequent on-chip analysis of WBCs. Additional applications of the proposed technique are enrichment of rare cell populations and exchange of medium in suspensions of particles and cells. The medium exchange can be used for staining cells and for carrying out chemical reactions on surfaces of particles in continuous flow.

ACKNOWLEDGEMENTS

We thank Edgar Gutierrez for help with handling blood samples and with FemLab simulations. We are grateful to Geert Schmidt-Schonbein, Amy Sung, Sanford Shattil, and Ana Kasierer-Friede for useful suggestions. Funding for this work was provided by NSF grant OCE-0428900 and the DARPA Center for Opto-Fluidic Integration,

http://www.optofluidics.caltech.edu.

Chapter 2.2, in full, is a reprint of the journal article Perfusion in microfluidic cross-flow: separation of white blood cells from whole blood and exchange of medium in a continuous flow, Analytical Chemistry, 2007. VanDelinder, Virginia; Groisman, Alex. Dissertation author was the first author and a leading contributor of this paper.

Chapter 3

Microfluidics for dinoflagellate response latency measurements

Dinoflagellate bioluminescence serves as a model system for examining mechanosensing by suspended motile unicellular organisms. The response latency, i.e. the delay time between the mechanical stimulus and luminescent response, provides information about the mechanotransduction and signaling process, and must be accurately known for dinoflagellate bioluminescence to be used as a flow visualization tool. This study used a novel microfluidic device to measure the response latency of a large number of individual dinoflagellates with a resolution of a few milliseconds. Suspended cells of several dinoflagellate species approximately 35 μm in diameter were directed through a 200 μm deep channel to a barrier with a 15 μm clearance impassable to the cells. Bioluminescence was stimulated when cells encountered the barrier and experienced an abrupt increase in hydrodynamic drag, and was imaged using high numerical aperture optics and a high-speed low-light video system. The average response latency for *Lingulodinium polyedrum* strain HJ was 15 ms (N>300 cells) at the three highest flow rates tested, with a minimum latency of 12 ms. Cells produced multiple flashes with an interval as short as 5 ms between individual flashes, suggesting that repeat stimulation involved a subset of the entire intracellular signaling pathway. The mean response latency for the dinoflagellates *Pyrodinium bahamense*, *Alexandrium moni-*

latum and older and newer isolates of *L. polyedrum* ranged from 15 to 22 ms, similar to the latencies previously determined for larger dinoflagellates with different morphologies, possibly reflecting optimization of dinoflagellate bioluminescence as a rapid anti-predation behavior.

All organisms and cells sense external stimuli and respond to changes in their environment. Sensing of mechanical stimuli serves in the detection of vibrations and sound, acceleration, gravity, proprioreception, pressure and fluid flow. In multicellular organisms, the mechanosensory system usually involves sensory cells, a neural network, and effectors such as muscle. Each system component introduces a lag between application of the stimulus and the physiological response. This lag, known as the stimulus response latency, provides crucial information on the processing and functionality of the sensory system [FP98]. It also provides a sensitive sublethal assay for determining how sensory systems are affected by environmental conditions [PF03] and contaminants [LCYL03, CR06]. Of ecological significance is the behavioral response latency, the delay between stimulus and behavioral response. Some rapid predator escape behaviors of aquatic animals involve very short response latencies of <30 ms [WK72, BB85, EDN88, ZD88, HBL99, LH99, BLH02, BH03, PF03]

Mechanosensing also plays important roles for individual cells of multicellular organisms and for unicellular organisms. Endothelial cells attached to the walls of blood vessels are subjected to fluid shear stress due to blood flow [Fra93], causing a number of rapid and long-term physiological, morphological and gene expression changes [Rei94, GCF96, CLS98, CLZ$^+$01]. Suspended unicellular organisms such as ciliates and some flagellates use escape jumps to avoid predator feeding currents [Jak01, Jak02], whereas luminescent dinoflagellates use light flashes to disrupt predator feeding behavior [BMS83, BS83].

Dinoflagellate bioluminescence is a fascinating model system for mechanosensing. Dinoflagellates, the most common sources of bioluminescence in coastal waters [Sta66, Tet71], use light emission as an anti-predator strategy. The mechanical stimulus from predator contact is thought to cause cell deformation that activates the mechanotransduction pathway. The luminescent response has a 'flash bulb' effect, disrupting the feeding behavior of a predator [BMS83, BS83, BRSW85, BS85] and leading to a decrease in grazing [EC72, Whi79]. Bioluminescence can also act as a 'burglar alarm' to attract secondary

predators, increasing the risk to the dinoflagellate grazer [Mor83, MC92, AT93, FC95]. In addition to its role in predator-prey interactions, dinoflagellate bioluminescence is also stimulated by flow stresses of different origins that have sufficient magnitude to cause cell deformation. This type of stimulation is most commonly associated with high shear flows that are created in boundary layers around swimming animals [Hob66, RLF$^+$98], in ship wakes [RHFL02] and in breaking surface waves [SDLR04], leading to spectacular displays of bioluminescence during periods of high cell abundance [Sta66, RLF$^+$98, Lat05]

The bioluminescence of dinoflagellates is stimulated by the velocity gradient rather than absolute flow velocity [LR99, ML07] and can thus serve as a reporter of local velocity gradients and hydrodynamic stresses, making it a unique tool for both field [Roh99, RHFL02] and laboratory [CLF03, SDLR04] flow visualization. Based on laboratory studies using well-characterized flow fields [LCG94, LR99, LJA$^+$04, LNR04] a statistical model has recently been developed that predicts bioluminescence intensity as a function of shear stress level and cell concentration [DS05]. This model has been used to infer flow properties from bioluminescence intensity in flows not amenable to conventional measurements. Nevertheless, if dinoflagellates do not respond instantaneously to the stimulus, in high-speed flows the location where the flash response is observed can be substantially downstream of the location where a cell is stimulated by high local shear.

A delay between stimulation and light emission reflects the dynamics of mechanotransduction and of activation of cellular signaling pathways. High mechanical stress increases the fluidity of the dinoflagellate plasma membrane [MHVD$^+$02], causing activation of GTP-binding proteins [CLSF07] and a calcium flux, mainly from the release of Ca^{2+} from intracellular stores [vDL02]. The calcium flux leads to the generation of an action potential at the tonoplast, the membrane surrounding the vacuole [Eck65b, WC81], causing a proton flux from the vacuole to cytoplasm [NS79] and a decrease in cytoplamic pH. Acidification acts on scintillons, vesicles in close proximity with the vacuole that contain the chemicals involved in the luminescent reaction [JIFH85, NMBH91]. Low pH activates luciferase, inactive at physiological pH, which catalyzes the luminescent reaction [HD86]. In *Lingulodinium polyedrum*, low pH also dissociates the luciferin substrate from its binding protein [FH71] and makes it available for oxidation, leading to light emission. The response

latency represents the total duration of all these signal transduction events.

Using individual restrained dinoflagellate cells impaled with an electrode, the response latency to mechanical stimuli was previously estimated at ∼20 ms for the heterotrophic *Noctiluca scintillans* [Eck65a, ES68] and the autotrophic *Pyrocystis fusiformis* [Wid81]. These are large, non-motile, non-thecate species reaching dimensions up to 1 mm. For a flow speed of 2 m/s, a response latency of 20 ms corresponds to a downstream translation of 4 cm, a distance over which flow properties can change considerably. Statistically robust measurements of the response latency are needed for motile unrestrained dinoflagellates used for luminescent flow visualization and for correlating their bioluminescent flash responses with flow properties.

To measure the latency of response of dinoflagellates to hydrodynamic stresses with high resolution, a few basic experimental conditions must be met. First, the exposure of dinoflagellates to the stresses must occur over a time interval much shorter than the expected response latency, i.e. less than 5-10 ms, and the moment of exposure needs to be recorded with a high accuracy. Second, the light emitted by individual dinoflagellates needs to be measured with high temporal resolution. As the total number of photons emitted in one flash event is relatively small, it is important to collect the emitted light efficiently using high numerical aperture (NA) optics. Both conditions are difficult to meet using the conventional table-top flow setups. Hydrodynamic stress applied by starting a flow (e.g. by switching on rotation in a Couette flow system) is only established after a characteristic transient time $t = d^2/\nu$, where ν is the fluid kinematic viscosity (10 - 6 m^2/s for water at 20 °C) and d is the characteristic size of the flow setup (e.g. the size of the annular gap for a Couette flow system). Even in the smallest flow setup used previously [vDBL05], the transient time was 400 ms, much longer than the estimated latency time. In addition, table-top setups are incompatible with the standard high-NA short working distance microscope objectives, and the light emitted by luminescent cells is usually collected rather inefficiently with low-NA long working distance optics.

To meet the basic experimental conditions, we performed the experiments using a novel microfluidic setup. Microfluidics involves the study and application of flow in various arrangements of microscopic channels. The advent of microfluidic systems has led to a

growing number of biological applications in the areas of cell culture, flow cytometry, cellular biosensors, immunoassays, enzyme assays and cellular chemotaxis [SSA04, EAGG$^+$05, HGK$^+$05, deM06, Whi06]. Flows of liquids in microscopic channels are almost always laminar, linear and stable. Therefore hydrodynamics stresses in the flow can be controlled with high precision (e.g. kept constant over extended periods of time and quickly switched when needed) and reproduced with high accuracy. Microfluidic flows with controlled stresses have been applied to studies of the strength of adhesion of fibroblasts [LKW$^+$04] and neutrophils [GG07] to a substrate, shear stress responses of endothelial cells [SGF$^+$05] and hepatocytes [TYO$^+$06] attached to a substrate, deformation of erythrocytes under shear [ZAN$^+$06], swimming of microorganisms [MS06], and the effect of transient hydrodynamic forces on cell lysis of microalgae [HGH$^+$07].

The primary technical goal of our study was to test the feasibility of using microfluidic technology to apply well-defined mechanical stimuli to cells with a short inception time and to observe the responses of a large number of individual cells with millisecond resolution. The primary scientific objective was to obtain precise measurements of the response latency of mechanically stimulated bioluminescence from different species of motile dinoflagellates. To achieve these goals, we used a continuous flow in a microfluidic device with channels of two separate depths that created a barrier impenetrable to the dinoflagellates while allowing the flow to pass through. When individual cells were brought by the flow to the barrier, they came to a sudden stop and were exposed to an abrupt increase in hydrodynamic stress, with a transition time on the order of 1 ms, that triggered their bioluminescent response. The impulse associated with the impact did not play a significant role in triggering the bioluminescence. Immobilization of the dinoflagellates at the barrier greatly facilitated observation of their bioluminescence, which was measured with a temporal resolution as high as 4 ms. In this initial study, we focused on the response latency, flash duration, characteristic number of flashes per cell and the intervals between flashes, while other parameters such as the temporal pattern of flash intensity were not considered.

The main species investigated was *Lingulodinium polyedrum* (Stein) Dodge 1989, one of the most well-studied dinoflagellates in terms of general biology [LH97] and flow responses [LCG94, JVL00, JL02, LNR04, LJA$^+$04]. *L. polyedrum* is a coastal species, 35 μm

in diameter [KRK92], that is responsible for extensive blooms [Har76, Gre00] with dramatic nighttime displays of bioluminescence [Lat05]. The response latency was measured for three strains of *L. polyedrum*, an isolate of *Pyrodinium bahamense* Plate 1906 var. bahamense from a bioluminescent bay in Puerto Rico, and a Florida isolate of the saxitoxin-producing *Alexandrium monilatum* (Howell) Taylor 1979. The last two species are similar in size to *L. polyedrum*.

MATERIALS AND METHODS

Test organisms. The dinoflagellates tested are all motile thecate coastal species, approximately 35 μm in cell diameter. Three non-axenic, unialgal strains of *Lingulodinium polyedrum* (formerly *Gonyaulax polyedra*) collected from the Scripps Pier (La Jolla, CA, USA) were tested because the phenotype of a dinoflagellate, including its bioluminescence, can be affected by the time the dinoflagellate strain has been in culture [Swe86, vDBL05]. Therefore, we measured the response latencies of newer and older strains of *L. polyedrum* isolated from the Scripps Pier: strain CCMP407, isolated in 1970 by B. Sweeney; strain HJ, also referred to as strain LpSIO95 [JDYP$^+$05], isolation date unknown; and strain CCMP1932, isolated in 1998 by A. Shankle. The CCMP designation refers to strains maintained by the Provasoli- Guillard National Center for Culture of Marine Phytoplankton (http://ccmp.bigelow.org). Other dinoflagellates tested were a strain of *Alexandrium monilatum* isolated in 2000 from the Mississippi Sound, USA, by J. Rogers [Juh05], and *Pyrodinium bahamense* isolated in 2000 from Baha Fosforescente, La Parguera, PR, USA by A. Juhl. *P. bahamense* and *A. monilatum* were grown in f/2 medium [GR62] minus silicate at a temperature of 26 °C, whereas the *L. polyedrum* strains were grown in half-strength f/2 medium at 20°C. All cultures were grown on a 12 h:12 h light:dark cycle. Only cultures in mid-exponential growth phase, i.e. 5-20 days after inoculation, were used. Cell concentrations were determined from cell counts of defined volumes (usually 10 μl) in a multi-well slide under the microscope. Toward the end of the light phase, when dinoflagellate bioluminescence is not mechanically stimulable [BSBS69], a sample from the desired culture at a concentration of 2000-15,000 cells/ml was loaded into a 60ml plastic syringe that was covered with opaque material at the beginning of the dark phase.

Microfluidic apparatus. The microchannel device had two inlets, two outlets,

and channels of two different depths, 15 and 200 μm (Fig. 3.1). It was made out of a lithographically micro-machined polydimethylsiloxane (PDMS) chip sealed with a no. 1.5 microscope cover glass, using a fabrication procedure described elsewhere [SG05]. Flow in the microchannels was driven by setting differences in hydrostatic pressure between the inlets and outlets of the device (Fig. 3.1) [GEQ03]. The dinoflagellate cell suspension and filtered seawater were kept in four 60 ml plastic syringes, which were held upright. The syringe with the cell suspension was connected to inlet 1, and the three syringes with filtered seawater were connected to inlet 2 and outlets 1 and 2 (Fig. 3.1). The syringe linked to outlet 1 was connected through a solenoid valve to a source of compressed air with regulated pressure, P_g, which allowed the pressure at the outlet 1 to be increased by P_g for a pre-set amount of time.

The microfluidic device was designed to abruptly expose dinoflagellates to an adjustable level of mechanical stress and to create reproducible flow conditions for measuring the individual responses from large numbers of cells in repeated experiments. In the upstream part of the test region, channel 1, which is fed by inlet 1, merges with side channels 2 and 3, which are both fed by inlet 2 (Fig. 3.1C). The three merging channels form a single channel 4, which is 600 μm wide. Channels 1-3, as well as most of channel 4 have the same depth (h_0) of 200 μm. However, about 200 μm downstream from the merging, the depth of channel 4 (h_b) abruptly decreased to 15 μm, creating a barrier that is impenetrable to the cells, which are approximately 35 μm in diameter (Fig.3.1D). When the stream of the cell suspension from channel 1 enters channel 4, it is hydrodynamically focused between the streams of seawater from channels 2 and 3 and directed toward the center of the barrier. Observations showed that all dinoflagellates stopped at the entrance to the 15 mm deep section of channel 4 and rested in mechanical contact with both the barrier (wall in the yz-plane) and the bottom of the channel (wall in the xy-plane; Fig. 3.1D). Therefore, the drag force experienced by a cell at the barrier was largely independent of its original trajectory inside channels 1 and 4.

A cell passively flowing in a deep rectilinear channel, such as channel 1, moves with the average velocity of the liquid around it and thus experiences no net hydrodynamic drag. A mechanical stimulus applied to the cell originates from velocity gradients in the

flow and the resulting shear stresses. When the cell arrives at the barrier, its motion stops and it is abruptly exposed to a hydrodynamic drag that originates from the flow of liquid around the stationary cell and is proportional to the characteristic velocity of this flow. The mean flow velocity under the barrier is a factor of $h_0/h_b \approx 13$ higher than the mean flow velocity in the channel 4. Therefore, the drag experienced by the cell at the barrier is particularly high and the arrival of the cells at the barrier triggers the bioluminescence response. The drag remains constant the entire time a cell stays at the barrier, eliciting multiple bioluminescent flashes by some cells (see below). An analysis of stimuli applied to a cell at the barrier and in a selected position upstream of the barrier is presented in the Numerical simulations subsections of Materials and Methods and Results.

The width of the cell-laden stream in channel 4 and at the barrier depends on the ratio of volumetric flow rates in channel 1 and channels 2 and 3, which is adjusted by varying pressures P_1 and P_2 at inlets 1 and 2, respectively. The width is normally three to five times smaller than the 150 μm width of channel 1, and the mean flow velocity in channel 1 is three to five times less than the velocity in channel 4. The resulting shear stress experienced by cells in channel 1 ($<$0.3 N/m^2) is lower than the luminescence response threshold for *L. polyedrum* [LCG94, LR99, LNR04] so the probability of premature stimulation of bioluminescence is minimal. Excessive reduction of the flow rate in channel 1 would be undesirable, however, because of the concomitant decrease in the number of cells reaching the test region per unit time. Channel 1 has a total length of 110 cm (Fig. 3.1B) and occupies most of the area of the microfluidic device. This long length is necessary to provide large flow resistance at low shear rate and to provide sufficient resolution when adjusting the rate of flow in channel 1 by varying P_1.

The flow in the device was steady, and cells were continuously arriving at the barrier. To prevent their accumulation at the barrier, which would alter the flow conditions, cells were removed from the test region a few seconds after their arrival by applying pressure P_g to outlet 1 for 1-3 s (Fig.3.1B) causing cells to be evacuated through channel 5 towards outlet 2.

Numerical simulations. The goal of the numerical simulations was to evaluate forces acting on a dinoflagellate approaching and encountering the barrier. The domain of

the simulations was a 150 μm long fragment of the 600 μm wide, 200 μm deep channel 4 immediately upstream of a 25 μm long fragment of the barrier (15 μm deep; see Fig. 3.2A). A dinoflagellate was modeled as a sphere with radius (R) of 17.5 μm. The model dinoflagellate was placed in the xz-plane of symmetry of the channel (Fig. 3.2A).

The simulations were performed using the commercial finite element solver Comsol 3.2 (Femlab). Because of the curved boundary of the sphere representing the dinoflagellate, tetrahedral unstructured meshes were used and the mesh size was decreased in the vicinity of the sphere and of corners by the Comsol gridder. The boundary conditions were no slip on lateral walls (boundaries parallel to the xy- and xz-planes) and on the surface of the sphere. Different constant pressures were assigned to the entrance and the exit planes (boundaries parallel to the yz-plane), with the difference in the pressures driving the flow. The dynamic viscosity was taken to be 0.001 kg/ms corresponding to seawater at 20 °C [Vog81]. The convergence and accuracy of the simulations was tested by comparing the results obtained with different mesh resolutions and gridding strategies. In addition, we verified that the y-component of the force and the x and y components of the torque applied by the flow to the sphere are close to zero.

The numerical simulations were performed for two different situations: with the sphere at the barrier and with the sphere approaching the barrier. In the former case, the sphere was assumed to be at rest, touching both the barrier and the lower boundary of the channel (Fig. 3.2A), and the total force exerted on the sphere by the flow was calculated. For the latter case, we took the sphere to be 30 μm in front of the barrier and 30 μm above the lower boundary of the channel (the center of the sphere at 47.5 μm in front of the barrier and 47.5 μm above the lower boundary). We calculated the translational and angular velocities of the sphere, assuming that the inertial forces were negligible compared with the viscous forces and thus both the net force and net torque exerted on the sphere by the flow were zero. The computation was done iteratively. The translational and angular velocities of the sphere, $\mathbf{v}$ and $\boldsymbol{\omega}$, were assigned initial values of zero. At each iteration, the values of the force and torque, $\mathbf{F}$ and $\mathbf{T}$, exerted on the sphere by the flow were calculated, and $\mathbf{v}$ and $\boldsymbol{\omega}$ were updated according to $v^{(i+1)} = v^{(i)} - aF^{(i)}$ and $\omega^{(i+1)} = \omega^{(i)} - bT^{(i)}$ (where the upper index in the parentheses indicates the step number). The constants were chosen

empirically at a=109 s/kg and b=1015 s/m^{2}kg. The procedure was repeated 25 times until both $\mathbf{F}$ and $\mathbf{T}$ were essentially null ($F^{(25)} \approx 10^{-3}F^{(0)}$ and $T^{(25)} \approx 10^{-6}RF^{(0)}$), and the final values of $\mathbf{v}$ and $\boldsymbol{\omega}$ together with the flow velocity field after 25 iterations were used to calculate the forces applied to the sphere by the flow.

Imaging setup. The microfluidic device was mounted on the mechanical stage of a Zeiss Axiovert 135 inverted microscope (Carl Zeiss, Thornwood, NY, USA). To be able to record the arrival of dinoflagellates at the barrier, a low-level bright-field illumination was used. The test region was viewed using a 63x/1.4 or 40x/0.75 objective lens and a high-speed low-light video system consisting of a GENIISYS intensifier (DAGE-MTI of MC, Michigan City, IN, USA) coupled to an AVT Marlin F-033B digital video camera (Allied Vision Technologies GMBH, Stadtroda, Germany). The camera was computer-controlled via an IEEE 1394 interface with LabView IMAQ code (National Instruments Corporation, Austin, TX, USA). The images of the test region with luminescent cells were typically taken at a rate of 250 frames/s with a frame size of 96x640 pixels.

Data acquisition and analysis. A custom LabVIEW (National Instruments, Austin, TX, USA) virtual instrument (VI) provided control over video capture and camera parameters, such as frame rate, exposure time, and size of the region of interest. Video frames were collected in a 200-300 frame buffer; when a flash occurred, the buffer contents were saved to the computer hard drive. We used Vision Assistant 7.1 (National Instruments Corporation, Austin, TX, USA) to analyze the video sequences. To evaluate the latency in the bioluminescent response, the number of frames between the arrival of the cell at the barrier and the initiation of a flash was counted. The latency was calculated as the number of frames multiplied by the known interval between frames (the inverse of frame rate). For the video rate of 250 frames/s, a three-frame delay resulted in an estimated response latency of 12ms (see Fig.3.3). The error associated with this method was caused by two uncertainties. One uncertainty was associated with the difference between the actual time of arrival of the cell at the barrier and the middle time point of the frame where the cell was first seen at the barrier. The other uncertainty was the difference between the actual beginning of the flash and the middle time point of the first frame with visible luminescence. Each of the uncertainties was estimated as a half of the interval between frames, and because

the two uncertainties were independent from each other, the total error in the latency was estimated as 0.7 of the interval between frames, i.e. 3 ms for the frame rate of 250 frames/s. To evaluate the duration of a flash, we counted the number of frames between the first frame with visible luminescence and the first frame where luminescence could not be seen any more. Finally, the interval between consecutive flashes was evaluated by counting the number of frames between the first frame with no luminescence (end of one flash) and the first frame with luminescence from the subsequent flash.

The flow velocity within the microfluidic device was measured using 1 μm diameter fluorescent beads (Bangs Laboratories, Inc., Fishers, IN, USA) as tracer particles. These measurements were done independently of the cell flashing experiments but under the same experimental conditions (driving pressures). The velocity of the beads was measured downstream of the barrier in channel 4 (Fig. 3.1C), where the flow channel dimensions were constant at 600 μm wide and 200 μm high. To evaluate the maximal flow velocity, v_{max}, we measured the length of the longest streaklines, corresponding to beads near the central axis of the channel. Knowing the maximum flow velocity and channel dimensions, the entire distribution as well as average flow velocity in the channel and volumetric flow rate can be calculated using the equations for fully developed laminar flow [Whi91].

Values are expressed as mean ± s.d. unless otherwise stated. Statistical comparisons were done using Statview software (SAS Institute, Inc., Cary, NC, USA) and involved one-way analysis of variance (ANOVA) with post-hoc pairwise comparisons using Fisher's protected least significant difference (PLSD), or unpaired t-tests. Statistical significance was based on a P value of 0.05.

RESULTS

Numerical simulations. Numerical simulations were performed for maximum flow velocities, v_{max}, of 10, 20, and 40 mm/s in the 200 μm deep portion of channel 4. Because the characteristic Reynolds number (Re) in the flow, $Re = v_{max}h/\nu$, was always low ($Re \approx 4$ at $v_{max} = 20$ mm/s), a linear flow regime was expected. Indeed, the force exerted by the flow at the sphere at the barrier, F_b, was found to be proportional to v_{max}. The coefficient of proportionality between F_b and v_{max} was calculated to be 7.2x10^{-6} kg/s, or 7.2 nN s/mm in more practical units, with a fractional error of 7%. The direction of

the force was at 38° from the x-axis towards the bottom of the channel (-38° from the x-axis in the xz-plane). For example, for $v_{max} = 20$ mm/s, the x-component, z-component, and absolute value of F_b were calculated to be 113±10 nN, -88±8 nN, and 143±10 nN, respectively. The force exerted at the sphere by the flow is balanced by the reaction and friction at the barrier and the bottom of the channel.

For the sphere at $\Delta x = 30$ μm in front of the barrier and $\Delta z = 30$ μm above the bottom of the channel (Fig. 3.2B) at $v_{max} = 20$ mm/s, the two components of velocity of the sphere were $v_y = 24.4$ mm/s and $v_z = -22.2$ mm/s. The velocity was directed almost precisely along the bisector of the angle formed by the barrier and the bottom of the channel. Because of the symmetry of the flow with respect to the position of the sphere, we assumed that the principal axis of the tensile force exerted by the flow on the sphere was parallel to the direction of the motion of the sphere. To evaluate the tensile force, we numerically calculated the local force exerted by the moving liquid on different elements of the surface of the sphere and divided the sphere surface into two domains, with positive and negative projections of the local force onto the principal axis. The tensile force exerted on the sphere was calculated as a numeric integral of projections of the surface force onto the principal axis over the domain where the projections were positive. At $v_{max} = 20$ mm/s, the tensile force was $F_a = 3.0$ nN. A numeric integral over the domain with negative surface force was -3.0 nN, and the net force exerted by the flow on the sphere was zero, as imposed by the numeric simulation protocol.

When linearly extrapolated to $v_{max} = 11$ mm/s (a typical experimental value), the results of the simulations for a cell at $\Delta x = 30$ μm in front of the barrier give the force $F_a = 1.6$ nN and velocity $v_y = 13.4$ mm/s and $v_z = -12.2$ mm/s. For a cell at the barrier at the same flow conditions, the simulations predict a force $F_b = 79$ nN. Because the sphere accelerates as it approaches the barrier, the time required for it to reach the barrier is less than $\frac{\Delta z}{\nu_z} = 2.5$ ms. Therefore, the results of the simulations suggest that at the typical experimental conditions, the mechanical stimulus experienced by a dinoflagellate reaching the barrier increases about 48 fold (from $F_a = 1.6$ nN to $F_b = 7$ 9nN) within less than 2.5 ms. In the lowest flow rate experiment, which had a flow velocity $v_{max} = 5.7$ mm/s, the hydrodynamic force at the barrier was calculated as $F_b = 40$ nN.

Table 3.1: Summary of experimental results for initial flashes produced by different strains of dinoflagellates at different flow velocities.

Flow velocity,v_{max} (mm/s)	Response latency (ms)	Minimum latency (ms)	Flash duration (ms)
Lingoludinium Polyedrum HQ			
5.7±0.9	31.3±8.4 (83)	16	41.0±33.0 (171)
11.2±0.8	24.8±4.2 (85)	16	38.0±9.8 (100)
15.1±1.4	15.2±2.5 (122)	13	69.0±15.0 (53)
35.0±5.0	15.6±2.6 (111)	12	72.0±24.0 (31)
60.5±3.4	15.3±2.3 (99)	12	77.0±18.0 (11)
L. polyedrum CCMP1932			
47.0±2.0	22.1±11.5 (144)	12	
L. polyedrum CCMP407			
35.0±5.0	15.2±4.6 (136)	8	
Pyrodinium bahamense			
39.0±4.0	22.3±4.8 (126)	16	
Alexandrium monilatum			
34.0±2.0	15.2±2.8 (133)	12	

Values of flow velocity are best estimates ± uncertainties of the measurements. Response latency is presented as mean s.d., with the number of analyzed flashes in parentheses. The uncertainty for the minimum latency is 3 ms. Flash duration of the first flash is only for cells responding with at least three flashes; values are mean s.d., with the number of analyzed flashes in parentheses.

Experimental results for *L. polyedrum* strain HJ. Bioluminescence in the test region was only observed when dinoflagellate cells encountered the barrier (Fig. 3.3; supplementary material movie 1). For the experiment with the lowest v_{max} = 5.7 mm/s, approximately half the cells encountering the barrier responded with a flash. For the cells that produced flashes at this v_{max}, a majority (65%) had a relatively fast response (latencies <60 ms) and a latency of 31.3±8.4 ms (Table 1; Fig. 3.4A). The remaining cells produced a relatively slow response, with a latency of 285.4±180.0 ms (N=44). At a higher flow rate (v_{max} = 11 mm/s), most of the cells encountering the barrier produced a flash, and the fraction of the cells displaying fast responses (86%) was higher than at v_{max} = 5.7 mm/s (Fig. 3.4B). The latency of the fast responding cells was 24.8±4.2 ms (Table 3.1) and slowly responding cells had a response latency of 257.0±80.7 ms (N=14).

In experiments with v_{max} = 15 mm/s, all responses were fast and the distribution

of response latencies was narrow (Fig. 3.4C). For example, at $v_{max} = 35$ mm/s, the response latency ranged from 12 to 21 ms, with an average of 15.2 ms (Table 3.1). There was no significant difference in response latency among experiments with three highest v_{max} of 15, 35 and 61 mm/s (ANOVA, $F_{2,329} = 0.939$, $P = 0.392$). For the pooled data, the response latency was 15.4±2.4 ms ($N = 332$). The mean response latency was a decreasing function of the flow velocity with saturation at $v_{max} = 15$ mm/s (Table 3.1; Fig. 3.5).

We also evaluated the minimum response latency, representing the most rapid response by a cell to the mechanical stimulus at each test condition (Table 3.1; Fig. 3.5). For experiments with $v_{max} \geq 15$ mm/s, the minimum latency was 12 ms (i.e. three video frames at 250 frames/s). At lower flow speeds, the minimum latency increased, reaching 16 ms (i.e. four frames at 250 frames/s) at the lowest flow velocity of $v_{max} = 5.7$ mm/s.

The duration of luminescent flashes following the encounter with the barrier varied with flow velocity (Table 3.1). Interestingly, there was no significant difference in the duration of the flashes at $v_{max} = 15$, 35 and 61 mm/s (ANOVA, $F_{2,92} = 1.025$, $P = 0.363$), the range of velocities where the response latency was saturated at a low value (Table 3.1; Fig. 3.5). However, the flash durations for the pooled data at these three high velocities (70.6±18.9ms; $N = 95$) were significantly different (t-test, $t_{364} = 10.365$, $P < 0.0001$) from and 78% greater than those at the two lower velocities (39.9±26.5ms; $N = 271$ for the pooled data at $v_{max} = 5.7$ and 11 mm/s). Thus, larger hydrodynamic drag on cells at the barrier generally resulted not only in shorter latencies but also in longer duration flashes.

Experimental results for other dinoflagellate strains. Measurements of the response latencies of newer and older strains of *L.* polyedrum isolated from the Scripps Pier were performed within the range of flow speeds ($v_{max} \geq 15$ mm/s) where latency values for strain HJ were nearly constant. For the older strain CCMP407, isolated in 1970, the response latency at v_{max} of 35 mm/s was 15.2±4.6 ms, while a newer strain CCMP1932, isolated in 1998, had a response latency of 22.1 ±11.5 ms for $v_{max} = 47$ mm/s (Table 3.1). There was a significant difference in response latency for the three strains (ANOVA, $F_{2,609} = 38.672$, $P < 0.001$) because the latency for strain CCMP1932 was significantly different (Fisher's PLSD, $P < 0.0001$) and greater than the response latencies of strains HJ and CCMP407, which were not significantly different from each other (Fisher's PLSD,

$P = 0.735$). The minimum response latency was 12 ms for strains CCMP1932 and HJ, and 8ms for strain CCMP407 (Table 3.1).

We also measured the response latencies of two other similarly sized thecate dinoflagellate species, *Pyrodinium bahamense* and *Alexandrium monilatum* (Table 3.1). The 22.3±4.8ms response latency of *P. bahamense* was greater and significantly different (Fisher's PLSD, $P < 0.001$) from the 15.2±2.8 ms latency of *A. monilatum* and that of *L. polyedrum* strains HJ and CCMP407 but was not significantly different from the latency of *L. polyedrum* strain CCMP1932 ($P = 0.883$). The response latency of *A. monilatum* was not significantly different from those of *L. polyedrum* strains HJ and CCMP407 ($P \geq 0.846$).

Multiple flashing. The response latencies and flash durations reported above were determined for the initial flash produced by cells after they encountered the barrier. Yet it is known that *L. polyedrum* and other dinoflagellates can produce more than one flash with mechanical stimulation [WC81, LL95, LJ96]. In our microfluidic device many cells were observed to generate multiple luminescent flashes at the barrier. We investigated multiple flashing in detail for cells of *L. polyedrum* strain HJ, which flashed as many as four times within ˜1 s after reaching the barrier. Flashes that might have occurred later were not registered, because our observation window was limited by the 300 frame buffer for video capture. Interestingly, the number of flashes produced by a cell at the barrier never exceeded two at the two highest flow velocities ($v_{max} = 35$ and 61 mm/s; $N = 374$), whereas the number of flashes reached four at the three lowest velocities ($v_{max} = 5.7$, 11 and 15 mm/s; $N = 491$ for the pooled data).

For cells that flashed three or four times ($N = 98$ cells), the flash duration for pooled data was 43.8±13.2 ms ($N = 304$). There was a significant variation in flash duration with flash number (Fig.6A; ANOVA, $F_{3,300} = 17.169$, $P < 0.0001$). The duration of the first flash (36.7±8.7 ms; $N = 98$) was significantly different from and smaller than that of the second to fourth flashes (47.3±13.6 ms; $N = 206$), which were not significantly different from each other (Fisher's PLSD, $P \geq 0.156$). There was a significant difference ($t_{194} = 5.829$, $P < 0.0001$) in the interval between 1^{st} and 2^{nd} flashes (117.5±52.1ms; $N = 98$) and that between the second and third flashes (65.8±70.5 ms; $N = 98$; Fig. 3.6B). As only 11 out of 98 cells were observed to flash four times, the interval between the third

and fourth flashes (83.8±33.0 ms) represented only a small subpopulation and was not used for statistical comparison. The minimum interval was 4 ms between first and second flashes and 6 ms between second and third flashes.

DISCUSSION

Dinoflagellate response latency and cellular signaling pathway. The 15-22 ms response latency for dinoflagellate bioluminescence may be adaptive in terms of the ecological role of light emission as a predator defense to reduce the grazing rate of visual predators [EC72, Whi79] by altering their swimming to disrupt typical feeding behavior [BMS83, BS83]. Mechanical stimulation of bioluminescence appears to occur by direct predator contact [LNR04, vDBL05]. Presumably a rapid response after contact with the predator increases the probability that a cell may escape from a predator prior to ingestion.

The characteristic response latencies measured for the tested dinoflagellates are similar to those of other aquatic organisms responding to mechanical stimuli in the context of predator avoidance. Minimum response latencies for rapid escape behaviors in aquatic organisms include 10-30 ms for fish startle escape behavior [BB85, EDN88, PF03], 10 ms latency for crayfish responding to tactile stimuli [WK72], 30 ms for the shadow response of copepods [BH03], and 7 ms for the tail withdrawal reflex of a polychaete [ZD88]. The 2-4 ms latency for copepod escape behaviors represents some of the most rapid responses [HBL99, LH99, BLH02]. These rapid behavioral responses involve specialized neural networks including giant nerve fibers and myelinated nerves [ZD88, LHD00, WDHL00].

The response latency in dinoflagellates reflects a complex series of cellular events triggered by mechanical stimulation. The timing of the individual steps of the signaling pathway was not resolved in our experiments. The timing is best understood for the large dinoflagellates *Noctiluca scintillans* and *Pyrocystis fusiformis* based on measurements of individual cells impaled by an electrode. In *N. scintillans* the overall response latency is 16-19 ms, with about a 15 ms delay between mechanical stimulation and the tonoplast action potential [ES68] and a 1-3 ms delay between the tonoplast action potential and initial light emission [Eck65b, Eck65a, Eck66]. In *P. fusiformis* the overall response latency is about 17 ms, with a 5 ms delay between mechanical stimulation and the tonoplast action potential and a 12 ms delay between the action potential and the initial production of bioluminescence

[Wid81]. The uncertainties in these values are not stated, so it is unknown to what extent the dissimilar timing for the two phases of the bioluminescence signaling pathway in *N. scintillans* and *P. fusiformis* is due to biological variability, methodological differences, or the unusual morphologies of these two non-thecate species [Eck66, ES68, SR70, SF00].

The morphologies of the species of dinoflagellates tested in our study are typical of thecate dinoflagellates [Net84, Spe84]. It was expected that these smaller dinoflagellate species would have shorter latency times because of reduced diffusion distances of ions and a smaller surface area of the tonoplast membrane over which the action potential is propagated. However, their response latencies were similar to those of the larger species, perhaps reflecting the ecological value of dinoflagellate bioluminescence as a predator avoidance strategy. The minimum bioluminescence response latency is of interest because it represents the most rapid activity of the signaling pathways. CCMP407, the oldest strain of *L. polyedru*m, had the shortest minimum latency at 8 ms, while the other strains of *L. polyedrum*, as well as *A. monilatum*, had a minimum latency of 12 ms.

At low flow speeds the response latency of *L. polyedrum* HJ increased sharply. This response pattern is classically known for the electrical stimulation of neurons [Aid98] and is generally expected of a physiological response in that weaker stimuli will lead to a longer response latency. The pattern is consistent with the bioluminescence responses in fireflies [BHC63], where bioluminescence is mediated through the nervous system and the response latency increases from 10 to 30 ms with decreasing strength of the electrical stimulus. This pattern also occurs with other classes of sensory stimuli, including hearing [Hoy89, SPRR98] and vision [ADH$^+$93].

Analysis of forces exerted on cells encountering the barrier. A dinoflagellate cell encountering the barrier experiences mechanical stimuli of two kinds. The stimulus of the first kind originates from the hydrodynamic drag on the immobilized cell that lasts as long as the cell stays at the barrier. As follows from the numerical simulations, for $v_{max} = 11$ mm/s the hydrodynamic drag amounts to a total force $F_b = 79$ nN. The other stimulus is short term and originates from the impulse associated with impact. When a cell comes to a sudden stop at the barrier, there is an inertial force due to the change in momentum. The magnitude of the inertial force can be estimated as $F_{in} = p/\Delta t$, where p

is the momentum of the cell, the product of its mass and velocity, and Δt is a characteristic time in which the velocity of the cell is reduced from its initial high value to zero. The mass, m, of a cell with a radius of 17.5 μm and density of 1084 kg/m^{-3} (Kamykowski, Reed et al. 1992) is 2.4 x 10^{11} kg, resulting in $p = 4.1$ x 10^{-13} kg m/s or 4.1 x 10^{-4} nNs for a cell moving at $v_c = 17$ mm/s (the absolute value of velocity calculated for $\Delta x = 30$ μm and $\Delta z = 30$ μm upstream from the barrier at $v_{max} = 11$ mm/s). For this inertial force to be equal to the hydrodynamic drag, F_b, the impact has to last $\Delta t = p/F_b = 5$ ms, corresponding to a distance $\Delta x = v_c \Delta t = 0.085$ μm for a cell moving at $v_c = 17$ mm/s.

When a cell comes close to the barrier, the liquid in a thin layer between the cell and the barrier is squeezed radially outwards at a high speed, producing large shear and a region of increased pressure between the cell and the barrier that results in a substantial resisting force [Bre61]. To model the motion of a cell near the barrier, we again approximate the cell as a sphere with $R = 17.5$ μm and approximate the barrier by an infinite surface in the yz-plane. It is a reasonable approximation, when the distance between the sphere and the barrier is substantially less than $\sim$2.5 μm, the difference between R and the channel depth under the barrier. The resisting force experienced by the sphere moving at a speed v is inversely proportional to the distance from the barrier, x, and is given by $F_r = -6pR^2 v\mu/x$ [Bre61], where μ is the viscosity. For $v = v_c = 17$ mm/s and $x = \Delta x = 0.085$ μm, we calculate the resisting force as $F_r = 1150$ nN that is ˜14 times greater that the hydrodynamic drag at the barrier, $F_b = 79$ nN. Therefore, the resisting force near the barrier is expected to become comparable with F_b at distances, x, much greater than $\Delta x = 0.085$ μm, resulting in the impact duration substantially larger than $\Delta t = 5$ ms, and the impulse during the impact substantially smaller than the eventual drag force at the barrier, F_b. Because of the relatively low value of the impulse and short duration of the impact (still much less than 1 ms), the impulse associated with the impact is likely to be of relatively minor significance for the mechanical stimulation of the cells. This suggestion is supported by the observation of multiple flashing of cells immobilized at the barrier and exposed to a steady drag.

Minimum interval between repeated flashes versus minimum response latency. Dinoflagellates, including *L. polyedrum*, are known to produce more than one flash upon maintained mechanical stimulation ([WC81, LL95, LJ96], but it has been assumed

that the refractory period between repeated flashes would be long in comparison to the flash duration. For cells of *L. polyedrum* trapped at the barrier and experiencing steady hydrodynamic drag, the interval between first and second flashes was 117.5±52.1ms and the interval between second and third flashes was 65.8±70.5ms. Most surprisingly, the minimum interval between flashes was 4 ms, substantially less than the minimum response latency of 12 ms. We hypothesize that repeated flashing involves reactivation of only a subsystem of the entire mechanosensory signaling pathway. One possible candidate is the re-activation of the tonoplast action potential, which has a one-to-one association with a flash [Eck65b, WC81]. Another possibility is that the rate of repeat flashing is limited by the need to restore physiological pH within the cell, because the protonmediated tonoplast action potential leads to acidification of the cytoplasm, which activates the luminescent chemistry [HD86, WH98]. Thus cytoplasm pH must be restored to a physiological level, presumably by tonoplast membrane-associated ATPases that pump protons back into the vacuole.

Comparing mechanical simulation in the microfluidic device to previous flow experiments. To connect the results of this study with previous work on dinoflagellate bioluminescence in fully developed pipe flows, it is instructive to compare the stimuli experienced by a motionless cell at the barrier in the microfluidic device and by a moving cell experiencing shear in fully developed laminar pipe flow. Just as for a cell at the barrier, a cell in shear flow can be modeled as a sphere with radius $R = 17.5$ μm, neglecting any active motion of the cell with respect to the flow. In this case, the net force on the cell is zero, and the cell can be divided into two hemispheres experiencing equal tensile forces, $F = (5/2)\pi R^2\gamma\mu = (5/2)pR^2\tau$, in opposing directions [CL03], where γ is the shear rate and τ is the shear stress in the flow. In previous studies, cell response was related to flow properties rather than forces acting on the cell. For example, in pipe flow *L. polyedrum* luminescence was first detectable in flows where the wall shear stress, τ_w, was about 0.3 N/m^2 [LR99]; this level corresponds to a tensile force $F = 0.7$ nN on each hemisphere of a cell. The fraction of flashing cells at the threshold was estimated as 0.0002 and it increased to 0.11 at $\tau = 1$ N/m^2, corresponding to a tensile force $F = 2.3$ nN; the fraction remained at a level of ∼0.1 up to the highest shear stress tested, ∼20 N/m^2,corresponding to $F \approx 50$

nN.

The mechanical stimuli applied to cells in our study were always substantially above the level at which the fraction of luminescent cells in the pipe flow reached the value of ∼0.1 [LR99]. At the lowest tested flow velocity, $v_{max} = 5.7$ mm/s, the estimated hydrodynamic force exerted on a cell at the barrier was $F_b = 40$ nN. The fraction of flashing cells at these conditions was ∼0.5, substantially higher than at the highest shear stress in pipe flow, and it further increased at higher v_{max} and F_b. The discrepancy in the fractions of flashing cells between the two experiments could be partly due to different observation conditions (imaging of quickly moving versus motionless cells). Furthermore, quantitative comparison between stimuli experienced by a stationary dinoflagellate at the barrier in the microfluidic device and one moving in shear flow is somewhat problematic, because of different distribution of hydrodynamic stress over the cell surface in these two situations. The application of relatively strong stimuli resulted in a high yield of luminescent cells and allowed us to observe the saturation in the response latency at $v_{max} \geq 15$ mm/s. Thus, it was consistent with the objectives of this study to observe bioluminescent response of a large number of individual cells and to measure the minimal latency.

The response latency and luminescent flow visualization. Dinoflagellate bioluminescence is a useful flow visualization tool for conditions involving levels of shear stress above 0.1 N/m^2, such as the boundary layer flow on a moving dolphin [RLF$^+$98], high shear regions in bioreactors (Chen, Latz et al. 2003), and shear within a breaking wavecrest [SDLR04]. By developing a statistical model of the mechanical stimulation of dinoflagellate bioluminescence [DS05], it can be used for quantitative estimates of shear or dissipation. Because high shears usually occur at high flow speeds, the response latency can lead to considerable downstream advection of organisms from the points of their original stimulation before the luminescence starts. This effect is necessary to take into account this effect for reconstruction of the flow field from the distribution of bioluminescence. For example, in a nozzle flow with a speed of 2 m/s [LJA$^+$04], a response latency of 15 ms would result in distances as long as 3 cm between the regions of high shear where cells are stimulated and the regions where cell flashes are observed [LJA$^+$04]. The information on dinoflagellate response latency obtained in this study can be incorporated into models

relating dinoflagellate bioluminescence intensity to flow fields that cannot be measured using conventional techniques [DS05].

CONCLUSIONS

The present work used a specially made microfluidic device to study the short-time dynamics of mechanosensing of motile dinoflagellates. A hydrodynamic drag was applied to individual cells with a millisecond inception time and the bioluminescence of the cells was recorded and used as a reporter of their response to this mechanical stimulus. The 15-22 ms response latencies observed with different strains of dinoflagellates are similar to those of other aquatic organisms to mechanical stimuli in the context of predator avoidance. This is intriguing because dinoflagellates are protists that appear to use a G-protein-mediated transduction system for mechanosensing. When stimulated continuously, cells often produced multiple flashes with intervals that were sometimes shorter than the initial response latency, suggesting that only a subset of the signal transduction pathway is involved in repeat flashing. Dinoflagellate bioluminescence could serve as a model system for understanding mechanosensing in simple eukaryotes, and the experimental techniques developed in this study could also be applied to studies of mechanosensing in different types of cells and in multicellular organisms.

ACKNOWLEDGEMENTS

This work was partially supported by NSF grant OCE-0428900 to A.G. and by IA funds through SSC San Diego. M.B. was supported by a Naval Research Enterprise Intern Program (NREIP) fellowship through the Office of Naval Research.

Chapter 3, in full, is a reprint of the journal article Bioluminescent response of individual dinoflagellate cells to hydrodynamic stress measured with millisecond resolution in a microfluidic device in Journal of Experimental Biology, 2008. Latz, Michael; Bovard, Michelle; VanDelinder, Virginia; Segre, Enrico; Rohr, Jim; Groisman, Alex. Dissertation author was a participating investigator of this paper.

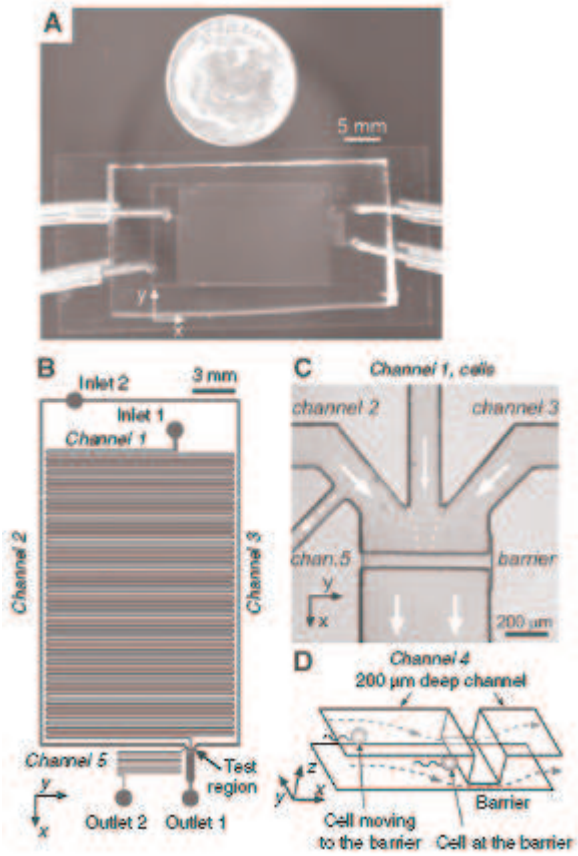

Figure 3.1: The microfluidic device. (A) Microfluidic device and portion of connected tubing, shown with a dime for scale (17.91 mm in diameter). (B) Drawing of microchannels in the device. (C) Micrograph of test region, showing flow channels and barrier. Solid arrows indicate direction of flow in the device during its normal operation. Dashed arrow shows flow in channel 5 during the removal of cells from the barrier. Dashed lines mark the boundaries between streams from channels 2, 1 and 3. (D) Schematic three-dimensional drawing of barrier and cells (not to scale). Curved dashed lines are flow lines with arrows indicating flow direction. B and C are rotated 90 deg. counterclockwise with respect to A and D, as indicated by the orientation of the x- and y-axis shown in the panels.

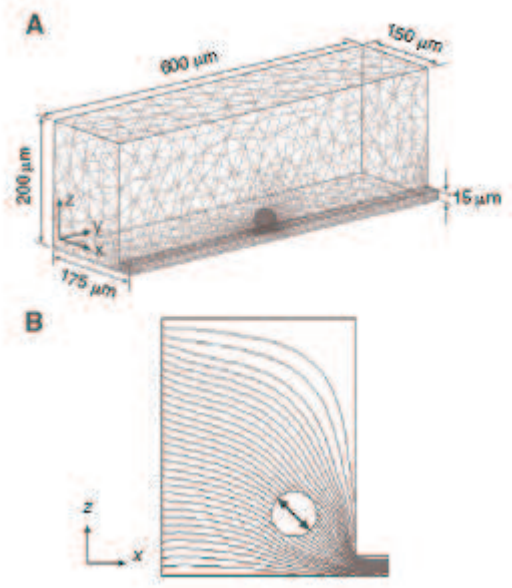

Figure 3.2: Numerical simulations. (A) Three-dimensional schematic drawing of the segment of channel 4 used in the numeric simulations with a motionless sphere at the barrier. The mesh used in the simulations is shown by thin lines. (B) Two-dimensional cross-section of the channel in the xz-plane of symmetry (vertical midplane) with a freely moving sphere at (-30, 0, 30) μm from the rest position. Curved lines are the streamlines with the flow directed from left to right. Double-headed arrow shows the principal axis of tensile forces exerted at the sphere by the hydrodynamic stresses. Note the minimal bending of the streamlines in the vicinity of the sphere, as the sphere is moving together with the fluid.

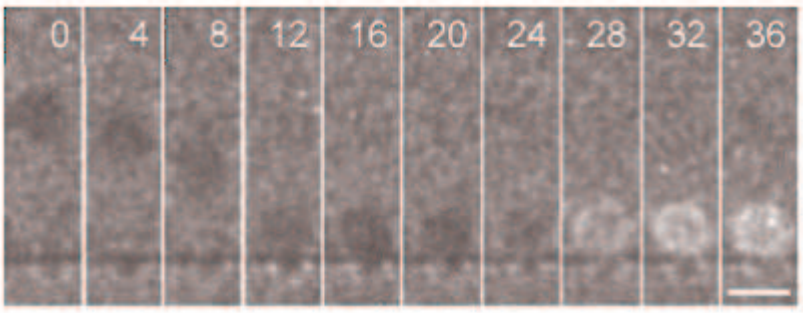

Figure 3.3: Sequence of video frames of a single cell of *Lingulodinium polyedrum* strain HJ approaching the barrier (dark horizontal line near the bottom). Flow direction is from top to bottom. Frames were taken with an interval of 4 ms; the numbers at the top of each panel show elapsed time in milliseconds. The cell arrived at the barrier at 12 ms and the flash started at 24 ms, resulting in a latency of 12 ms. Scale bar, 50 μm.

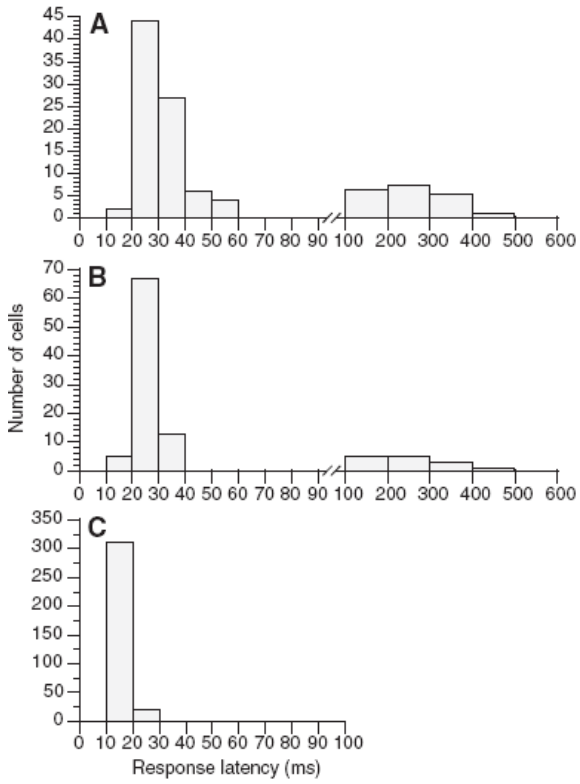

Figure 3.4: Frequency distribution of response latency for *Lingulodinium polyedrum* strain HJ. (A) Response latency for the experiment with the lowest flow velocity of $v_{max} = 5.7$ mm/s. (B) Response latency for the experiment with a flow velocity of $v_{max} = 11$ mm/s. (C) Response latency for the experiments with the highest flow velocities ($v_{max} = 15$, 35 and 61 mm/s). Bin width is 10 ms between 0 and 100 ms latency and 100 ms between 100 and 600 ms latency.

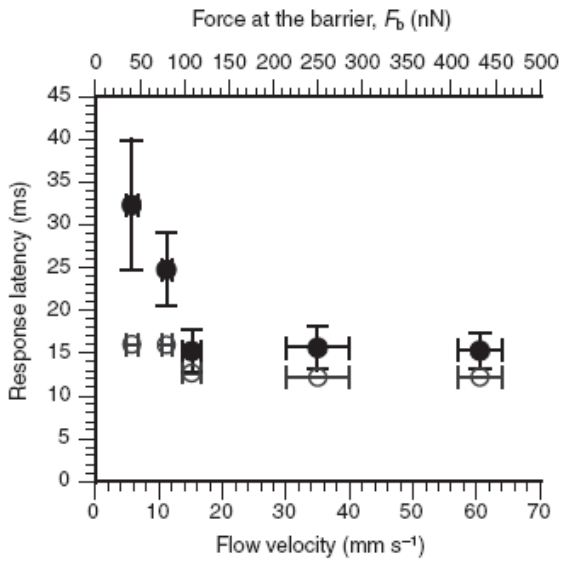

Figure 3.5: Response latency of *Lingulodinium polyedrum* strain HJ as a function of flow velocity, v_{max}. Values represent the mean response latency (filled circles) and the minimum response latency (open circles). The y-axis error bars are s.d. of the response latencies, and the x-axis error bars are uncertainties of the flow velocity measurements.

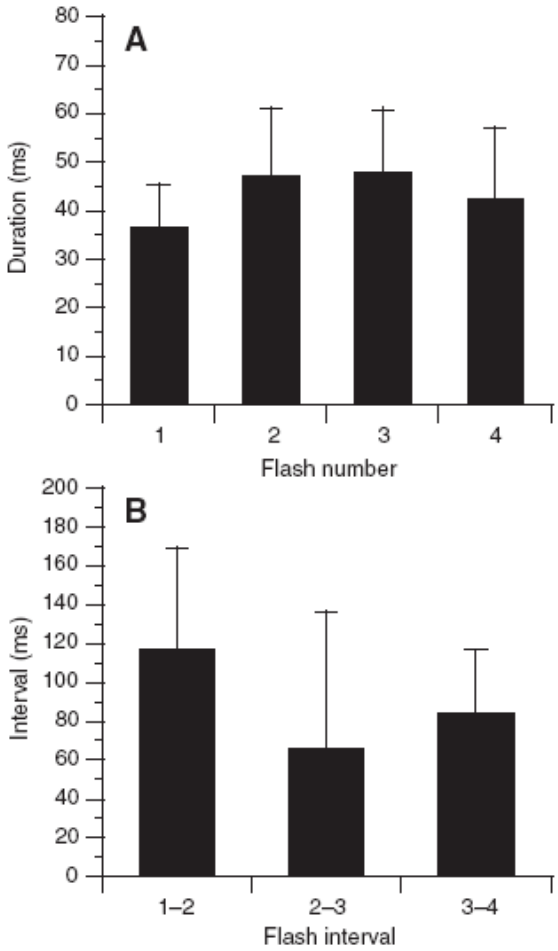

Figure 3.6: Multiple flashes from individual cells of *Lingulodinium polyedrum* strain HJ. Data were collected for cells that flashed three or four times at $v_{max} = 5.7$, 11 and 15mm/s. (A) Duration of each flash as a function of flash number. Values are means ± s.d. ($N = 98$ for flashes one to three; $N = 11$ for flash four). (B) Length of interval between consecutive flashes. Values are means ± s.d. ($N = 98$ for the intervals between the first and second and between the second and third flashes; $N = 11$ for the interval between the third and fourth flashes).

Chapter 4

Microfluidics for protein folding studies

4.1 Microfluidic device for single-molecule fluorescence experiments with enhanced photostability

We present a microfluidic platform made of polydimethylsiloxane (PDMS) that addresses key limitations in single-molecule fluorescence experiments by providing high dye photostability and low sample sticking. Photobleaching is dramatically reduced by deoxygenation via gas diffusion through porous channel walls. Rapid buffer exchange in a laminar sheath flow immediately followed by optical interrogation minimizes surface-sample contacts, and allows in situ combination and addition of other reagents such as triplet quenchers.

Single-molecule Frster resonance energy transfer (smFRET) experiments can elucidate biomolecular structure and dynamics with a resolution beyond the reach of common ensemble techniques [DML08]. The quality of the smFRET signal depends on the number of emitted photons, which is generally limited by photobleaching of the fluorescent dyes. As a substantial fraction of photobleaching pathways are mediated by molecular oxygen [EWB$^+$06, RMH06, KNHW07, VKS$^+$08], a common remedy is the addition of an enzy-

matic oxygen scavenging system. However, such systems are incompatible with a variety of experimental designs, e.g. protein folding studies requiring denaturants. Moreover, removal of oxygen can result in increased triplet lifetime and other non-fluorescent "dark" states, which is detrimental to signal quality but can be suppressed using β-mercaptoethanol, Trolox or ROXS [RMH06, VKS$^+$08]. While beneficial for dye stability, additives alter the chemical environment of the sample, can interfere with biological function and contribute to autofluorescent background.

Another limitation in single-molecule experiments is that proteins often have a strong tendency to adhere to surfaces, which can severely complicate or even make experiments impossible by depleting molecules or specific structural subpopulations. This problem is particularly pervasive because of long measurement times and the large ratio of surface area to the number of molecules in freely diffusing smFRET experiments, a popular technique that is utilized in this work. Adhesion problems can be mitigated by various surface coatings[RMH05], but these typically need to be optimized for specific proteins and medium conditions.

Here we report a microfluidic device made of a single cast of silicone elastomer PDMS sealed to a microscope cover glass that adresses both the above problems, providing a high-performance platform for smFRET measurements. Using diffusive mixing in a laminar sheath flow [KVBA98], the sample is rapidly transferred from the loading buffer into the measurement buffer and immediately measured, preventing exposure to surfaces. Photostabilizing additives are supplied only to the measurement buffer, reducing interaction times with the biological sample to a minimum. Most importantly, sample solution and sheath buffer are deoxygenated in the device without the use of enzymes or other additives, such as propylgallate and mercaptoethylamine [RMH05, KNHW07, VKS$^+$08]. Oxygen diffuses out of the solutions through porous PDMS walls into neighboring channels that are continuously ventilated with pure nitrogen. Furthermore, the two components of ROXS (the oxidizer methyl viologen (MV) and reductant AA) are mixed in situ and used within $<$10 s, prior to their degradation.

The microfluidic device (Fig. 4.1) has a network of flow channels with depth $h = 80$ μm for sample solution and buffers. The fluorescently tagged sample is fed into the sample

inlet and MV and AA are fed into the two buffer inlets (Fig. 4.1a). The streams of the two components merge and proceed through a long channel, where they mix by diffusion. The flow of the ROXS mixture is evenly split into two channels and directed to the mixing junction (Fig. 4.1a,c), where the sample stream is sandwiched laterally between the two streams of ROXS. The volumetric flow rate of the sample solution is substantially lower than of the ROXS buffer, so the sample solution stream is squeezed to a width of $w_p < 1$ μm. This small width leads to buffer exchange (diffusive elution of small molecules such as salt from and addition of ROXS to the sample solution) at a time scale $t_{ex} = w_p^2/(8D) < 1$ ms, with the diffusion coefficient, $D = 5 \cdot 10^{-6}$ cm^2/s, a typical value for small molecules. The time the sample spends traveling from the junction to the 300 μm wide optical interrogation channel ($\sim$100 ms) is more than sufficient for buffer exchange but is substantially shorter than the time of diffusion of sample molecules to the side walls ($\sim$1s).

Deoxygenation is based on the high gas permeability of PDMS [MBN$^+$00, VPGT05] and provided by continuous flow of nitrogen through two 160 μm deep, 200 μm wide gas channels flanking the flow channels upstream of the junction. To maximize the lateral diffusion of oxygen from the flow channels into the gas channels and to minimize the exposure of the flow channels to oxygen, the flow channels are made narrow (40 μm) and the distance between the flow and gas channels is made small (100 μm, Fig. 4.1b). Numerical simulations predicted that at equilibrium, the oxygen concentration, [O_2], in the flow channels is $\sim$0.3% as compared to $\sim$21% for a solution saturated with air. The length of the segments where the flow channels are flanked by the gas channels (Fig. 4.1a) was made sufficient to reach this equilibrium. Experimental tests with an oxygen-sensitive fluorescent dye [SMM$^+$06b, MMS$^+$07] showed that at typical flow velocities of smFRET experiments, [O_2] in the optical interrogation area was indistinguishable from zero at an experimental uncertainty of $\sim$0.5% (See the Methods section for more details about the design, fabrication, operation and testing of the device).

We first tested the microfluidic device using two common dyes, Alexa488 (donor, D) and Cy5 (acceptor, A), attached 9 base pairs apart to rigid duplex DNA. The excitation power was set to a relatively high level at which photostability is a major limitation for smFRET. A smFRET histogram of this sample without additives measured in a standard

cuvette exposed to atmosphere air exhibits two peaks (Fig. 4.2a). The low amplitude peak at $E_{FRET} = 0.41$ (FRET peak) originates from FRET in properly labeled DNA molecules. The peak at $E_{FRET} = 0$ (zero peak) originates from events without acceptor signal, which can occur due to insufficient labeling, inactivation of acceptors by photobleaching or transition into dark states. Strikingly, when the same DNA sample was tested in the microfluidic platform with deoxygenation, the relative amplitude of the zero peak was reduced ∼50-fold and became smaller than the FRET peak (Fig. 4.2b). The use of ROXS in addition to deoxygenation further improved the data by increasing the brightness, which raised the signal-to-noise ratio and reduced the width of the FRET peak from 0.17 to 0.12 (Fig. 4.2b vs. Fig. 4.2c and Fig. 4.3). The width reduction was accompanied by a shift of the peak position from 0.41 to 0.46, which is in line with the reported reduced blinking of the dyes[KNHW07] and our own observations using correlation spectroscopy (Fig. 4.3). Enhancement of the zero-peak in Fig. 4.2c vs. 4.2b was likely due to residual fluorescence of ROXS.

The FRET histograms in the left panel of Fig 4.3 show that the ratio between the zero peak and FRET peak improves when changing from the freely diffusing molecules in the cuvette to flow conditions in the device. This is expected, as e.g. reentry of molecules and prolonged residence in the focal volume are reduced by flow. Additional deoxygenation improves the zero peak to FRET peak ratio by an additional ∼3 fold (b vs c). The middle panel shows the raw data intensity trace with a binning time of 0.5 ms for the photon stream arriving in D (green) and A (red). The overall intensity of the bursts drops due to deoxygenation (b vs c), in line with enhanced blinking of the dyes.[RMH06, VKS$^+$08] A substantial fast fluctuating component is also visible in the cross-correlation function $G(\tau)$ (right panel) as indicated by an arrow. This component is suppressed by the mixing with ROXS and a brightness increase is also visible in the burst intensity trace. Additionally, the width of the FRET peak reduced from 0.17 to 0.12 (a vs d) and shifted by 0.05 to higher E_{FRET} which can be explained by the improved brightness of the dyes over background. The background fluorescence originates from autofluorescent species in the buffer, which was particularly notable in our experiments as we used a high laser power in all experiments (865 μW at the back pupil of the objective). This setting was chosen to be in a regime

were photostability of dyes are major concerns in order to illustrate the performance of the device.

Next, the performance of the device in denaturant conditions was tested with the protein T4Lysozyme, which was site specifically labeled with Alexa488 and Cy5 using a recently reported labeling strategy based on incorporation of the genetically encoded non-natural amino acid p-aceptylphenylalanine [BLSD08]. SmFRET experiments on a solution of the protein in a denaturing buffer (4M GdmCL, Fig. 4.2d-f) showed that similarly to the DNA experiments (Fig. 4.2a,b), the zero peak was reduced by deoxygenation in the microfluidic device (Fig. 4.2e vs 4.2d), revealing a low FRET signal that was hardly visible under standard cuvette conditions. We note that deoxygenation with an enzymatic system is not possible here because enzymes are not functional in the presence of 4M GdmCL. Next, a physiological buffer without GdmCL was fed to the buffer inlets, resulting in the removal of GdmCL from the protein solution in the buffer exchange channel, which led to folding of the protein, as evidenced by a substantial shift of E_{FRET} (Fig. 4.2e vs 4.2f and Fig. 4.4). Importantly, removal of the denaturant in the microfluidic device did not cause appreciable sample loss. In contrast, smFRET measurements for GdmCl concentrations lower than 1M were severely complicated by continuous and unpredictable sticking of the sample in the optical cuvette.

The presented device offers several important benefits for smFRET experiments as compared to standard techniques. First, efficient inhibition of oxygen-mediated photobleaching is achieved independent of solution composition (denaturant, ionic strength, or pH) and without additional chemicals. Second, loss and degradation of potentially highly adherent folded or other conformational states of molecules are minimized by rapid transfer from non-adherent conditions immediately followed by smFRET measurement. The short time interval between buffer exchange and optical interrogation minimizes concerns due to potential cross reactivity of additives and biological specimen. By increasing the flow velocity this observation dead time can be further reduced, making the device also a potential tool for studying kinetics on 25 ms - 1 s scale, which is among the fastest mixers for single molecule applications [LSBE03, HW08]. Third, the buffer for FRET measurements can be prepared by in situ mixing of two components, making the device compatible with ROXS

or other unstable mixtures with short lifetimes. Moreover, the sample consumption is extremely reduced, ∼200 μL buffer and ∼2 μL of a 0.1 μM protein solution per day, and the microfluidic chips are simple to operate, adjustable, inexpensive to fabricate, and reusable. Based on these multiple benefits, we anticipate this experimental platform to substantially extend the reach of single-molecule investigations of biological systems.

METHODS

Design of the microfluidic device. The microfluidic device was designed to deoxygenate solutions in the microchannels and achieve an oxygen-free environment in the optical interrogation region, where the FRET measurements are performed (Fig. 4.1 and Fig. 4.5). The deoxygenation occurred by molecular diffusion of oxygen, O_2, from the solutions in the flow channels through porous PDMS walls to nearby gas channels that were continuously ventilated with pure nitrogen, N_2. Unlike some previous designs, where microfluidic devices were made of two layers of PDMS and had two layers of microchannels, with gas channels positioned on top of flow channels [VPGT05, Pol08], the microfluidic devices used in the present study were made of a single cast of PDMS, with gas channels flanking the flow channels. The single-layer design substantially simplified the fabrication procedure, making it possible to produce microfluidic devices at a low labor cost and making the devices more durable and reusable.

In addition to reaching maximal deoxygenation, the dimensions and layout of the flow channels were chosen to provide optimized conditions for single molecule FRET spectroscopy in the measurement region and fast and efficient buffer exchange in a laminar sheath flow immediately upstream of the measurement region. The choice of the flow channels depth, 80 μm, was dictated by relatively high levels of autofluorescence of the cover glass at the bottom and PDMS chip at the top as compared to water. The autofluorescence could contribute to the FRET background, thus reducing data quality. The channel depth of 80 μm enabled positioning the region of confocal microscopy at a distance of 40 μm from both glass and PDMS, making it possible to optimize the detection sensitivity without appreciable increase in the fluorescence background. The width of the measurement channel was chosen at 300 μm, so the beams focused and collected by the high-NA objective used in the experiments (40x/1.2NA water immersion) would not be distorted by passing through

the PDMS side walls of the channel, which had a refractive index of ∼1.41 as compared to 1.33 for water.

The buffer exchange was initiated at the 4-channel junction (Fig. 4.1, 4.5d, 4.6, 4.7), where the stream of the sample solution was squeezed in a sheath between two streams of buffer coming from two sides. The sample and sheath channels were 30 μm wide at the junction. The sheathed sample stream travelled through a mixing channel to the measurement region. The mixing channel was 200 μm long and consisted of a 30 μm wide, 50 μm long upstream segment and a 40 μm wide, 150 μm long downstream segment.

The width of the sample solution stream in the 40 μm wide segment, w_p, was 1.8 μm, leading to diffusive exchange between the sample and buffer solutions at a time scale $t_{ex} = w_p^2/(8D)$ that was ∼1 ms for ROXS ($D = 10^{-15}$ cm^2/s) and ∼0.5 ms for the denaturant (GdmCl, $D = 10^{-5}$ cm^2/s). In the experiments reported in the paper, the flow velocity through the confocal volume was 0.9 mm/s, corresponding to the sample flow velocity of 6.8 mm/s in the 40 μm wide segment of the mixing channel and a time of ∼200 μm/6.8 mm/s = 29 ms ($\sim 68 \cdot t_{ex}$ for the denaturant) available for the buffer exchange. Numerical simulations (Fig. 4.6-8) indicated that the concentration of denaturant in the sample is reduced by 92% compared with its original value, and the concentration of ROXS reaches 90% of its value in the sheath buffer before the sample reaches the measurement region.

The time required for protein molecules in the sheathed sample steam to reach the side walls of the mixing channel by diffusion can be estimated as $t_{side} = w_m^2/(8D_{pr}) \approx 2$ s, where $w_m = 40$ μm is the width of the mixing channels and the diffusion coefficient of the protein molecules was conservatively estimated as $D_{pr} = 10^{-6}$ cm^2/s. Because $t_{side} >> 29$ ms, protein molecules were not expected to interact with the side walls. For protein molecules moving near the mid-plane of the channel, the transit time between the entrance of the mixing channel and the confocal volume (150 μm from the end of the 40 μm wide mixing channel) was estimated as ∼130 ms, corresponding a diffusion distance of ∼5.5 μm. This diffusion distance was substantially less than the 40 μm distances from the mid-plane to the top and bottom of the channel, precluding any sample loss due to interactions with the top and bottom channel walls after the buffer exchange.

The microfluidic device (Fig. 4.1, 4.5) had two buffer inlets for solutions of the oxidizer methyl viologen (MV) and reductant ascorbic acid (AA) that were mixed in the device to produce ROXS, a compound found to decrease dye blinking [VKS$^+$08]. Whereas each of the two components was chemically stable, ROXS was observed to degrade on a time scale of ∼10 min producing a solution with a significant autofluorescence background. We note that a soluble autofluorescent compound is much more of a concern for studies using freely diffusing molecules with confocal detection geometry (this study) than for the study of immobilized molecules (ref. [VKS$^+$08]). Therefore, to prevent the autofluorescence, MV and AA had to be mixed immediately before feeding the buffer with ROXS to the measurement region. To mix the two components, the microchannels connected to the two buffer inlets merged into a single microchannel with a length $L_m = 62$ mm, and width $w_m = 40$ μm. Because both MV and AA are small molecules with diffusion coefficients $D_{rx} \approx 5 \cdot 10^{-6}$ cm^2/s, the time of mixing by diffusion in the channel was estimated as $t_{rx} = w_m^2/D_{rx} = 3.2$ s. Therefore, the mixing was expected to be complete by the end of the channel, when mean flow velocities in the channel, $\bar{\nu}$, was below $L_m/t_{rx} \approx 19$ mm/s, corresponding to a flow velocity of 4.6 mm/s through the confocal volume at the measurement point. In the experiments reported in the paper, the flow velocity through the confocal volume was 1 mm/s, corresponding to $\bar{\nu} = 4.2$ mm/s in the ROXS mixing channel and suggesting that the mixing of ROXS was complete. The transit time between the entrance of the ROXS mixing channel (where MV and AA first start interacting to form ROXS) and the measurement point, estimated as the sum of ratios of channel segment lengths to the mean flow velocities in them, was ∼42 s, which was substantially less than the degradation time of ROXS (Fig. 4.5a,c).

In general, our device allows for slow mixing of two buffers separately and fast mixing with the sample buffer. When using additives (such as ROXS, Propylgallate, mercaptoethylamine) this approach minimizes the contact time with the biological sample to the actual measurement time point, rather than supplying the additive directly with the sample. Certainly, the combination of a slow and a fast mixer also allows for a variety of experimental designs to study e.g. formation of biological complexes.

Deoxygenation in the microfluidic device. When designing the device and

estimating the deoxygenation, we used values of $D_w = 2 \cdot 10^{-5}$ cm^2/s for O_2 diffusivity in water, 1.3 mM for O_2 solubility in water at 25 °C at O_2 partial pressure of 1 atm (pure oxygen), and 18% for O2 solubility in PDMS (effective porosity of PDMS) (Merkel, Bondar et al. 2000). This porosity corresponds to the concentration of oxygen, $[O_2]$, in PDMS of 0.18/22.4 M = 8.04 mM when PDMS is saturated with pure O_2 at 1 atm, and ∼6 times higher solubility of O_2 in PDMS as compared with water. Therefore, according to Henry's law, $[O_2]$ in a PDMS wall of a channel was expected to be ∼6 times higher than in an aqueous solution inside the channel. The diffusivity of O_2 in PDMS was taken to be $D_p = 1.3 \cdot 10^{-5}$ cm^2/s, as measured in our pervious study [Pol08]. We deliberately used this conservative estimate, because a higher value of the diffusivity, $3.4 \cdot 10^{-5}$ cm^2/s, as reported in the literature[MBN$^+$00], would result in improved operation of the device.

The concentration of oxygen, $[O_2]$, in the flow channels in a steady state (constant flow rate in all channels) is defined by three competing processes: lateral diffusion of $[O_2]$ from the flow channels into gas channels, vertical diffusion of $[O_2]$ from the atmosphere and from the porous PDMS chip (which is initially saturated with air) into the flow channels, and advection due to flow of the solutions (which are saturated with air, when fed into the device). To account for these processes in the device design, we used a combination of analytical estimates and simplified numerical simulations made with FemLab (Comsol, Palo Alta, CA). First, we performed a two-dimensional (2D) simulations of $[O_2]$ in a cross-section of the device ignoring the flow of liquids through the microchannels. The device was represented by a 5 mm thick and 5 mm wide PDMS chip with gas-impermeable lower boundary, corresponding to the cover glass at the bottom of the device, and with $[O_2]$ = 21% at the top and on the sides. Two gas channels ventilated with N_2 at the bottom of the device were represented by two rectangular protrusions with areas identical to the gas channel cross-sections and with $[O_2] = 0$ at their boundaries (Fig. 4.9). Because the simulation software did not have an option to account for the 6-fold jump in $[O_2]$ at the boundaries of the flow channels, the flow channel between the gas channels was represented by a rectangular region at the bottom between the gas channels with material properties identical to those of PDMS.

As a representative $[O_2]$ in the flow channel, we took its value in the middle

between the gas channels at 40 μm from the bottom, corresponding to the longitudinal axis of symmetry of the flow channel. Simulations of steady-state distributions of [O_2] indicated that, as expected, low values of [O_2] in the flow channel are achieved when the gas channels are wide and deep and when the distance between them is small. Based on results of the simulations, we chose to use 160 μm deep and 200 μm wide gas channels with 240 μm spacing between them and a 40 μm wide flow channel. With a 100 μm distance between the gas and flow channels, this configuration made it possible to use a relatively simple and robust fabrication procedure with easy alignment between the 80 μm and 160 μm tall patterns on the master mold. In addition, the 100 μm distance between the channels ensured reliable reversible bonding of the PDMS chips to cover glasses. The steady-state simulation of [O_2] distribution predicted a [O_2] of $\sim$0.3% in the flow channel, a 70-times reduction compared with a solution saturated with air. A more refined simulation, taking into account the fact that the gas channels in the device are folded into serpentine lines with a considerable footprint, (Fig. 4.5b) predicted an [O_2] of $<$0.2% (Fig. 4.1c, Fig. 4.9) corresponding to $>$100-times reduction compared with an air-saturated aqueous solution.

Because of relatively large thickness of the chip and relatively low diffusivity of O_2 in PDMS, the steady-state distribution shown in Fig. 4.9 would require considerable time to reach. To simulate transition to the steady state we performed a time dependent simulation of [O_2] in the same computational domain in Fig. 4.9, with the same boundary conditions and with [O_2] = 21% everywhere in the beginning, corresponding to a PDMS chip saturated with air. The simulation predicted that [O_2] in the flow channel is reduced to $<$0.25% within 10 min from the start of the flow of N_2 through the gas channels. This result of the simulation suggested that to achieve low levels of [O_2] in the flow channels, the PDMS chip needs to be first deoxygenated by ventilating the gas channels with N_2 for $>$10 min. (We note that the PDMS deoxygenation time is 2.7 times lower if the diffusivity of [O_2] is $3.4 \cdot 10^{-5}$ cm^2/s as reported in the literature.[MBN$^+$00])

To evaluate the effect of advection of O_2 by flow of solutions through the flow channels, we considered one-dimensional horizontal diffusion across the channels. When new boundary conditions are imposed on the two side walls of a flow channel with the width w_{ch} = 40 μm (corresponding to a stream of aerated solution reaching the region,

where the flow channel is flanked by two gas channels; (Fig. 4.1a), $[O_2]$ in the flow channel is homogenized within time $\tau_{ch} = w_{ch}^2/(8D_w) \approx 0.1$ s. If $[O_2]$ in the flow channel can be considered as uniform, the deoxygenation of the solution in the flow channel by diffusion through its two PDMS walls, each with the thickness $d = 100$ μm, towards the two gas channels has the dynamics of an exponent decaying with a characteristic time $t_{wall} = w_{ch}d/(2 \cdot 6 \cdot D_p) \approx 0.25$ s, where the factors of 2 and 6 are due to two side walls and 6-times difference in $[O_2]$ in absolute units between the solution in the channel and the PDMS wall. These estimates indicate that the time-limiting step in the solution deoxygenation is the diffusion of O_2 through the channel walls rather than homogenization of $[O_2]$ inside the flow channel. Therefore, the time required for a ~100-fold reduction of $[O_2]$ from 21% in the solution fed to the device to the limiting value of 0.2%, as predicted by the steady-state 2D simulation (Fig. 4.9), can be estimated as $\tau_{deox} = \tau_{wall} \ln(100) \approx 1.2$ s.

Hence, for complete deoxygenation of the solution, the length of the segment of the flow channel where it is flanked by gas channel, L, should be $L > \tau_{deox}\bar{\nu}$, where $\bar{\nu}$ is the mean velocity of the solution flow. For the two sheath buffer flow channels of the microfluidic device (Fig. 4.1a, Fig. 4.5a,c), the length of the deoxygenation segments was $l = 27$ mm, allowing for a maximal value of $\bar{\nu}$ of ~22 mm/s. The actual value of $\bar{\nu}$ in the buffer channels was normally ~2.5 mm/s (corresponding to flow velocities of 1 mm/s through the confocal volume at the measurement point in the 300 μm wide test region). Therefore, by the point of merging with the sample flow at the 4-channel junction, $[O_2]$ in the buffer channels was expected to reach a steady-state value defined by the diffusion through PDMS and independent of the flow of the buffer. The length of the deoxygenation segment of the channel with the sample solution was 3.5 mm (Fig. 4.5a), and because of >10 times lower value of $\bar{\nu}$ in this channel, the deoxygenation in the sample channel was always more thorough than in the sheath buffer channels. The measurement point was located in the middle of the 300 μm wide test channel, for which the distance between the gas channels was 500 μm. A steady-state 2D simulation for such channel layout predicted $[O_2] = 1.1\%$. Nevertheless, the distance between the exit of the 40 μm wide mixing channel and the measurement point was only 150 μm, corresponding to a passage time $t_{pas} = 90$ ms for the experimental flow velocity, as obtained from 3D flow simulations with FemLab at

1 mm/s velocity in the confocal volume. This passage time was substantially shorter than the O_2 diffusion time along the vertical direction of the channel (the direction of flow of O_2 from the PDMS chip) estimated as $\tau_{vert} = h^2/(8D_w) \approx 400$ ms. Therefore, $[O_2]$ in the confocal volume at the measurement point was expected to be $0.2\% + (1.1\% - 0.2\%)[1 - \exp(t_{pas}/\tau_{vert})] \approx 0.4\%$, twice higher than in the 40 μm channels, but $\sim$50 time lower than in an air-saturated solution.

Microfluidic setup: flow control and robustness of operation. The solutions fed to the inlets and drawn off from the outlet were kept in modified 500 μL eppendorf tubes. The tubes were sealed with PDMS plugs, with two small holes punched in each plug using a gauge 20 luer stub. To connect the solution in a tube to an inlet (or outlet), a segment of #30 AWG Thin Wall PTFE tubing (Cole Parmer Instrument Company; Vernon Hills, Illinois) was pushed through one of the holes to a position close to the bottom of the tube, and the other end of the segment was inserted into the inlet (or outlet). A luer stub was inserted into another hole in the plug, making it possible to drive the flow through the device by pressurizing the air in tubes connected to the inlets. The small eppendorf tubes and the narrow PTFE tubing (inner diameter of 0.25 mm; internal volume of 1 μL per 20 mm length) made it possible to perform experiments with small amounts of sample and buffers and to use the sample and buffers down to the last $\sim$20 μL. The solutions in the eppendorf tubes were centrifuged prior to use to prevent occasional contamination particles and debris from entering the devices. In addition, the solutions could easily be examined for bubbles.

The pressure of compressed air supplied to the eppendorf tubes was controlled with a resolution of $\sim$10 Pa using two pressure regulators (#8286 by Porter Instruments, Hatfield, Pennsylvania, USA 0 - 2.5 psi) and measured with an accuracy of $\sim$20 Pa with an electronic gauge (Heise, Stratford, CT). For all three inlets, nearly the entire pressure drop between the inlet and outlet occurred upstream of the 4-channel junction, where the sample and sheath streams merged. Therefore, the volumetric flow rates of the sample and buffer were proportional to pressures at the respective inlets. The hydrodynamic resistance of the channel line connecting the sample inlet with the 4-channel crossing was $\sim$1.5 times higher than the equivalent resistance of the lines between the buffer inlets and the crossings.

Therefore, to obtain a narrow sample stream for rapid buffer exchange, the sample inlet pressure had to be set substantially lower than the buffer inlet pressure. In the experiments described in the paper, the buffer inlets were both pressurized at 4 kPa and the sample inlet was pressurized at 0.5 kPa with respect to the outlet.

Flow velocities in various channels were measured by analyzing streak lines produced by 2 μm fluorescent beads (Bangs Laboratories, Fishers, IN). The extent of the longest streak line divided by the exposure time was taken as the maximum velocity in the channel, and the values of the mean flow velocity, $\bar{\nu}$, and volumetric flow rate, Q , were calculated based on the channel cross-section using the equations for developed laminar flow in rectangular channels. The values of Q were 0.36 μL/min for each of the buffer inlets (a total buffer flow of 0.72 μL/min) and 0.052 μL/min for the sample inlet, corresponding to a sample stream width of 1.8 μm in the 40 μm wide mixing channel. In the 300 μm wide measurement channel, the sample stream width was $\sim$20 μm, making it easy to align the confocal volume with the stream. The flow velocity at the location of the confocal volume in the measurement region was measured at 0.9 mm/s with an uncertainty of $\sim$5%.

Because of the large ratio of the volumetric flow rate of the buffer to that of the sample, the flow velocity through the confocal volume was nearly entirely defined by the pressure at the buffer inlets (proportional to it) and almost independent on the sample inlet pressure. Given the 10 Pa sensitivity of the pressure regulator, the flow velocity and the passage time through the confocal volume were adjustable with $\sim$0.25% precision. The adjustment of the flow velocity could be used in combination with tuning of the FRET microscopy system for optimal sample interrogation. A change in the buffer inlet pressure by, say, a factor of 1.5 would change the flow velocity by about the same factor, thus substantially modifying the conditions for optical interrogation of the sample. The 1.5-fold pressure variation would also change the width of the sample stream and the time available for buffer exchange in the mixing channel. However numerical simulations (not shown; cf. Fig. 4.6, 4.7) indicated that the concentration of the denaturant at the measurement point would only change by $\sim$2% (with 100% being its original concentration), which would likely have little effect on the protein conformation. Furthermore, because of the excessive time available for deoxygenation upstream of the 4-channel junction and relatively small ($\sim$0.2%)

increase in $[O_2]$ on the way from the mixing channel to the measurement point, the 1.5-fold change in the buffer inlet pressure would only cause ∼0.1% change in $[O_2]$ in the confocal volume and would likely have no measurable effect on the FRET signal.

The sample inlet pressure controlled the width of the sample stream and almost did not affect the flow velocity. Therefore, the sample stream width was adjustable with ∼2% precision (10 Pa in pressure), and a 1.5-fold variation in the sample inlet pressure would cause a nearly proportional variation of the sample stream width, leading to <3% change in the concentration of the denaturant at the measurement point, without any other changes in the setup operation. According to numerical simulations (not shown), the denaturant concentration at the measurement point could be reduced by ∼96% (with the sample stream width at a sufficiently large value of 8 μm) by reducing the sample inlet pressure to 0.25 kPa. These arguments show that the setup can be accurately tuned for best performance and, at the same time, its basic operation does not require fine adjustment of inlet pressures, changing relatively little even when the inlet pressures change as much as 1.5-fold.

The relatively short transit time of the sample solution between the buffer exchange and the measurement point (∼100 ms for the experiments reported in this work) suggest that the setup can be used for protein folding kinetics studies on a 100 ms scale. Moreover, as argued above, the deoxygenation and in-situ mixing of ROXS are expected to be nearly complete up to buffer flow velocities ∼5 times higher than used in the current experiments resulting in a ∼25 ms transit time, potentially making it possible to perform experiments as early as 25 ms after the initiation of the buffer exchange (Fig. 4.8b). The flow velocity at the mid-plane of the channel along the trajectory of the sample stream is nearly constant in the 300 μm wide channel downstream of the measurement point (Fig. 4.2). Therefore, the coordinate along the channel is linearly converted into time from the moment of the buffer exchange, and the conformations of protein molecules in the sample solution at times >25 ms from the buffer exchange can be inferred from FRET measurements at corresponding positions along the channel. Given the length of the channel (2.5 mm), the flow velocity (4.5 mm/s, ∼5 times above the velocity in the reported experiments), and the time of vertical diffusion of protein molecules in the channel (∼2 s), the accessible times can be as large as 500 ms.

We preliminarily tested the device with a buffer inlet pressure of 20 kPa and sample inlet pressure of 0.8 kPa, the settings producing 5 times higher flow velocity and 5 times shorter transit time with nearly the same level of buffer exchange as in the experiments reported in the paper ($\sim$0.6 μm and $\sim$6 μm sample stream widths in the mixing channel and measurement point, respectively). With a solution of FITC fed to the sample inlet and the flow visualized under epi-fluorescence illumination, we observed a steady and stable pattern of 2D-flow focusing. We note, that the burst duration and thus the number of photons collected per single molecule is dependent on various parameters such as flow speed, excitation power, dye properties and size of the confocal pinhole and might need to be optimized if one parameter is changed.

Fabrication of microfluidic device. The microfluidic device consisted of a PDMS chip sealed by a #1 cover glass. The chip was cast out of PDMS (10:1 mixture of parts A and B of Sylgard 184 by Dow Corning, Midland, MI) using a master mold fabricated in a two-step photolithography process described in detail elsewhere. Briefly, a 5 in. silicon wafer was spin-coated with a 80 μm layer of a UV-curable epoxy (SU8-2050 by Microchem), exposed to UV-light through a photomask (transparency photoplotted at 25,000 dpi), baked to cure the UV-treated PDMS, spin-coated with another 80 μm layer of the epoxy, exposed through a second photomask, baked, and developed. The pattern of cured SU8 on the completed master mold had features of two heights, 80 μm (for flow channels) and 160 μm tall (for gas channels). To make the PDMS chip, a 5 mm thick layer of PDMS pre-polymer was poured onto the mold and then baked in an 80 °C oven for $\sim$40 min to cure PDMS. The PDMS was then peeled off the wafer, trimmed to the size for individual chips, and holes were punched in the chips to produce inlet and outlet ports. The PDMS chips were reversibly bonded to cover glasses by overnight baking at 80 °C.

Measurements of oxygen concentration in microchannels. The concentration of oxygen, $[O_2]$, in the flow channels was measured using a solution of an oxygen-sensitive fluorescent dye ruthenium tris(2,2'-dipyridyl) dichloride hexahydrate (RTDP, 0.5 g/l in PBS, Ambion, Austin, TX). The fluorescence of RTDP is quenched by oxygen, with the intensity of fluorescence decreasing as $[O_2]$ increases according to the Stern-Volmer equation, $I_0/I = 1 + K_q[O_2]$, where I_0 is the intensity of fluorescence without oxygen, I is the

intensity of fluorescence at the give $[O_2]$, and K_q is a quenching constant. It is convenient to measure $[O_2]$ as percentage of its value in water saturated with pure oxygen at 1 atm, so $[O_2]$ in water saturated with air is 20.9%. The value of K_q corresponding to this definition of $[O_2]$ is dimensionless, but depends on the temperature and ionic content of the solution, and therefore has to be determined experimentally.

The measurements of RTDP fluorescence were performed on a Nikon TE300 inverted fluorescence microscope (Nikon, Melville, NY). The source of fluorescence illumination was a blue LED (Royal Blue Luxeon V by Lumileds, San Jose, CA; 700 mW with central wavelength 455 nm) mounted on a cooling fan and inserted into a modified Nikon lamp house. The LED was powered by a regulated DC supply with and provided stable illumination with <0.5% variation of intensity over several hours. Images were taken with an Olympus 20X/0.7 WI objective and a Coolsnap HQ camera (Photometrics, California). We first used the microscope to evaluate K_q by measuring the intensity of fluorescence of the RTDP solution, I, in a 100 μm deep 300 μm wide microchannel, when the solution was saturated with N_2, air, and O_2 using a technique described elsewhere [Pol08]. Based on the three fluorescence intensities, I_0, $I(20.9\%)$, and $I(100\%)$, respectively, K_q was estimated as 2.25 (per 100%) with an uncertainly of ∼0.5%. After that, all three inlets of the microfluidic device were fed with the RTDP solutions by applying a pressure of 4 kPa to the buffer inlets and a pressure of 1 kPa to the sample inlet, and creating flow conditions nearly identical to the smFRET experiments reported in the paper. The gas channels were fed with either air or N_2, both at a pressure of 1 psi, the same as in the smFRET experiments. To allow time for equilibration of the gas content in the PDMS chip, fluorescence measurements were started >5 min after the gas supplied to the gas channels was switched. The value of I_0 was calculated using the measured value of and the intensity of RTDP fluorescence when the gas channels were ventilated with air, I_{air}, under the assumption that $[O_2]$ in the flow channels in this case was 20.9%: $I_0 = I_{air}(1 + K_q 0.209)$. The value of I_0 calculated in this fashion was then used together with the value of RTDP fluorescence at the point of FRET measurements when the gas channels were ventilated with nitrogen, I_{N_2}, to estimate $[O_2]$ at the FRET measurement point $[O_2] = (I_0/I_{N_2} - 1)/K_q$. In this case the result was indistinguishable from 0 within the 0.5% measurement uncertainty, which was consistent

with the estimate $[O_2]$ ~0.4% obtained from the numerical simulations.

Sample preparation. Two complementary strands of DNA were labeled using standard succinamide chemistry as described in the manufactures kit (Invitrogen, Carlsbad, CA and GE Healthcare, Piscataway, NJ)). Alexa488 was ligated using an aminomodifier at T9 and Cy5 was attached to the 3' terminus of the complementary strand with the following sequences (IDT, San Diego, USA), spacing the two dyes 9 bases apart in agreement with the observed FRET efficiency (Fig. 4.2):

5'-CTC TTC AGT(A488) TCA CAG TCC ATC CTA TCA GC-3'

5'-GCT GAT AGG ATG GAC TGT GAA CTG AAG AG-3' Cy5

Alexa488 (donor) was attached by reaction of its N-hydroxysuccinimidyl ester with an amino group introduced at T9 (via a C6 Amino Modifier dT), and Cy5 (acceptor) was attached to the 3' terminus of the complementary strand by reaction of its N-hydroxysuccinimidyl ester with a 3'-amino group. Labeled DNA strands were purified by polyacrylamide gel electrophoresis. The duplex construct was prepared by annealing the purified complementary labeled DNA strands prior to use in 2xPBS buffer by heating to 94 °C followed by gradual cooling (1°/s) to room temperature.

A cysteine free variant of T4Lysozyme containing a C-terminal his tagged was genetically modified to contain a Cys residue at position 109 and to encode for the non-natural amino acid p-acetylphenylalanine at position 38. The protein was expressed and the two sites were site specifically labeled as previously reported [BLSD08]. Alexa488-hydroxylamine (Invitrogen) was used to label position 38 and Cy5-maleimide (GE Healthcare, Piscataway, NJ) was reacted with the cysteine residue at position 109. Experiments were performed as described in the text either in 2xPBS or 2xPBS with 4M guanidinium chloride (GdmCL). The individual components of ROXS, AA and MV, were used as previously described at 1mM each [VKS$^+$08].

Single-Molecule Spectroscopy. Single molecule FRET experiments were performed as previously described [BLSD08]. Briefly, laser light at 488 nm from an argon ion laser (Melles Griot, Carlsbad, CA) was coupled into a Zeiss Axiovert 200 microscope (Zeiss, Thornwood, NY) by a single mode fiber (Pointsource, Hamble, UK) and focused into the sample using a Zeiss C-Apochromat 40x, 1.2 NA, after passing through a $\lambda/4$ plate.

The emitted light was separated from the excitation light by using a dichroic beam splitter (Q495LP, Chroma Tech. Corp., Rockingham, VT), and further spatially filtered by focusing on a 75 μm pinhole. The light was spectrally split into Donor and Acceptor channels by using another dichroic beam splitter (DC560, Chroma). After passing through bandpass filters (Donor channel, 525/50 (Chroma) and acceptor channel, 700/70 (Chroma)), the light was focused onto and detected by avalanche photon counting modules (SPCM-AQR-14, Perkin-Elmer Optoelectronics, Fremont, CA). An SPC630 computer card (Becker&Hickl, Berlin, Germany) operating in the FIFO TAG mode was used to record the arrival times of individual photons. Individual bursts were identified by using a previously described burst search algorithm[EBB$^+$01]. FRET histogram analysis was carried out on bursts containing more than 40 photon counts using IgorPro (Wavemetrics, Lake Oswego, OR). FRET efficiencies were computed as proximity factors $E_{FRET} = \frac{I_A}{I_A+I_D}$, with I_A and I_D being the detected photon counts in the Donor (D) and Acceptor (A) channels corrected for a bleed through of 2% of fluorescence from the D into the A channel. Gaussian fits of the resulting histograms were calculated by using IgorPro, and the peak positions and widths (σ) were obtained from the fitting parameters. The photon signals from the Donor and Acceptor channels were also simultaneously fed into a Hardware correlator (ALV-6010/160; ALV-GmbH, Langen, Germany) to compute the fluorescence cross correlation function between the two channels. A fast decay component due to blinking from transitions to and from the dark triplet state is clearly visible under some conditions (Fig. 4.4).

ACKNOWLEDGEMENTS

This work was supported by grants PHY0750049 and OCE-0428900 from the National Science Foundation (A.A.D., V.V., and A.G.), GM073104 from the National Institute of General Medical Science, NIH (A.A.D.), NIH GM62159 (P.G.S.) the Alexander von Humboldt Foundation (E.A.L.) and La Jolla Interface In Science program (Y.G).

Chapter 4.1 is in preparation for publication in Microfluidic device for single-molecule fluorescence experiments with high photostability. Lemke, Edward*; Gambin, Yann*; Vandelinder, Virginia*; Brustad, Eric; Schultz, Peter; Groisman, Alex; Deniz, Ashok. Dissertation author was one of the principal investigators of this paper.

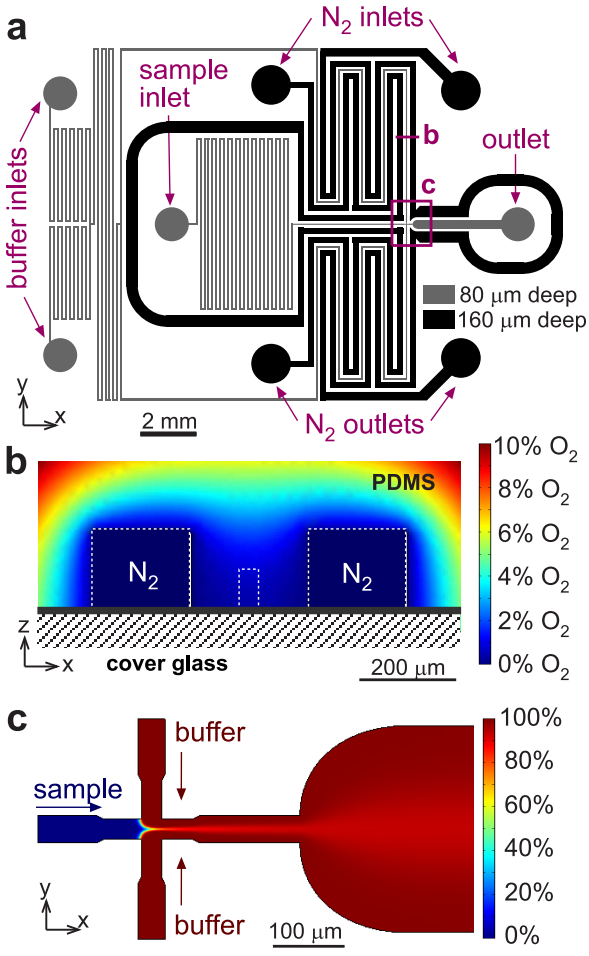

Figure 4.1: (a) Schematic of the microfluidic device consisting of a 80 μm deep network of channels for sample solution and buffers (grey), and 160 μm deep channels for nitrogen (black). (b) Cross sectional view of a 40 μm wide flow channel flanked by two nitrogen channels with color-coded concentration of oxygen in PDMS from a numerical simulation (see Methods). (c) 2D focusing and interrogation channels with color-coded concentration of denaturant from a numerical simulation.

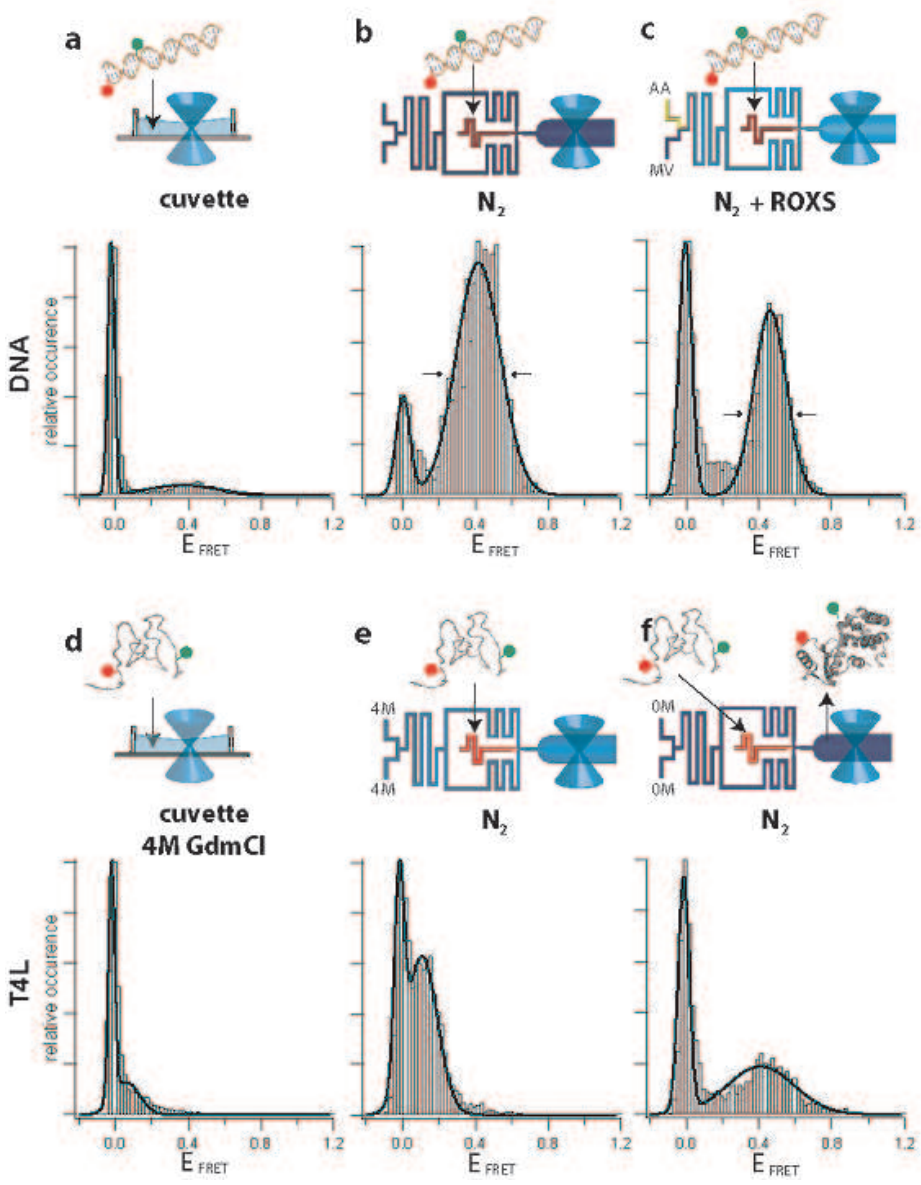

Figure 4.2: Histograms of smFRET efficiency, E_{FRET}. (a-c) Dual labeled DNA: (a) in a cuvette open to air, (b) in the microfluidic device with deoxygenation, and (c) in the microfluidic device with deoxygenation and addition of ROXS. (d-f) T4L protein: (d) with denaturant in a cuvette; (e) in the microfluidic device with deoxygenation and with denaturant; (f) in the microfluidic device with deoxygenation after denaturant is removed by buffer exchange.

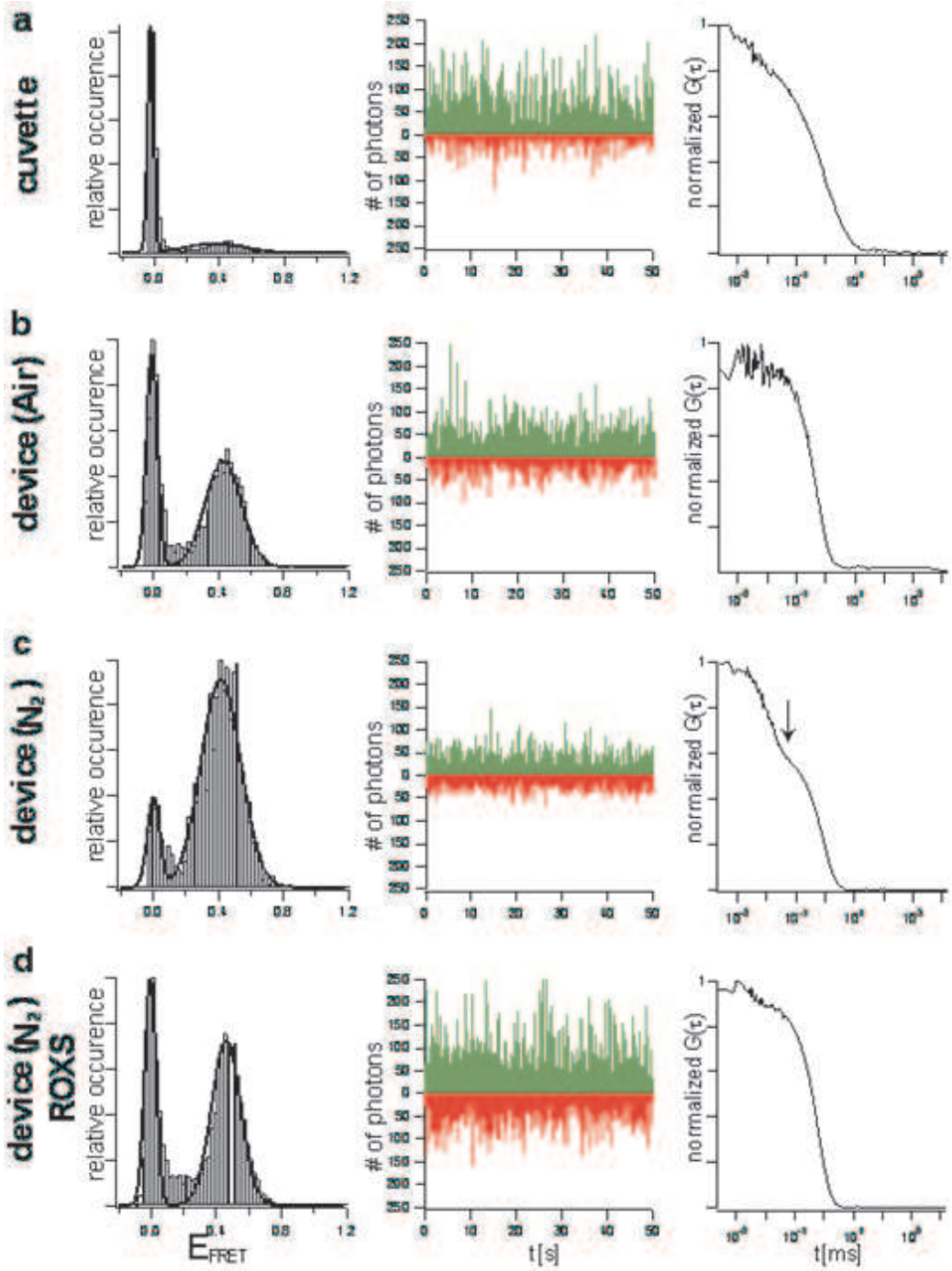

Figure 4.3: Shown is the experimental data for FRET measurements of DNA in a cuvette (a) in the device in the presence of ambient air (b), in the device using deoxygenation with N_2 (c) and in the device with N_2 and additional rapid mixing with ROXS (d).

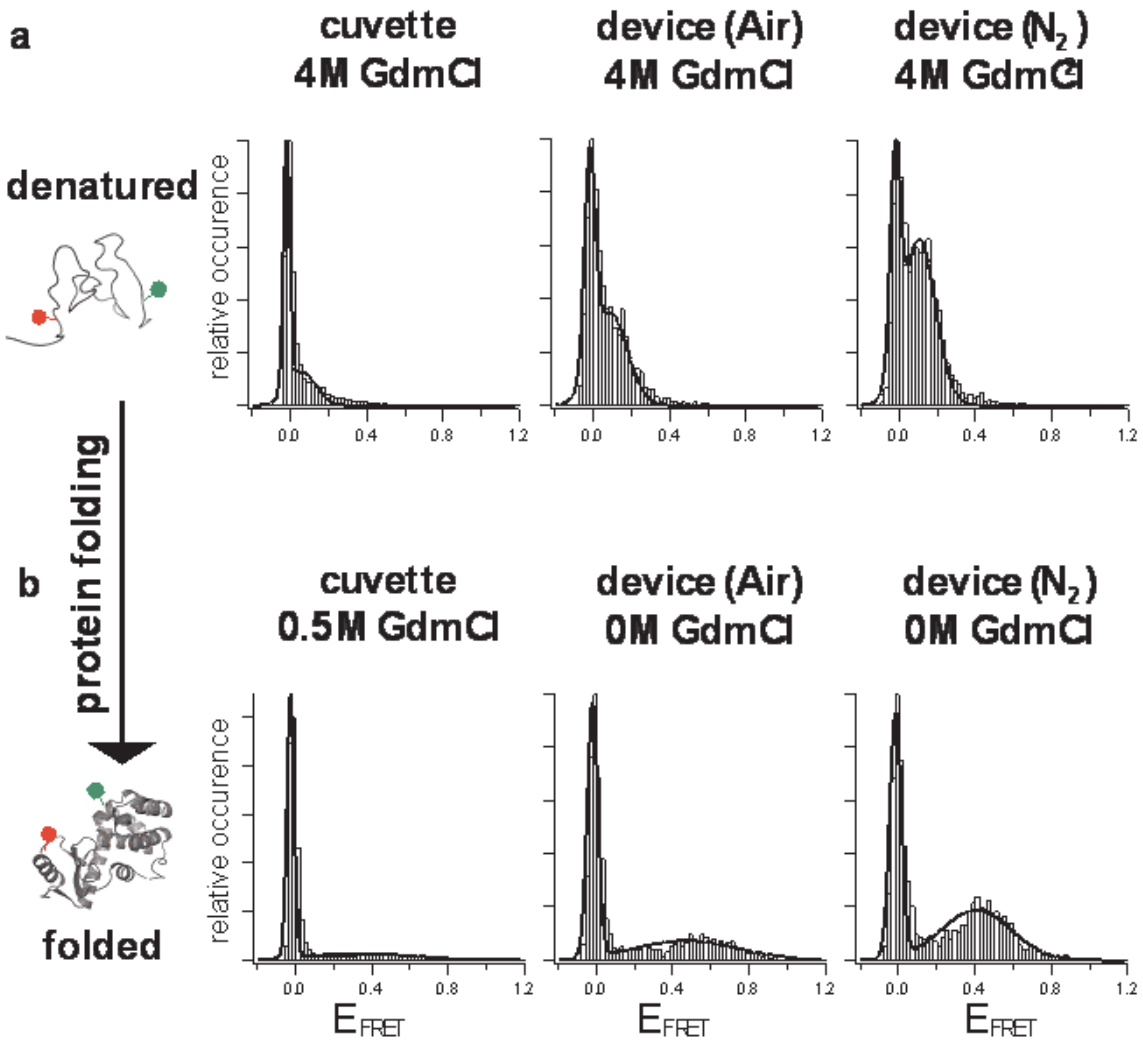

Figure 4.4: Shown is the experimental data for FRET measurements of dual labeled T4L under denaturing conditions (a) measured in a cuvette (left panel), in the device with ambient air (middle panel), and N_2 flow (right panel). Similar to the experiment performed on DNA, the beneficial effect of deoxygenation is visible by an improvement in the zero peak to FRET peak ratio. This particular example also illustrates, that deoxygenation in the device enables us to clearly identify populations that are barely separated or even indistinguishable under standard conditions. The utility of the device for protein folding studies was also demonstrated by rapidly mixing protein loaded in 4M GdmCL buffer with physiological buffer. The resulting data is shown in (b). Note that due to sticking issues under physiological conditions of Cy5 labeled T4l the cuvette experiments were performed at 0.5M GdmCl Under those conditions T4L already exists in its folded state. We emphasize that the described operation of the device circumvents sticking issues.

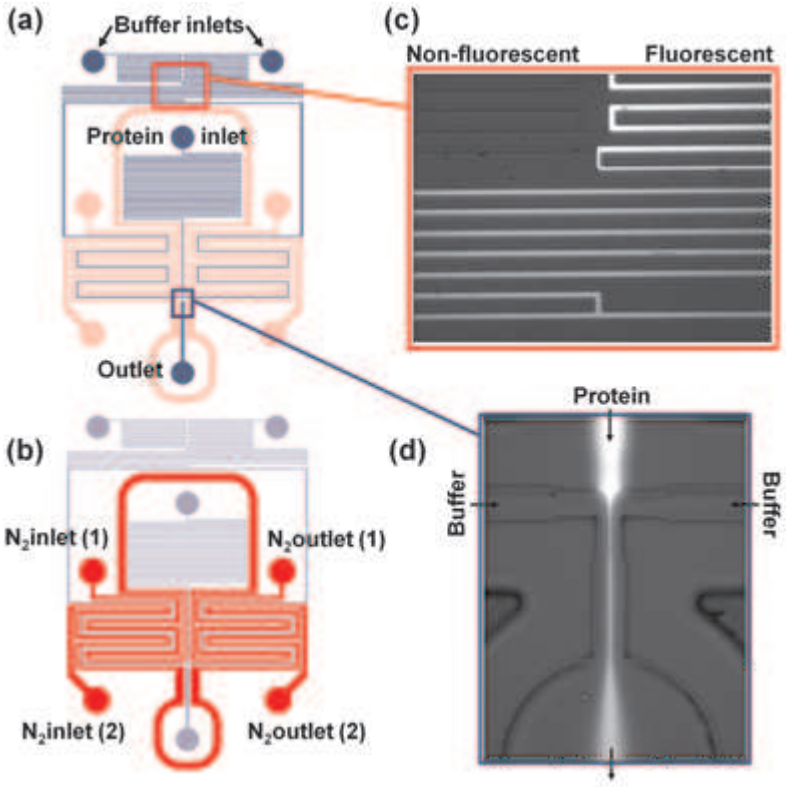

Figure 4.5: Schematics of the device showing (a) the network of flow channels and (b) the system of deeper gas channels. (c) Micrograph showing the slow mixing in the serpentine channels of 2 components (fluorescent and non-fluorescent). (d) Micrograph of the mixing region showing a stream of fluorescent molecules being squeezed by the two side inlets carrying the non fluorescent measurement buffer.

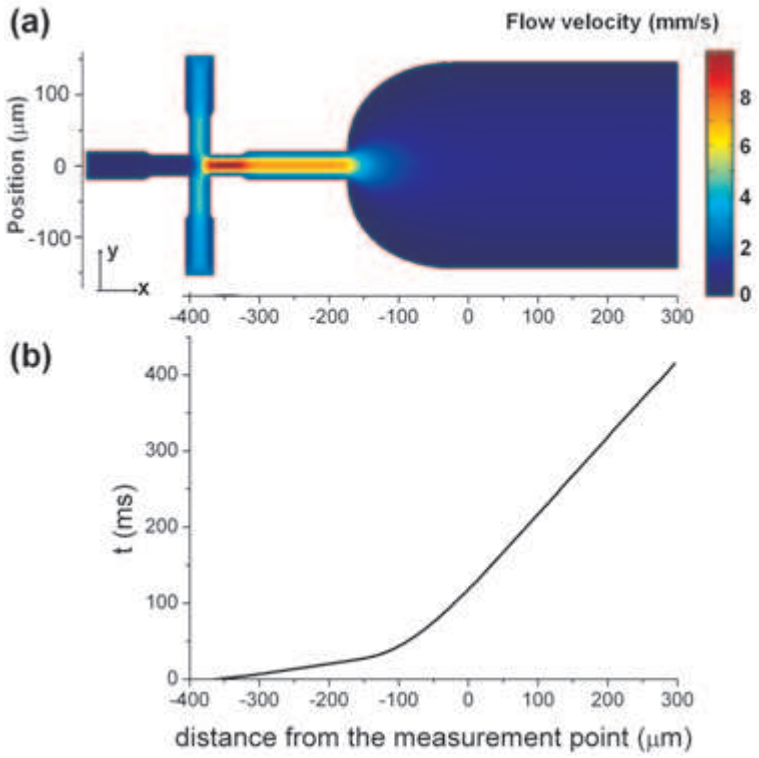

Figure 4.6: The hydrodynamics in the device were analyzed using the commercially available program FemLab. The simulations were performed to match the experimental conditions cited in the description of the microfluidic setup. a) Velocity simulations using full Navier-Stokes equations. The unit on the colorbar are in mm/s. The measurement occurs at $x = y = 0$. b) Data of time spent by the molecules in their streamline along $y = 0$ as a function of position x in the device.

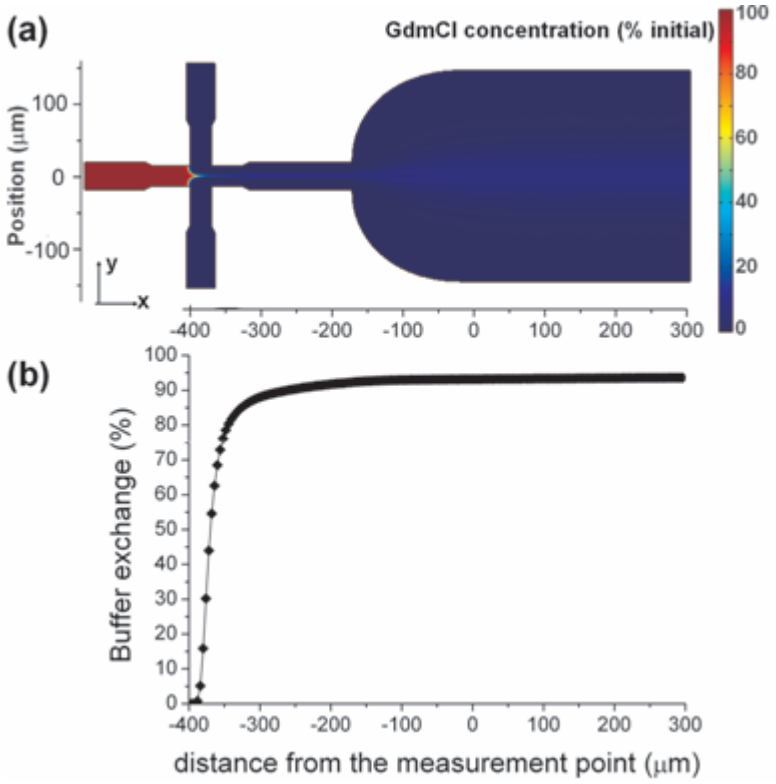

Figure 4.7: a) Results of a simulation of Guanidinium Chloride (GdmCl) removal (buffer exchange) from the protein stream. A typical value of $10 \cdot 10^{-10}$ m^2/s is used for the diffusion coefficient of GdmCl molecules. The colorbar on the right shows the percentage of initial GdmCl concentration, vs. 100% in the sample inlet and 0% in the two side buffer inlets. b) Percentage buffer exchange along the $y = 0$ streamline as a function of position in the device.

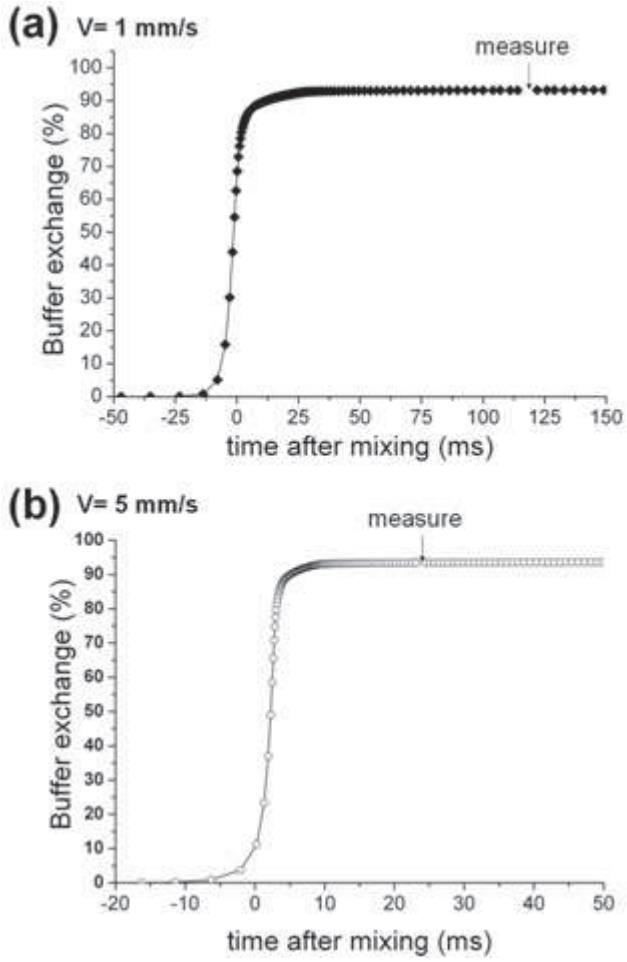

Figure 4.8: Kinetics of sample stream buffer exchange in the microfluidic device. a) Percentage of buffer exchange of the sample stream buffer with the sheath buffer (for example, to dilute GdmCl concentration in a protein folding experiment) evaluated in the middle of the sample stream as a function of time, at a flow rate of 1 mm/s, as calculated from Fig. 4.4 and 4.5) Femlab simulations showing that mixing times shorter than 25 ms can be obtained when operating the device at higher pressures. In this simulation, the flow velocity in the measurement channel is 5 mm/s instead of 1 mm/s. Due to the high signal-to-noise ratio achieved in the deoxygenation device, acceptable quality smFRET histograms are expected even with the correspondingly shorter burst durations (to be tested in future work).

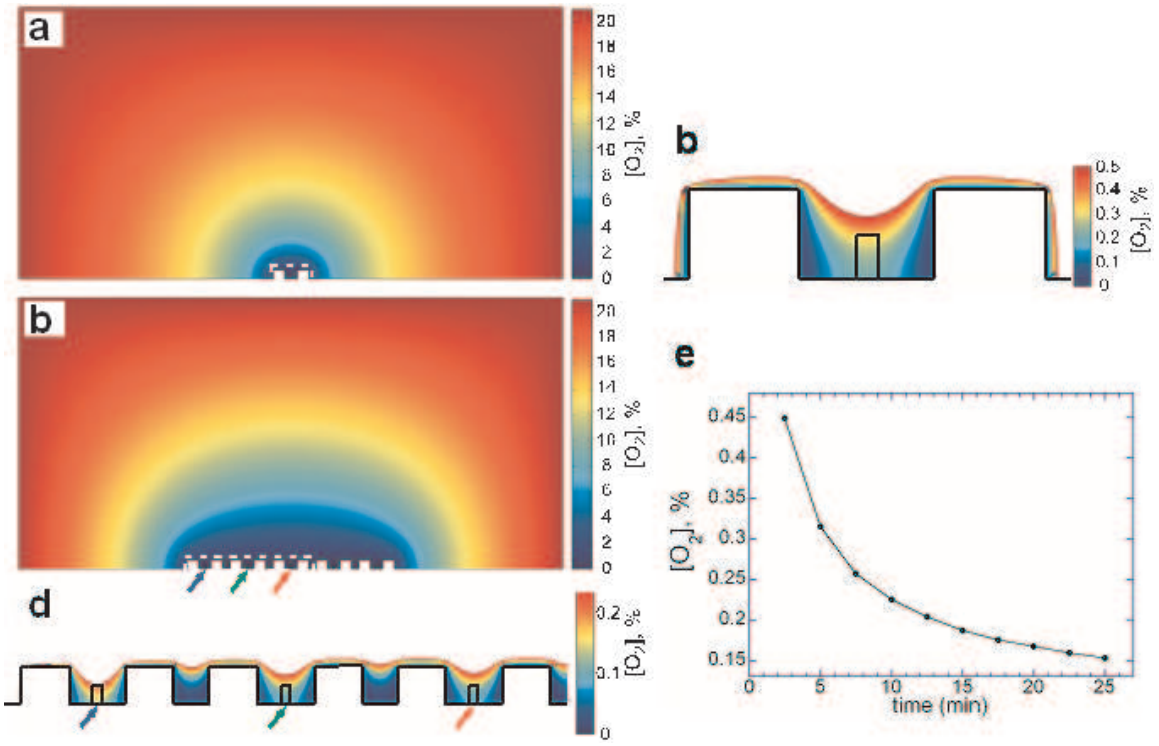

Figure 4.9: Two-dimensional (2D) numerical simulations of the distribution of oxygen concentration, $[O_2]$, in two PDMS chips. Both chips have 10x5 mm cross-sections (horizontalvertical) with gas-impermeable lower boundaries, corresponding to the cover glass at the bottom of the microfluidic device, and with $[O_2] = 21\%$ at the top and on the sides. The gas channels ventilated with N_2 are represented by 200x160 μm rectangular protrusions at the bottom (identical to the gas channel cross-sections) with $[O_2] = 0$ at their boundaries. The distributions of $[O_2]$ in the computational domains are color-coded with legends shown on the right. a) Steady-state distribution of $[O_2]$ in a chip with two gas channels separated by 240 μm. b) Magnified view of the region marked by a white dashed box in (a). $[O_2]$ is color-coded from 0 to 0.5%, and areas with $[O_2] > 0.5\%$ are blank. Black rectangle in the middle shows the location of the flow channel. At 40 μm above the bottom in the low channel $[O_2] = 0.25\%$. c) Steady-state distribution of $[O_2]$ in a chip with 5 sets of channels, as in the microfluidic device (Fig. 4.1). Each set is identical to the two gas channels with a flow channel in the middle in (a) and (b), and the distance between adjacent sets is 150 μm. d) Magnified view of the region marked by a dashed box in (c) with 3 channel sets. Black rectangles show locations of flow channels. $[O_2]$ is color-coded from 0 to 0.25%, and areas with $[O_2] > 0.25\%$ are blank. The levels of $[O_2]$ in flow channels marked by blue, green, and red arrows are 0.17%, 0.11%, and 0.10%, respectively. e) $[O_2]$ in the central flow channel (marked by red arrows in (c)and (d)) from a time dependent numerical simulation in the computational domain shown in (c). The initial condition was $[O_2] = 21\%$ everywhere.

4.2 Kinetics of single molecule protein folding

The misfolding and formation of fibrous aggregates of α-synuclein has been implicated in Parkinson's and Alzheimer's disease.[SFJ+03] Understanding the entire folding pathway from monomer to the potentially harmful aggregates could serve as a lever to unravel the physiological process of aggregate formation from monomeric species. This goal is largely obscured by the existence of multiple, possibly coexisting heterogenous species of α-synuclein, as well as a lack of technology to access fast kinetics of protein folding and conversion.

Here we combine single molecule FRET (smFRET) and microfluidic mixing to map the folding landscape of α-synuclein with unprecedented time resolution of less than 0.5 ms. We designed a novel microfluidic device in which the protein solution is accelerated to a speed of 2 m/s, the carrier medium of the proteins is exchanged by rapid diffusion in laminar sheath flow, and the new protein solution is abruptly decelerated and directed into the observation channel where conformational changes of the protein molecules are monitored with smFRET measurements as the reaction proceeds.

We find that the binding of lipid-mimetics induces rapid formation of highly helical structures through 'one-way' intermediates, as the folding sequence of α-synuclein is different from the unfolding sequence. Our microfluidic device reveals ephemeral kinetics intermediates that are undetectable in either 'bulk' kinetic experiments or single-molecule experiments using existing instrumentation. The fast buffer exchange in the device provides a general platform to explore the mechanisms of folding and amyloid formation, which is key to deciphering the molecular basis of multiple diseases.

The α-synuclein protein is a member of the growing class of intrinsically-disordered proteins (IDPs) for which the folding is not solely defined by the amino-acid sequence. Rather, these proteins are natively unfolded and will only find their functional 3D-structure upon interaction with cellular partners.[DC97, Dob03] The conformational 'search' is a complex process, potentially involving multiple binding steps that are difficult to study with ensemble averaging techniques.[BOSW95, OW04] Hence, single molecule kinetics methods hold particular promise for revealing new details of the folding pathway. In particular,

FRET microscopy is a tool of choice to observe structural changes at the single molecule level [TMLO00, Wei00] and to directly detect intermediate conformations as folding proceeds [OW04, Sch05].

In order to observe the entire process of conformational modifications in a protein, the timescale of the carrier medium exchange must be shorter than the onset time of the earliest events of the process. Rapid medium exchange can be achieved through mixing in conventional turbulent stopped flow or quench flow apparatus. Even faster medium exchange, as short as a microsecond, can be attained with laminar microfluidic sheath-flow mixers, which have an additional benefit of greatly reducing sample consumption [PQR$^+$06, HIM$^+$06]. In order to reach these short medium exchange times, laminar sheath-flow mixers are operated at flow rates in the 1 - 10 m/s range. However, smFRET measurements require a sufficient number of photons to be collected during the passage of a molecule through the sub-micron size optical interrogation volume, practically limiting the flow velocity to $\sim$1 mm/s. Therefore, adaptations of laminar sheath-flow mixers to smFRET interrogation involved substantially reducting the flow speeds, which compromised the mixing speed and limited the studies of folding kinetics to time scales longer than 100 milliseconds [LSBE03]. Modifications of these high-speed devices, such as reduction of mixer dimensions or use of micro-pipette injection, rendered their fabrication substantially more difficult without making accessible folding processes with time scales of shorter than tens of milliseconds.

In order to study folding kinetics at the single molecule level with sub-millisecond time resolution, we built a microfluidic device where the carrier medium is rapidly exchanged in a high-speed sheath flow that is abruptly slowed down to a speed compatible with smFRET (Fig. 4.10). In the medium exchange portion of the device illustrated in Fig. 4.10, the protein stream is squeezed to $\sim$200 nm layer between two buffer streams. Low-molecular molecules diffuse across this thin layer within a few microseconds, triggering protein folding or unfolding [HMJ$^+$04]. To accommodate the study of more complex systems where structural changes are triggered by binding of ligands or substrates, the device has a reaction chamber to allow slowly-diffusing reagents to reach the middle of the stream.

Immediately downstream of the reaction chamber, $>$99% of the flow is diverted into two side outlets. The flow velocity, after peaking around 2 m/s, decreases abruptly

by 3 orders of magnitude within a few μm. Thus the flow of protein sample becomes sufficiently slow for smFRET measurement only 200 ms after its carrier medium is completely exchanged (Fig. 4.11), which is two orders of magnitude earlier than previously reported in a microfluidic device.

The design of device, especially the shape of the deceleration region, was optimized in an extensive series of 3D flow simulations in order to obtain a minimal residence time along the protein trajectory while avoiding vortices. The simulations show (Fig. 4.11) that only molecules moving in the middle of the reaction chamber, both laterally and vertically, proceed to the measurement channel, while other parts of the sample stream are redirected to the side outlets. This behavior limits the dispersion in mixing time, as all the protein detected traveled where the flow is the fastest.

While passing through the reaction chamber, the protein molecules diffuse laterally, generating low-concentration tails on the sides of squeezed protein stream. By making the flow rates of the two buffer inlets slightly asymmetric, it is possible to select which portion of the protein stream enters the measurement channel, the concentrated center of the protein stream or somewhere in the low concentration tails. Thus, we can dilute the protein sample by an arbitrary factor without changing the total flow rate. The ability to continuously and rapidly tune the protein concentration from micromolar to picomolar expands the application of the device to weakly bound complexes and transient oligomers, which, upon dilution to concentrations usually required for smFRET, dissociate too quickly to be detected by previous methods [LKT$^+$03].

The general design of this microfluidic platform is suitable for various observation techniques including X-Ray, infrared, and fluorescence detection. In this work we use a home-built confocal setup for smFRET measurements. When individual labeled protein molecules pass through the small confocal volume, bursts of fluorescence from the donor and acceptor dyes are separately recorded. Photon counts are analyzed to generate histograms of FRET efficiency, which translate into structural distributions [DLB$^+$00, DML08]. By scanning the confocal detection along the measurement channel (with the distance-time conversion shown in Fig. 4.11), one can follow the evolution of intramolecular distances from 200 μs up to several seconds after mixing (see methods).

Exploring α-synuclein folding pathway.

The protein α-synuclein has been shown to interact with negatively charged lipid bilayers, and studies have demonstrated that the lipid-mimetic SDS can imitate the binding of lipids and drive the formation of alpha-helical structures. Using a combination of Circular Dichroism and smFRET under equilibrium conditions, we recently discovered that a particular concentration of SDS monomers induces the formation of a long, continuous α-helix. [FD07, Fer09] In this work, we used smFRET and the microfluidic device to investigate the folding and unfolding routes between the native unfolded (U) state and the fully-extended conformation (called F state hereafter).

In the first experiment, the stream of natively disordered a-synuclein is hydrodynamically focused between two symmetric flows containing the binding partner SDS. Immediately after mixing, we follow the evolution of FRET efficiency, E_{FRET}, between the donor (A488) and acceptor (A594) fluorescent dyes grafted on the protein. Strikingly, instead of a two-state transition, multiple folding events are observed before the final equilibrium structure is formed. The earliest single-molecule measurement, performed only 200 μs after the addition of SDS, already shows a shift of the E_{FRET} peak from 0.45 (no SDS, U-state) towards higher E_{FRET}. The interaction with negatively charged SDS molecules does not cause an expansion of the protein chain; on the contrary, the protein appears to compact within the first few milliseconds. Following this initial compaction of the protein, the shape of the FRET peak, which is centered around $E_{FRET} = 0.7$, becomes asymmetric, and after 1 ms, a stable high-E_{FRET} state is reached. We then observe a two-state conversion of this intermediate conformation to the expected final structure (F-state characterized by a low- E_{FRET} peak), occurring within about 11 ms (Fig. 4.12).

In order to study the unbinding events, a solution of protein with an SDS concentration that favors the F-state was hydrodynamically focused between streams of buffer with no SDS. After the carrier medium exchange, concentration of binding partners effectively drops and is no longer sufficient to maintain folding. The data show that the weakly-bound α-synuclein-SDS complex dissociates quickly, as the low-$_{EFRET}$ F peak present at 200 μs can no longer be detected after 1 ms. Strikingly, no proteins adopt a high-E_{FRET} conformation; the intermediate state cannot be observed in the unfolding pathway.

The data suggests the following scenario: at early folding stages, binding of SDS molecules compacts the unfolded α-synuclein and then triggers the formation of an intermediate folded state. The FRET peak of the intermediate state corresponds to the one obtained at the SDS concentration where micelles form and α-synuclein is known to adopt a helix-kink-helix structure. The 'broken helix' conformation was previously believed to be a mere artifact of the highly-curved SDS micelles, and the elongated helix was though to be the only relevant state stabilized by the membrane interface. Our data show that the kinked structure is an essential kinetic step in the folding process, and that discrete binding events can trigger the dramatic conformational transition to the fully extended helix (low-E_{FRET} folded state).

More importantly, the folding and unfolding routes differ radically. When the binding partners are rapidly removed from the fully-folded state, the intermediate state and the SDS-bound compacted states are not populated on the way to the unfolded state. The apparent non-reversibility of the folding pathway can be explained if we consider that all interactions 'sites' have similar affinities in the fully folded state. In that case, unbinding of the stabilizing partners would be random and result in the observed fast collapse, directly to the unstructured state. This opens an intriguing possibility: the fact that the final state is not directly formed during folding suggests that 'binding sites' do not have the same accessibility within the unfolded α-synuclein. It may be possible that, even if the protein does not have a defined structure under native conditions, its spatial conformation is not fully random and parts of the protein could be engaged in intra-chain interactions and so remain concealed to binding partners. Only the formation of the intermediate folded state would expose more interaction sites, and the interaction with further binding of partners would induce the final conformational switch.

Overall, the single molecule microfluidic mixer enabled us to explore in detail the folding of proteins under non equilibrium conditions, revealing kinetic intermediates and transient conformations that would remain hidden if the existing techniques were used. The ability to tune the concentration of proteins as well as folding conditions makes it a promising tool to observe the coupling between structural changes and oligomer formation on the aggregation pathway of synucleins and other amyloidogenic proteins.

METHODS

Microfluidic Device Design. The layout of the microfluidic device is shown in Fig. 4.10. The dimensions and layout of the flow channels were chosen to provide optimized conditions for single molecule FRET microscopy in the measurement region and fast and efficient buffer exchange in a laminar sheath flow immediately upstream of the measurement region.

A channel depth of 15 μm was selected as a compromise between avoiding unwanted inertial effects, for which channels with a small diameter are advantageous; and overcomplicating the fabrication with small features. In preliminary experiments, we found that the autofluorescence of the glass coverslip that seals the PDMS chip substantially raises the background noise in the smFRET measurements, which are performed at half channel depth (at 7.5 μm from the coverslip). To reduce this autofluorescence background, we cover the coverslip with a 50 μm layer of PDMS. The autofluorescence of PDMS at the wavelength used in the experiments was found to be 10 times less than that of glass.

The width of the measurement channel was chosen at 30 μm, so the beams focused and collected by the high-NA objective used in the experiments (40x, NA = 1.2, water immersion) would not be distorted by passing through the PDMS side walls of the channel, which had a refractive index of $\sim$1.41 as compared to $\sim$1.33 for water.

Liquids used in the experiments were aqueous solutions with viscosities close to the viscosity of water, 10^{-3} Pas. Therefore, the Reynolds number corresponding to a 0.5 m/s flow in a 10 μm channel was $Re \approx 5$. At this moderate value of Re, the flow is generally laminar, but inertial effects are still significant in regions where the flow velocity, $\vec{v}$, rapidly changes in space [large value of $(\vec{v}\cdot\bar{\nabla})\vec{v}$]. Therefore, the width of the focused protein stream sandwiched laterally by buffer streams cannot be calculated simply from the ratio of the volumetric flow rates; instead, finite element simulations must be performed to correctly predict the width and shape of the protein stream. We analyzed the hydrodynamics in the device using the commercially available program FEMLAB. Velocity simulations were performed with full non-linear Navier-Stokes equation, and distributions of concentration were numerically calculated using the classic diffusion and convection equation. The shape of the channels in the device was iteratively optimized based on the simulation results to

achieve stable flow.

The microfluidic device has a number of features that make experiments more facile. Large particles, such as specks of dust, going through the confocal volume can destroy an avalanche photo detector (APD). To stop such particles, the buffer channels have arrays of microfabricated pillars 10 μm dia spaced 5 μm apart serving as filters. The filters also prevent clogging of the contractions of the buffer channels that are only 8 μm wide. In addition, the device has location markers along the measurement channel, which enable the operator to perform measurements with good reproducibility.

Fabrication. The device is a poly(dimethylsiloxane) (PDMS; Sylgard 184 by Dow Corning, Midland, MI) cast of a UV-lithography microfabricated master mold. To make the master mold, a 15 μm layer of UV-curable epoxy SU8 2015 (MicroChem, Newton, MA) was spin-coated onto a 5" silicon wafer, exposed to UV-light through a specially designed chrome photomask (Photo Sciences, Inc., Torrance, CA; 0.5 μm resolution), and cured on a hot plate. The resulting developed wafer was silanized by exposure to a vapor of chlorotrimethylsilane (Sigma-Aldrich, St. Louis, MO) at room temperature for 90 s to facilitate release of the PDMS replicas. Next, PDMS pre-polymer (10:1 mixture of the base and curing agent) was poured onto the master mold and baked at 80 °C for 1 hr. The PDMS casts ($\sim$5 mm thick) were peeled off the master mold and cut into individual chips, which were trimmed to size and punched with luer stubs to make inlet and outlet holes. Glass coverslips with layers of PDMS on them were made by spin-coating a 50 μm thick layer of uncured PDMS on #1 microscope cover glasses and baking at 80 °C for 1 hr. The PDMS chips were then reversibly bonded to the PDMS-coated cover glasses by overnight baking in an 80 °C oven. The PDMS-PDMS bond was able to withstand over 7 psi pressure without delamination. (Higher pressures were not tested, since 7 psi was more than sufficient for the experiments reported in the paper). A single master mold was used to for making all the microfluidic chips used in the study. It produced 4 copies of the chip in one cast. For repeated use, PDMS chips were separated from coverslips, cleaned by boiling in HCl for 1 hr, and then bonded to new PDMS coated cover glasses.

Experimental Set-up. The device has 3 inlets consisting of 2 buffer inlets and 1 protein inlet, and 3 outlets consisting of the measurement channel outlet and 2 buffer

outlets. All fluids connected to inlets and outlets were kept in 500 μL eppendorf tubes. The tubes were sealed with PDMS plugs, with two small holes punched in each. To feed the solution in a tube to an inlet (or draw it off from an outlet), a segment of #30 AWG Thin Wall PTFE tubing (Cole Parmer Instrument Company; Vernon Hills, Illinois) was pushed through one of the holes to a position close to the bottom of the tube, and the other end of the segment was inserted into the inlet (or outlet). A luer stub was inserted into another hole in the plug, making it possible to drive the flow through the device by pressurizing the air in tubes connected to the inlets. The small eppendorf tubes and the narrow PTFE tubing (inner diameter of 0.25 mm; internal volume of 1 μL per 20 mm length) made it possible to perform experiments with small amounts of sample and buffers and to use the sample and buffers up to the last $\sim$20 μL. The solutions in the eppendorf tubes were centrifuged prior to use to prevent occasional contamination particles and debris from entering the PTFE tubing. In addition, the solutions could easily be examined for bubbles.

Flow through the device was driven with a combination of air and hydrostatic pressure. The level of liquids fed to the buffer inlets was 15 inches above the level of liquids in the tubes connected to the outlets. In addition, in the FRET experiments, the air of the tubes connected to the inlets was pressurized at 3 psi, so the total pressure difference between buffer inlets and outlets was 3.54 psi. The pressure at the protein inlet was set by first equilibrating the pressure to that in the mixing region (zero flow through the protein inlet) and then increasing it by 2 inches of water column.

Because the flow rate through the protein inlet and measurement outlet was much smaller that through each of the buffer inlets and outlets, the flow rate through the reaction chamber was controlled by the pressure difference between the buffer inlets and the buffer outlets. The width of the focused stream was controlled by the ratio of the pressure difference between the protein inlet and the mixing region to the pressure difference between the buffer inlets and the mixing region. The resistances of the micro-channels were chosen so that at equal inlet pressures, the protein flow rate was >600 times lower than the combined buffer flow rate. The buffer inlet pressures were first set equal and then carefully tuned to adjust the lateral position of the focused protein stream in the mixing chamber, thus

selecting the part of the protein stream (and its diffusive tails) directed to the measurement channel. Typically, by increasing the pressure of one of the buffer inlets by 0.4 psi (from the initial 3.5 psi), the protein stream could be completely diverted to one of the buffer outlet, with no protein molecules detectable in the measurement channel. Finally, adjustment of pressures at the buffer outlets and measurement outlet made it possible to control the distribution of flow between the outlets and the flow velocity in the measurement channel. The accessible range of velocities in the measurement channel was from 0.1 mm/s to 10 mm/s.

Device characterization

Flow rate measurements. Several methods were used to characterize the volumetric flow rates and flow velocities in the device. High resolution Fluorescence Correlation Spectroscopy (FCS) measurements of flow velocity in the reaction chamber and measurement channel of the device are shown in Fig. 4.10. Where possible, these measurements were corroborated by streakline measurement of flow velocity or volumetric flow rate measurements with calibrated syringes.

The volumetric flow rate through the buffer inlets was measured by connecting the PTFE tubing to 100 μL Hamilton syringes. With equal pressures at the buffer inlets, the flow rate through the mixing region of the device is approximately twice the flow rate through each of the buffer inlets and also twice the flow rate through each of the buffer outlets. (The flow through the protein inlet and measurement outlet are each <0.5% of the buffer flow.) For all buffer inlet pressures tested, the volumetric flow rate through the two buffer inlets were within 5% of each other, which was within the experimental error. The volumetric flow rate through the buffer inlets increased linearly with the difference in pressure between the inlets and the outlets. At the pressure difference of 3.5 psi, the volumetric flow rate through the mixing region was 6.8 μL/min corresponding to a maximal flow velocity, v_{max}, of 0.75 m/s.

The flow rate through the protein inlet and measurement outlet were too low to be measured with a Hamilton syringe. Therefore, we measured these flow rates by analyzing steaklines of 0.99 μm fluorescent polystyrene beads (Bangs Laboratory Inc., Fishers, IN). To make them neutrally buoyant, the beads were suspended in a 7% solution of KI that

was fed into the protein inlet. The buffer inlets were both fed with KI solution without beads. Streaklines produced by the beads were photographed under fluorescence illumination using a SonyX700 camera, 1X coupler, Nikon TE300 microscope, and a 40/1.15 WI objective. The maximal flow velocity in the channels was evaluated as the length of the longest streaklines divided by the exposure time, and the volumetric flow rate in the channel was calculated from the known cross-section of the channel using the equations for fully developed laminar flow. The volumetric flow rate through the protein inlet was a linear function of the difference in pressure between the inlet and the reaction chamber and had a value of $\sim$0.01 μL/min at the conditions of the experiments with proteins reported in the paper. The volumetric flow rate through the measurement outlet was 0.02 μl/min at the experimental conditions.

The streakline measurement technique was not readily applicable in the sheath flow region, and more importantly, in the region between the reaction chamber and the measurement channel in the microfluidic device, because the flow velocity sharply changed on a scale of $<$10 μm. The velocity profile in this region was essential for calculating the protein folding reaction time, which was the time between the buffer exchange and the arrival of the sample at the measurement point. Therefore, the velocity profile was measured with FCS, which had a spatial resolution of $<$0.5 μm (diameter of the confocal volume). The dependence of flow velocity on the position along the channel, $v(x)$, measured with FCS was then used to calculate the reaction time as $t = \int_0^{x'} \frac{dx}{v(x)}$, where x is the coordinate along the channel and x' is the location of the measurement point (the time as a function of x is shown in Fig. 4.10d).

The result of an FCS measurement is a temporal autocorrelation curve (Fig. 4.13c) and a correlation time, τ, derived from the curve.[TL07] The time $\tau = w_0/v$, where w_0 is the characteristic width of the confocal volume of the FCS setup and v is the velocity of the molecules through the confocal volume. Therefore, to convert τ into $v(x)$, the FCS setup needs to be calibrated with flows of known velocity. To perform this calibration, we built a simple microfluidic device with 5 rectilinear segments with different widths and different flow velocities. The device had the same depth of channels (15 μm) as the device used in the experiments with protein. The maximal flow velocity in each segment was measured

both by analyzing particle streaklines and with FCS. Since the volumetric flow rate was the same in all segments, the ratios between the maximal flow velocities and the volumetric flow rate were corroborated by numerical simulations of a fully developed laminar flow in the segments. To increase the range of flow velocities, the pressure between the inlet and outlet was varied. The dependence of the inverse correlation time, $1/\tau$, on the flow velocity, v_{max}, was linear, indicating that the measurement setup was operating properly, and the slope of the best linear fit to the dependence of v_{max} on $1/\tau$ was used for the conversion of $1/\tau$ into flow velocity in the microfluidics device described in the paper (Fig. 4.14).

Characterization of medium exchange and sample dilution. In laminar sheath-flow mixers, such as the one presented here, carrier medium exchange occurs exclusively by diffusion. The protein stream is tightly focused by buffer sheath flows on either side, squeezing the protein stream to an estimated width of ∼21 nm . Small molecules from the sheathing fluid rapidly diffuse into the protein stream, while proteins more slowly diffuse out of the sample stream. The protein diffusion produces a Guassian protein concentration profile in the reaction chamber, with the extension of the profile tails governed by the diffusivity of the protein.

Given the diffusivity of SDS monomers, $D = 600\ \mu\text{m}^2/\text{s}$, and the estimated width of the sample solution stream, $w_p = 21$ nm, the diffusive exchange of SDS between the buffer and sample streams occurs at a time scale $t_{ex} = w_p^2/(8D) \approx 0.1\ \mu$s. The mixing channel is 100 μm long, and the flow velocity of the center of the stream is ∼1 m/s. So the time available for the buffer exchange is ∼100 μs. The profile of concentration of SDS monomers in the channel resulting from diffusion and convection in the flow, as numerically calculated with FemLab, is shown in Fig. 4.15.

As described above, the concentration of protein in the measurement channel could be tuned during experiments by applying a higher pressure to one inlet than to the other. A particularly convenient way of adjusting the difference between the inlet pressures was always to decrease the pressure at the second inlet by an amount equal to the increase in pressure at the first inlet, ΔP, so that the sum of the two pressures remains constant. Because the microchannel network was symmetric with respect to the two inlets, this type of pressure variation did not change the flow rate or pressure in the measurement channel

and thus did not change the sample flow rate or width of the sample stream.

To experimentally evaluate the variations of protein concentration in the measurement channel caused by changes in the buffer inlet pressures, we used FITC ($D = 450$ μm^2/s) and FITC labeled dextran (FITCD) with a molecular weight of 77 KDa and diffusivity $D = 23$ μm^2/s. Diffusivities of many proteins, including α-Synuclein, are between those of FITC and FITCD. A solution of fluorescent dye (either FITC or FITCD in PBS) was fed to the protein inlet and plain PBS buffer in the buffer inlets and measured the fluorescence near the middle of the measurement channel as a function of ΔP (Fig. 4.16a). The reference point of $\Delta P = 0$ corresponded to the buffer inlet pressures adjusted for a maximum of the fluorescence (both near 3.5 psi). Fluorescence micrographs of the measurement and buffer diversion channels are shown in Fig. 4.16b-c (with false green and red color for FITC and FITCD, respectively) for two representative cases, $\Delta P = 0$ and $\Delta P = 0.5$ kPa (2 inches of water column). The plot in Fig. 4.16a indicates that the variation of the buffer inlet pressures can be effectively used for substantial dilution of the protein concentration.

Protein Expression, Purification and Labeling. The plasmid construct for wildtype α-synuclein was kindly provided by R. L. Nussbaum (National Institutes of Health, Bethesda, MD). QuickChange site-directed mutagenesis (Stratagene) was performed to generate the single cysteine (G7C and G84C) and double cysteine (G7C, G84C) mutants used in this study. Expression and purification of wildtype and mutant proteins were carried out following the procedure described previously [FD07].

For protein labeling, α-synuclein cys mutants were reacted with Alexa Fluor 488 maleimide (donor) and Alexa Fluor 594 maleimide (acceptor) dyes (Molecular Probes, Inc.) in 6M guanidine hydrochloride, 50 mM Tris, pH 7.2, 4 °C, overnight in the dark. For the mono-labeled proteins, either the G7C or G84C mutant was reacted with 5-fold excess concentration of dye (using either donor or acceptor dyes). The monolabeled proteins were subsequently purified from the unlabeled proteins using an analytical C4 reversed phase HPLC column. The identity and purity of the reaction products were verified by MALDI-TOF mass spectrometry (Scripps Center for Mass Spectrometry).

For the preparation of the dual-labeled protein, the double cys mutant was first reacted with an equimolar ratio of the donor dye, and subsequently purified by HPLC

(separating the singly-labeled protein from the unlabeled and double-labeled protein) and lyophilized in the dark. The masses of the appropriate HPLC fractions were checked by mass spectrometry to confirm the degree of labeling and purity. The verified singly-labeled protein was then reacted with a 5-fold excess concentration of the acceptor dye and purified as described above.

Single-molecule FRET measurements. Single-molecule FRET measurements were performed as previously described. Briefly, experiments were carried out on a home-built laser confocal microscope system, using an Axiovert 200 microscope (Zeiss, Thornwood, NY).

To excite the fluorescence, we used the 488 nm line of a 543-AP-A01 tunable argon-ion laser (Melles Griot, Carlsbad, CA). The excitation beam was focused inside the sample solution near the mid-plane of the measurement channel (at $\sim$7.5 μm from its bottom and top walls), using a 63x, 1.2 NA, water immersion objective lens (Zeiss, Thornwood, NY). The fluorescence emission was collected using the same objective, separated from the excitation light using a dichroic mirror (Q495LP, Chroma Tech. Corp., Rockingham, VT), spatially filtered with a 100 μm pinhole , and separated into donor and acceptor components using a second dichroic mirror (560 DCXR, Chroma). The donor and acceptor signals were further filtered using an HQ 525/50M band-pass filter (Chroma) for the donor and a 590 LPV2 long-pass filter (Chroma) for the acceptor, and then detected using two SPCM-AQR-14 avalanche photodiode (APD) photon counting modules (Perkin-Elmer Optoelectronics, Fremont, CA). Photon counts were recorded using a photon counting card (PCI 6602, National Instruments, Austin, TX) interfaced with a computer.

The FRET efficiency histograms presented in this paper were generated by using a two-channel data collection mode to simultaneously record donor and acceptor signals as a function of time. Photon emission bursts originating from single molecules were determined using a burst search algorithm as described previously [EBB$^+$01]. A threshold of 30 counts (the sum of signals from the two channels) was used to separate photon bursts due to fluorescent molecules from background. The concentrations of donor-acceptor fluorophore pairs were $\sim$ 100 pM, ensuring that virtually all of the detected photon burst events were due to single molecules. The background counts, leakage of donor into acceptor channel

(∼8%) and the direct excitation of acceptor (∼5%) were estimated in separate experiments, and used to correct the signals before FRET analysis.

FRET efficiencies, E_{FRET}, were calculated for each accepted event from the numbers of donor and acceptor photons, I_D and I_A, using the equation $E_{FRET} = \frac{I_A}{I_A+\gamma I_D}$, and plotted in the form of a histogram. γ for this system was found to be 1.08 ± 0.03 (detail available in the SI to [Fer09]. The FRET-efficiency histograms were fitted with Gaussian functions using Origin (OriginLab Corp., Northampton, MA) and IGOR (WaveMetrics, Lake Oswego, OR), and the positions of the values of E_{FRET} at the maxima and areas under the peaks and were obtained from the fitting parameters. The smFRET three-dimensional maps displayed in Fig. 4.12 represents twenty three separate histograms.

ACKNOWLEDGEMENTS

This work was supported by grants PHY0750049 and OCE-0428900 from the National Science Foundation (A.A.D., V.V., and A.G.), GM073104 from the National Institute of General Medical Science, NIH (A.A.D.), NIH GM62159 (P.G.S.) the Alexander von Humboldt Foundation (E.A.L.) and La Jolla Interface In Science program (Y.G).

Chapter 4.2 is in preparation for publication in Non-reversible folding pathway in a-Synuclein revealed in a single-molecule microfluidic mixer. Gambin, Yann; Ferreon, Allan; VanDelinder, Virginia; Lemke, Edward; Groisman, Alex; Deniz, Ashok. Dissertation author was a participating investigator of this paper.

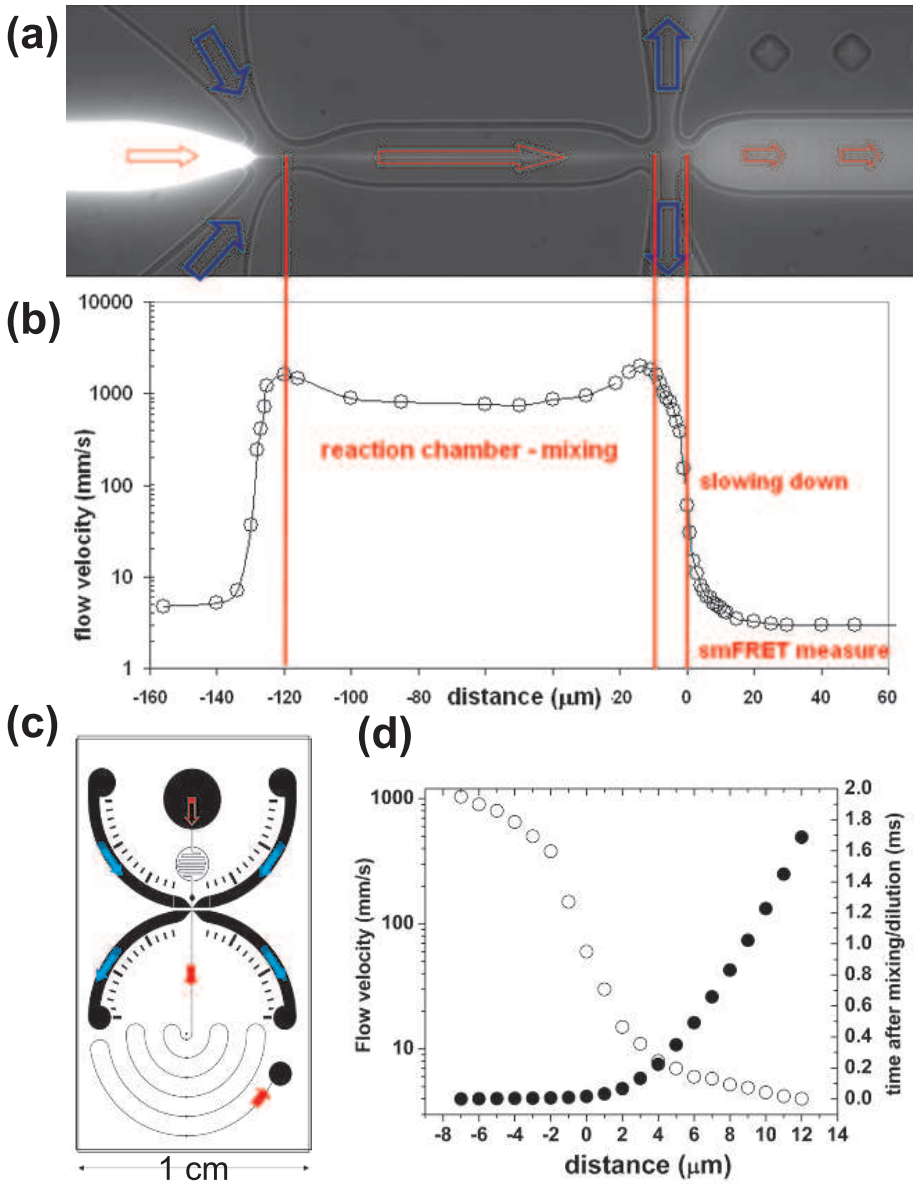

Figure 4.10: (a) Micrograph (mixed fluorescence and brightfield illumination) of the functional region of the device, showing sheath-flow, reaction chamber, and deceleration region. Blue arrows show direction of buffer flow; red arrows mark the flow of sample (fluorescent stream). (b) The flow velocity along the centerline of the mixing channel as measured with fluorescence correlation spectroscopy (FCS). (c) A schematic of the microfluidic device. (d) Graph of flow velocity (hollow circles) and time after medium exchange (solid circles) along centerline of mixing chamber and measurement channel, with the distance axis the same as in (a) and (b).

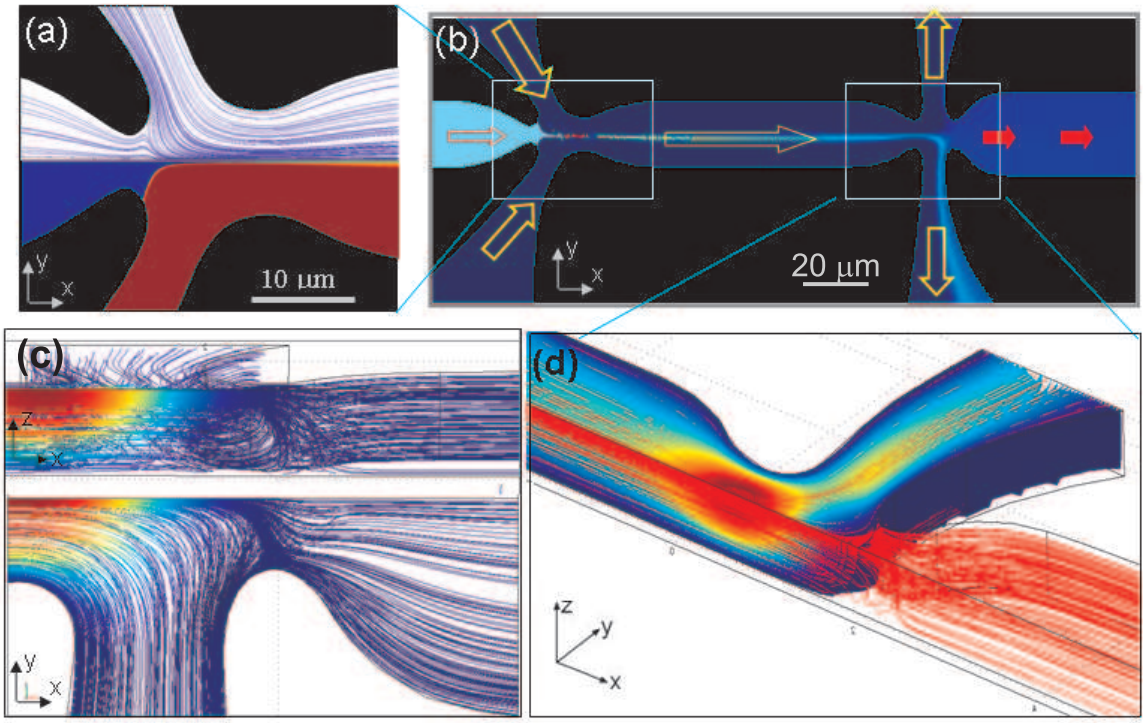

Figure 4.11: (a) Laminar mixing in a sheath-flow. Upper and lower halves show stream lines and concentrations, respectively. Sample stream (blue) is squeezed between two buffer streams (red). (b) Simulation of device with unequal flow rates of buffer from the two sides of the sample stream. Only a portion of the diffusion-formed tail of the sample stream enters the measurement channel. (c to e) Due to inertial effects in the deceleration region, only the part of the sample moving at the longitudinal axis of symmetry of the reaction chamber enters the measurement channel. The streamlines in (c) are color-coded with flow velocity (red 2 m/s, blue 2 mm/s), while the streamlines in (d) do not show velocity. These simulation images only show one quarter of the channel; the maximum z-extent shown is the height/2.

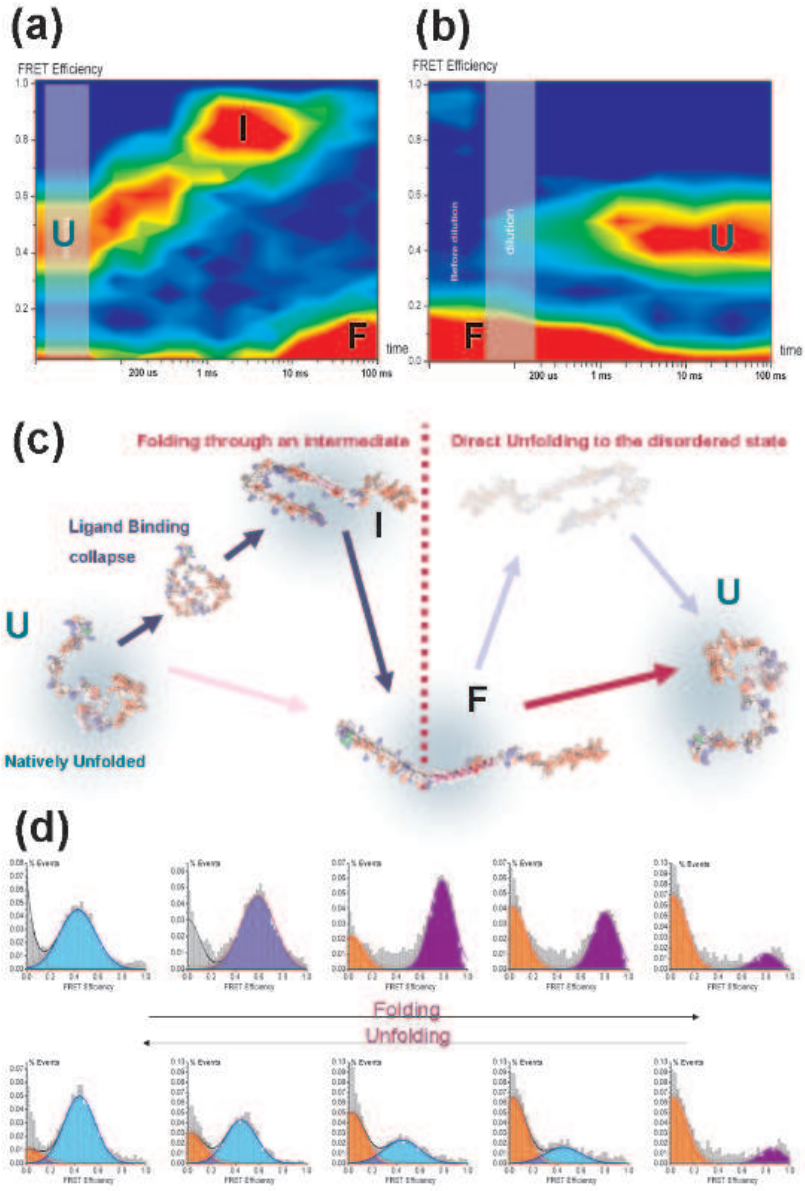

Figure 4.12: Folding and unfolding of α-synuclein. (a) Color-coded histogram histogram of FRET efficiency, E_{FRET}, as a function of time after the addition of SDS to the protein sample. Protein in denaturated state is mixed with a buffer containging SDS at a concentration corresponding to F-state and FRET is measured as folding progress in time. Red and blue correspond to E_{FRET} of 1 and 0, respectively. (b) Color-coded histogram of E_{FRET} as a function of time after SDS is removed from a protein sample, which is initially in the F-state with SDS bound to the protein (c) Diagram of the proteins state transitions. (d) Representative FRET histograms of the folding and unfolding reactions.

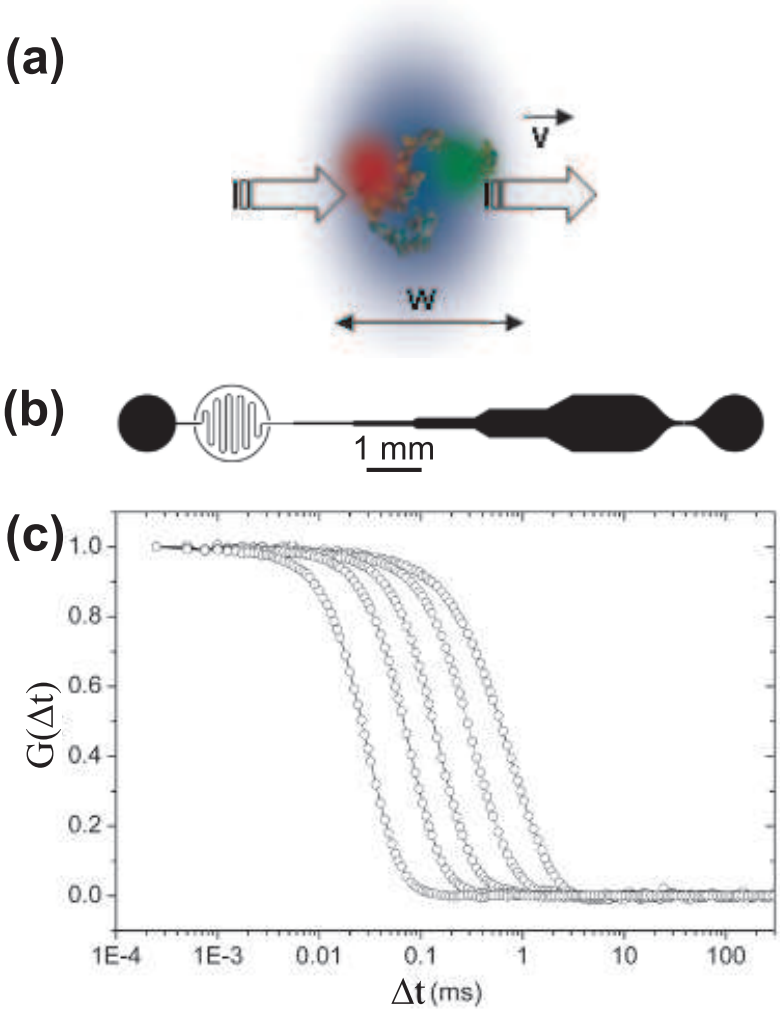

Figure 4.13: FCS flow rate measurements. (a) The device used to calibrate the FCS measurments. (b) Cartoon of molecule convecting through the confocal volume. (c) FCS correlation curves obtained at various velocities, where $G(\Delta t)$ is the temporal autocorrelation function.

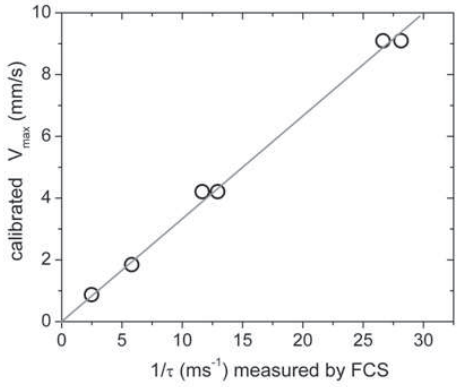

Figure 4.14: FCS calibration curve. The y-axis is the velocity as measured with streaklines, and the x-axis is the FCS measurement at the same conditions. The dependence of v_{max} on $\frac{1}{\Delta t}$ was fitted with a straight line crossing the origin and the slope of the line was used to translate the FCS measurements into velocities in the microfluidic device.

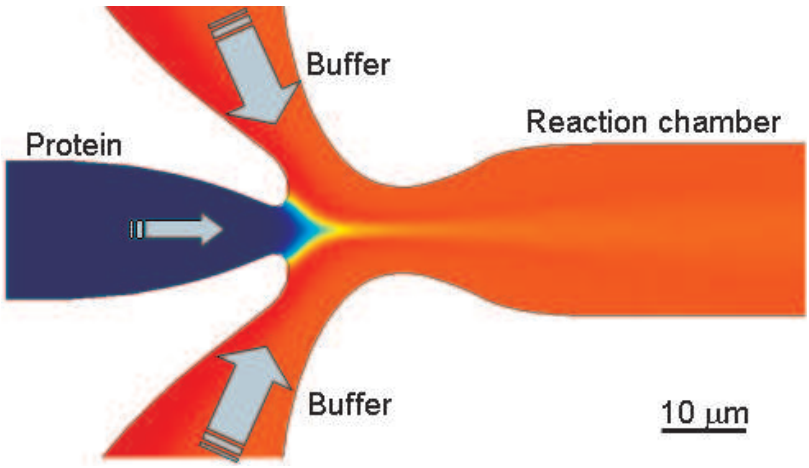

Figure 4.15: SDS monomer concentration from a numerical simulation of flow and diffusion in the mixing region (red is 100%, dark blue is 0%).

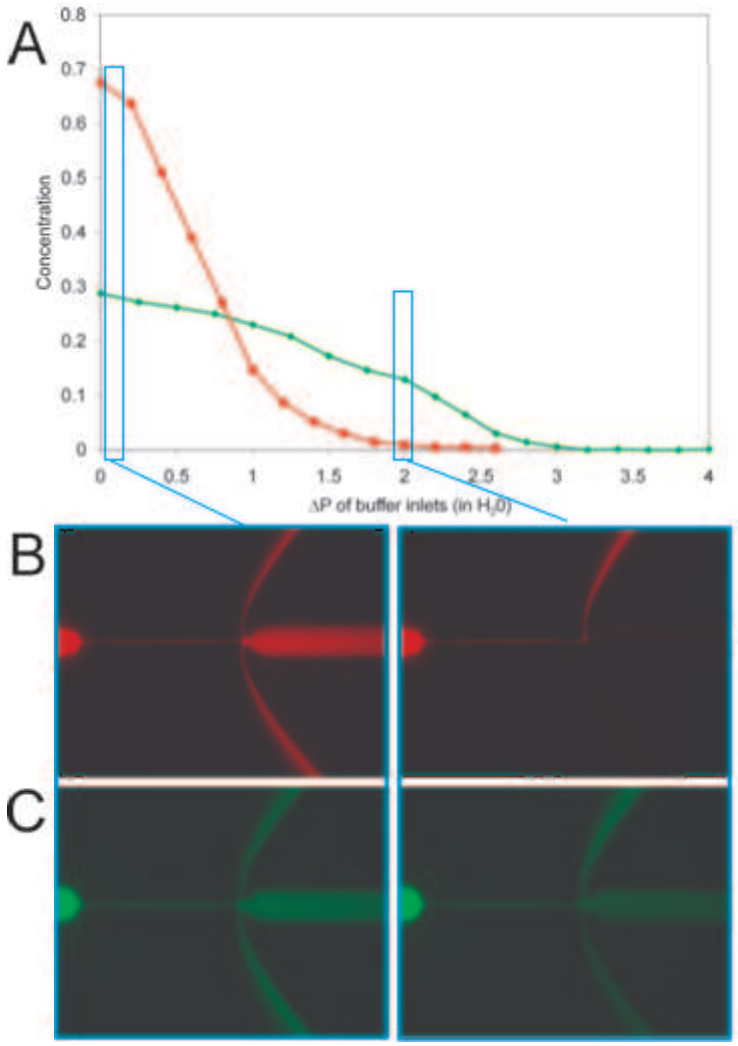

Figure 4.16: To tune the concentration of sample in the measurement channel, the pressures at the two buffer inlets are changed asymmetrically, by ΔP and $-\Delta P$ with respect to a reference point. a) Plot of fluorescence near the middle of the measurement channel as a function of ΔP for FITC (green line) and 77KDa FITC-Dextran (red line). The fluorescence is normalized to its value for the original solutions of FITC and FITCD, respectively. b) Images of the functional area of the device with 77KDa FITC-Dextran (false color red) at $\Delta P = 0$ (left) and $\Delta P = 0.5$ kPa (right). c) Image of the functional area of the device with FITC (false color green) at $\Delta P = 0$ (left) and $\Delta P = 0.5$ (right).

Bibliography

[ADH+93] A. C. Aho, K. Donner, S. Helenius, L. O. Larsen, and T. Reuter. Visual performance of the toad (bufo-bufo) at low-light levels - retinal ganglion-cell responses and prey-catching accuracy. *Journal of Comparative Physiology a-Sensory Neural and Behavioral Physiology*, 172(6):671–682, 1993. Times Cited: 32 Cited Reference Count: 37 English Article J COMP PHYSIOL A LK508.

[Aid98] D.J. Aidley. *The Physiology of Excitable Cells*. Cambridge University Press, Cambridge, 4th edition, 1998.

[AT93] M. V. Abrahams and L. D. Townsend. Bioluminescence in dinoflagellates - a test of the burglar alarm hypothesis. *Ecology*, 74(1):258–260, 1993. Times Cited: 25 Cited Reference Count: 16 English Note ECOLOGY KF775.

[BB85] J. H. S. Blaxter and R. S. Batty. The development of startle responses in herring larvae. *Journal of the Marine Biological Association of the United Kingdom*, 65(3):737–750, 1985. Times Cited: 51 Cited Reference Count: 18 English Article J MAR BIOL ASSN UK ANU26.

[BDZ94] G. Belfort, R. H. Davis, and A. L. Zydney. The behavior of suspensions and macromolecular solutions in cross-flow microfiltration. *Journal of Membrane Science*, 96(1-2):1–58, 1994.

[BH03] E. J. Buskey and D. K. Hartline. High-speed video analysis of the escape responses of the copepod acartia tonsa to shadows. *Biological Bulletin*, 204(1):28–37, 2003. Times Cited: 9 Cited Reference Count: 54 English Article BIOL BULL 647NJ.

[BHC63] J. Buck, F. E. Hanson, and J. F. Case. Control of flashing in fireflies .3. peripheral excitation. *Biological Bulletin*, 125(2):251, 1963. Times Cited: 27 Cited Reference Count: 9 English Article BIOL BULL 7202A.

[BLH02] E. J. Buskey, P. H. Lenz, and D. K. Hartline. Escape behavior of planktonic copepods in response to hydrodynamic disturbances: high speed video analysis. *Marine Ecology-Progress Series*, 235:135–146, 2002. Times Cited: 19 Cited Reference Count: 53 English Article MAR ECOL-PROGR SER 576DW.

[BLSD08] Eric M. Brustad, Edward A. Lemke, Peter G. Schultz, and Ashok A. Deniz. A general and efficient method for the site-specific dual-labeling of proteins for single molecule fluorescence resonance energy transfer. *J Am Chem Soc*, 130(52):17664–5, 2008. Times Cited: 0.

[BMS83] E. Buskey, L. Mills, and E. Swift. The effects of dinoflagellate bioluminescence on the swimming behavior of a marine copepod. *Limnology and Oceanography*, 28(3):575–579, 1983. Times Cited: 45 Cited Reference Count: 14 English Note LIMNOL OCEANOGR QT112.

[BOFY96] J. P. Brody, T. D. Osborn, F. K. Forster, and P. Yager. A planar microfabricated fluid. *Sensors and Actuators a-Physical*, 54(1-3):704–708, 1996.

[BOSW95] J. D. Bryngelson, J. N. Onuchic, N. D. Socci, and P. G. Wolynes. Funnels, pathways, and the energy landscape of protein-folding - a synthesis. *Proteins-Structure Function and Genetics*, 21(3):167–195, 1995. Times Cited: 1066.

[Bre61] H. Brenner. The slow motion of a sphere through a viscous fluid towards a plane surface. *Chemical Engineering Science*, 16(3-4):242–251, 1961. Times Cited: 677 Cited Reference Count: 17 English Article CHEM ENG SCI XG765.

[BRSW85] E. J. Buskey, G. T. Reynolds, E. Swift, and A. J. Walton. Interactions between copepods and bioluminescent dinoflagellates - direct observations using image intensification. *Biological Bulletin*, 169(2):530–530, 1985. Times Cited: 12 Cited Reference Count: 0 English Meeting Abstract BIOL BULL AUC55.

[Bru08] H. Bruus. *Theoretical Microfluidics*. Oxford University Press, Oxford, 2008.

[BS83] E. J. Buskey and E. Swift. Behavioral-responses of the coastal copepod acartia-hudsonica (pinhey) to simulated dinoflagellate bioluminescence. *Journal of Experimental Marine Biology and Ecology*, 72(1):43–58, 1983. Times Cited: 24 Cited Reference Count: 27 English Article J EXP MAR BIOL ECOL RL493.

[BS85] E. J. Buskey and E. Swift. Behavioral-responses of oceanic zooplankton to simulated bioluminescence. *Biological Bulletin*, 168(2):263–275, 1985. Times Cited: 23 Cited Reference Count: 36 English Article BIOL BULL AGJ83.

[BSBS69] W. H. Biggley, E. Swift, R. J. Buchanan, and H. H. Seliger. Stimulable and spontaneous bioluminescence in marine dinoflagellates, pyrodinium bahamense, gonyaulax polyedra, and pyrocystis lunula. *Journal of General Physiology*, 54(1P1):96, 1969. Times Cited: 71 Cited Reference Count: 17 English Article J GEN PHYSIOL D6765.

[BT96] Orrit M Wild UP Basche T, Moerner WE. *Single-Molecule Optical Detection, Imaging and Spectroscopy*. VCH, Weinheim, 1996.

[BW87] J. D. Bryngelson and P. G. Wolynes. Spin-glasses and the statistical-mechanics of protein folding. *Proceedings of the National Academy of Sciences of the United States of America*, 84(21):7524–7528, 1987. Times Cited: 798.

[CCR+03] S. Chandra, X. C. Chen, J. Rizo, R. Jahn, and T. C. Sudhof. A broken alpha-helix in folded alpha-synuclein. *Journal of Biological Chemistry*, 278(17):15313–15318, 2003.

[CD06] F. Chiti and C. M. Dobson. Protein misfolding, functional amyloid, and human disease. *Annual Review of Biochemistry*, 75:333–366, 2006. Times Cited: 301 Cited Reference Count: 192 English Review ANNU REV BIOCHEM 074JD.

[CGC+97] R. H. Carlson, C. V. Gabel, S. S. Chan, R. H. Austin, J. P. Brody, and J. W. Winkelman. Self-sorting of white blood cells in a lattice. *Physical Review Letters*, 79(11):2149–2152, 1997.

[CH07] P. V. Cornish and T. Ha. A survey of single-molecule techniques in chemical biology. *Acs Chemical Biology*, 2(1):53–61, 2007. Times Cited: 30.

[CL03] C. Coufort and A. Line. Forces on spherical particles in terms of upstream flow characteristics. *Chemical Engineering Research and Design*, 81(A9):1206–1211, 2003. Times Cited: 4 Cited Reference Count: 12 English Proceedings Paper CHEM ENG RES DES 752KA.

[CLF03] A. K. Chen, M. I. Latz, and J. A. Frangos. The use of dinoflagellate bioluminescence to characterize cell stimulation in bioreactors. *Biotechnology and Bioengineering*, 83(1):93–103, 2003. Times Cited: 11 Cited Reference Count: 55 English Article BIOTECHNOL BIOENG 682NW.

[CLL05] W. C. Chang, L. P. Lee, and D. Liepmann. Biomimetic technique for adhesion-based collection and separation of cells in a microfluidic channel. *Lab on a Chip*, 5(1):64–73, 2005.

[CLS98] S. Chien, S. Li, and J. Y. J. Shyy. Effects of mechanical forces on signal transduction and gene expression in endothelial cells. *Hypertension*, 31(1):162–169, 1998. Times Cited: 278 Cited Reference Count: 89 English Proceedings Paper HYPERTENSION Part 2 Suppl. S YV789.

[CLSF07] A. K. Chen, M. I. Latz, P. Sobolewski, and J. A. Frangos. Evidence for the role of g-proteins in flow stimulation of dinoflagellate bioluminescence. *American Journal of Physiology-Regulatory Integrative and Comparative Physiology*, 292(5):R2020–R2027, 2007. Times Cited: 3 Cited Reference Count: 58 English Article AMER J PHYSIOL-REGUL INTEGR C 185QJ.

[CLZ+01] B. P. C. Chen, Y. S. Li, Y. H. Zhao, K. D. Chen, S. Li, J. M. Lao, S. L. Yuan, J. Y. J. Shyy, and S. Chien. Dna microarray analysis of gene expression in endothelial cells in response to 24-h shear stress. *Physiological Genomics*, 7(1):55–63, 2001. Times Cited: 93 Cited Reference Count: 54 English Article PHYSIOL GENOMICS 481BV.

[CP05] T. A. Crowley and V. Pizziconi. Isolation of plasma from whole blood using planar microfilters for lab-on-a-chip applications. *Lab on a Chip*, 5(9):922–929, 2005.

[CR06] E. D. Clotfelter and A. C. Rodriguez. Behavioral changes in fish exposed to phytoestrogens. *Environmental Pollution*, 144(3):833–839, 2006. Times Cited: 6 Cited Reference Count: 84 English Article ENVIRON POLLUT 094PX.

[Cra06] H. Craighead. Future lab-on-a-chip technologies for interrogating individual molecules. *Nature*, 442(7101):387–393, 2006. Times Cited: 90 Cited Reference Count: 83 English Review NATURE 067CI.

[Cri68] C. M. Cripps. Rapid method for estimation of plasma haemoglobin levels. *Journal of Clinical Pathology*, 21(1):110, 1968.

[CTF+02] N. Christodoulides, M. Tran, P. N. Floriano, M. Rodriguez, A. Goodey, M. Ali, D. Neikirk, and J. T. McDevitt. A microchip-based multianalyte assay system for the assessment of cardiac risk. *Analytical Chemistry*, 74(13):3030–3036, 2002.

[DC97] K. A. Dill and H. S. Chan. From levinthal to pathways to funnels. *Nature Structural Biology*, 4(1):10–19, 1997. Times Cited: 994.

[DCAL06] D. Di Carlo, N. Aghdam, and L. P. Lee. Single-cell enzyme concentrations, kinetics, and inhibition analysis using high-density hydrodynamic cell isolation arrays. *Analytical Chemistry*, 78(14):4925–4930, 2006.

[DCR+05] A. K. Dunker, M. S. Cortese, P. Romero, L. M. Iakoucheva, and V. N. Uversky. Flexible nets - the roles of intrinsic disorder in protein interaction networks. *Febs Journal*, 272(20):5129–5148, 2005. Times Cited: 135 Cited Reference Count: 204 English Proceedings Paper FEBS J 972FE.

[DDG+99] A. A. Deniz, M. Dahan, J. R. Grunwell, T. J. Ha, A. E. Faulhaber, D. S. Chemla, S. Weiss, and P. G. Schultz. Single-pair fluorescence resonance energy transfer on freely diffusing molecules: Observation of forster distance dependence and subpopulations. *Proceedings of the National Academy of Sciences of the United States of America*, 96(7):3670–3675, 1999. Times Cited: 219 Cited Reference Count: 31 English Proceedings Paper PROC NAT ACAD SCI USA 182PT.

[deM06] A. J. deMello. Control and detection of chemical reactions in microfluidic systems. *Nature*, 442(7101):394–402, 2006. Times Cited: 90 Cited Reference Count: 96 English Review NATURE 067CI.

[DJCG98] W. S. Davidson, A. Jonas, D. F. Clayton, and J. M. George. Stabilization of alpha-synuclein secondary structure upon binding to synthetic membranes. *Journal of Biological Chemistry*, 273(16):9443–9449, 1998.

[DLB+00] A. A. Deniz, T. A. Laurence, G. S. Beligere, M. Dahan, A. B. Martin, D. S. Chemla, P. E. Dawson, P. G. Schultz, and S. Weiss. Single-molecule protein folding: Diffusion fluorescence resonance energy transfer studies of the denaturation of chymotrypsin inhibitor 2. *Proceedings of the National Academy of Sciences of the United States of America*, 97(10):5179–5184, 2000. Times Cited: 212 Cited Reference Count: 36 English Article PROC NAT ACAD SCI USA 313KH.

[DMB56] H. L. Dryden, F. D. Murnaghan, and H. Bateman. *Hydrodynamics*. Dover, New York, 1956.

[DMGM+05] C. Del Mar, E. A. Greenbaum, L. Mayne, S. W. Englander, and V. L. Woods. Structure and properties of alpha-synuclein and other amyloids determined at the amino acid level. *Proceedings of the National Academy of Sciences of the United States of America*, 102(43):15477–15482, 2005.

[DML08] A. A. Deniz, S. Mukhopadhyay, and E. A. Lemke. Single-molecule biophysics: at the interface of biology, physics and chemistry. *Journal of the Royal Society Interface*, 5:15–45, 2008. Times Cited: 5.

[DMYDG+02] S. A. Dames, M. Martinez-Yamout, R. N. De Guzman, H. J. Dyson, and P. E. Wright. Structural basis for hif-1 alpha/cbp recognition in the cellular hypoxic response. *Proceedings of the National Academy of Sciences of the United States of America*, 99(8):5271–5276, 2002. Times Cited: 125.

[Dob03] C. M. Dobson. Protein folding and misfolding. *Nature*, 426(6968):884–890, 2003.

[DP98] D. Rickwood D. Patel, T.C. Ford. *Cell Separation: A Practical Approach*. The Practical Approach Series. Oxford University Press, Oxford, 1998.

[DS05] G. B. Deane and M. D. Stokes. A quantitative model for flow-induced bioluminescence in dinoflagellates. *Journal of Theoretical Biology*, 237(2):147–169, 2005. Times Cited: 1 Cited Reference Count: 57 English Article J THEOR BIOL 980CR.

[DSJCL03] A. Der-Sarkissian, C. C. Jao, J. Chen, and R. Langen. Structural organization of alpha-synuclein fibrils studied by site-directed spin labeling. *Journal of Biological Chemistry*, 278(39):37530–37535, 2003.

[EAGG+05] J. El-Ali, S. Gaudet, A. Gunther, P. K. Sorger, and K. F. Jensen. Cell stimulus and lysis in a microfluidic device with segmented gas-liquid flow. *Analytical Chemistry*, 77(11):3629–3636, 2005. Times Cited: 23 Cited Reference Count: 33 English Article ANAL CHEM 932OA.

[EBB+01] C. Eggeling, S. Berger, L. Brand, J. R. Fries, J. Schaffer, A. Volkmer, and C. A. M. Seidel. Data registration and selective single-molecule analysis using multi-parameter fluorescence detection. *Journal of Biotechnology*, 86(3):163–180, 2001. Times Cited: 83 SI.

[EC72] W. E. Esaias and H. C. Curl. Effect of dinoflagellate bioluminescence on copepod ingestion rates. *Limnology and Oceanography*, 17(6):901–905, 1972. Times Cited: 54 Cited Reference Count: 14 English Note LIMNOL OCEANOGR P0129.

[Eck65a] R. Eckert. 2. asynchronous flash initiation by a propagated triggering potential. *Science*, 147(3662):1142, 1965. Times Cited: 17 Cited Reference Count: 13 English Article SCIENCE 61963.

[Eck65b] R. Eckert. Bioelectric control of bioluminescence in dinoflagellate noctiluca .i. specific nature of triggering events. *Science*, 147(3662):1140, 1965. Times Cited: 64 Cited Reference Count: 20 English Article SCIENCE 61963.

[Eck66] R. Eckert. Excitation and luminescence in the dinoflagellate noctiluca miliaris. In Hameda Y. Johnson, F.H., editor, *Bioluminescence in Progress*, pages 269–300. Princton University Press, Princeton, NJ, 1966.

[EDN88] R. C. Eaton, R. Didomenico, and J. Nissanov. Flexible body dynamics of the goldfish c-start - implications for reticulospinal command mechanisms. *Journal of Neuroscience*, 8(8):2758–2768, 1988. Times Cited: 70 Cited Reference Count: 59 English Article J NEUROSCI P8314.

[EHM+03] J. M. Elkins, K. S. Hewitson, L. A. McNeill, J. F. Seibel, I. Schlemminger, C. W. Pugh, P. J. Ratcliffe, and C. J. Schofield. Structure of factor-inhibiting hypoxia-inducible factor (hif) reveals mechanism of oxidative modification of hif-1 alpha. *Journal of Biological Chemistry*, 278(3):1802–1806, 2003. Times Cited: 134.

[ES68] R. Eckert and T. Sibaoka. Flash-triggering action potential of luminescent dinoflagellate noctiluca. *Journal of General Physiology*, 52(2):258, 1968. Times Cited: 45 Cited Reference Count: 26 English Article J GEN PHYSIOL B6504.

[EWB+06] C. Eggeling, J. Widengren, L. Brand, J. Schaffer, S. Felekyan, and C. A. M. Seidel. Analysis of photobleaching in single-molecule multicolor excitation and forster resonance energy transfer measurement. *Journal of Physical Chemistry A*, 110(9):2979–2995, 2006. Times Cited: 28.

[FBS06] M. Friedel, A. Baumketner, and J. E. Shea. Effects of surface tethering on protein folding mechanisms. *Proceedings of the National Academy of Sciences of the United States of America*, 103(22):8396–8401, 2006. Times Cited: 18 Cited Reference Count: 46 English Article PROC NAT ACAD SCI USA 052BX.

[FC95] K. J. Fleisher and J. F. Case. Cephalopod predation facilitated by dinoflagellate luminescence. *Biological Bulletin*, 189(3):263–271, 1995. Times Cited: 23 Cited Reference Count: 30 English Article BIOL BULL TL768.

[FD07] A. C. M. Ferreon and A. A. Deniz. alpha-synuclein multistate folding thermodynamics: Implications for protein misfolding and aggregation. *Biochemistry*, 46(15):4499–4509, 2007. Times Cited: 6.

[Fer09] Gambin Y. Lemke E. Deniz A. Ferreon, A. C. M. Interplay of a-synuclein binding and conformational switching probed by single-molecule fluorescence. *Proceedings of the National Academy of Sciences of the United States of America*, 2009.

[FH71] M. Fogel and J. W. Hastings. Substrate-binding protein in gonyaulax bioluminescence reation. *Archives of Biochemistry and Biophysics*, 142(1):310, 1971. Times Cited: 75 Cited Reference Count: 16 English Article ARCH BIOCHEM BIOPHYS I5026.

[FP98] H. S. Friedman and C. E. Priebe. Estimating stimulus response latency. *Journal of Neuroscience Methods*, 83(2):185–194, 1998. Times Cited: 13 Cited Reference Count: 18 English Article J NEUROSCI METH 123UZ.

[Fra93] J. A. Frangos. *Physical Forces and the Mammalian Cell*. Academic Press, San Diego, 1993.

[Fun93] Y.C. Fung. *Biomechanics : mechanical properties of living tissues*. Springer-Verlag, New York, 2nd edition, 1993.

[GCF96] S. R. P. Gudi, C. B. Clark, and J. A. Frangos. Fluid flow rapidly activates g proteins in human endothelial cells - involvement of g proteins in mechanochemical signal transduction. *Circulation Research*, 79(4):834–839, 1996. Times Cited: 138 Cited Reference Count: 29 English Article CIRC RES VL228.

[GEQ03] A. Groisman, M. Enzelberger, and S. R. Quake. Microfluidic memory and control devices. *Science*, 300(5621):955–958, 2003. Times Cited: 107 Cited Reference Count: 14 English Article SCIENCE 675WD.

[GG07] E. Gutierrez and A. Groisman. Quantitative measurements of the strength of adhesion of human neutrophils to a substratum in a microfluidic device. *Analytical Chemistry*, 79(6):2249–2258, 2007. Times Cited: 5 Cited Reference Count: 34 English Article ANAL CHEM 145LR.

[Gid93] J. C. Giddings. Field-flow fractionation - analysis of macromolecular, colloidal, and particulate materials. *Science*, 260(5113):1456–1465, 1993.

[GLC+05] A. Groisman, C. Lobo, H. Cho, J. K. Campbell, Y. S. Dufour, A. M. Stevens, and A. Levchenko. A microfluidic chemostat for experiments with bacterial and yeast cells. *Nature Meth.*, 2:685 – 689, 2005.

[GR62] R. R. Guillard and J. H. Ryther. Studies of marine planktonic diatoms .1. cyclotella nana hustedt, and detonula confervacea (cleve) gran. *Canadian Journal of Microbiology*, 8(2):229, 1962. Times Cited: 3000 Cited Reference Count: 28 English Article CAN J MICROBIOL 8067A.

[Gre00] Pieper R.E. Gregario, D.E. Investigations of red tides along the southern california coast. *Bull. Couth. Calif. Acad. Sci.*, 99:147–160, 2000.

[Har76] W. G. Harrison. Nitrate metabolism of red tide dinoflagellate gonyaulax-polyedra stein. *Journal of Experimental Marine Biology and Ecology*, 21(3):199–209, 1976. Times Cited: 63 Cited Reference Count: 31 English Article J EXP MAR BIOL ECOL BN610.

[HBL99] D. K. Hartline, E. J. Buskey, and P. H. Lenz. Rapid jumps and bioluminescence elicited by controlled hydrodynamic stimuli in a mesopelagic copepod, pleuromamma xiphias. *Biological Bulletin*, 197(2):132–143, 1999. Times Cited: 14 Cited Reference Count: 26 English Article BIOL BULL 251AC.

[HD86] J. W. Hastings and J. C. Dunlap. Cell-free components in dinoflagellate bioluminescence - the particulate activity - scintillons - the soluble components - luciferase, luciferin, and luciferin-binding protein. *Methods in Enzymology*, 133:307–327, 1986. Times Cited: 22 Cited Reference Count: 27 English Review METH ENZYMOLOGY J5444.

[Hen86] L.W. Henderson. *Hemofiltration*. Springer-Verlag, Berlin, New York, 1986.

[HET+01] Y. Huang, K. L. Ewalt, M. Tirado, T. R. Haigis, A. Forster, D. Ackley, M. J. Heller, J. P. O'Connell, and M. Krihak. Electric manipulation of bioparticles and macromolecules on microfabricated electrodes. *Analytical Chemistry*, 73(7):1549–1559, 2001.

[HGH+07] W. W. Hu, R. Gladue, J. Hansen, C. Wojnar, and J. J. Chalmers. The sensitivity of the dinoflagellate crypthecodinium cohnii to transient hydrodynamic forces and cell-bubble interactions. *Biotechnology Progress*, 23(6):1355–1362, 2007. Times Cited: 3 Cited Reference Count: 33 English Article BIOTECHNOL PROGR 239VW.

[HGK+05] D. Huh, W. Gu, Y. Kamotani, J. B. Grotberg, and S. Takayama. Microfluidics for flow cytometric analysis of cells and particles. *Physiological Measurement*, 26(3):R73–R98, 2005. Times Cited: 69 Cited Reference Count: 72 English Review PHYSIOL MEAS 936EI.

[HHB+05] H. Heise, W. Hoyer, S. Becker, O. C. Andronesi, D. Riedel, and M. Baldus. Molecular-level secondary structure, polymorphism, and dynamics of full-length alpha-synuclein fibrils studied by solid-state nmr. *Proceedings of the National Academy of Sciences of the United States of America*, 102(44):15871–15876, 2005.

[HIM+06] D. E. Hertzog, B. Ivorra, B. Mohammadi, O. Bakajin, and J. G. Santiago. Optimization of a microfluidic mixer for studying protein folding kinetics. *Analytical Chemistry*, 78(13):4299–4306, 2006. Times Cited: 11.

[HMJ+04] D. E. Hertzog, X. Michalet, M. Jager, X. X. Kong, J. G. Santiago, S. Weiss, and O. Bakajin. Femtomole mixer for microsecond kinetic studies of protein folding. *Analytical Chemistry*, 76(24):7169–7178, 2004. Times Cited: 39.

[Hob66] Edmunds Hobson. Visual orientation and feeding behavior in seals phoca vitulina and sea lions zalophus californianus. *Nature*, 210((5033)):326–327, 1966. Article.

[Hoy89] R. R. Hoy. Startle, categorical response, and attention in acoustic behavior of insects. *Annual Review of Neuroscience*, 12:355–375, 1989. Times Cited: 25 Cited Reference Count: 96 English Review ANNU REV NEUROSCI T5675.

[HSH+04] J. W. Hong, V. Studer, G. Hang, W. F. Anderson, and S. R. Quake. A nanoliter-scale nucleic acid processor with parallel architecture. *Nature Biotechnology*, 22(4):435–439, 2004.

[HW08] K. M. Hamadani and S. Weiss. Nonequilibrium single molecule protein folding in a coaxial mixer. *Biophysical Journal*, 95(1):352–365, 2008. Times Cited: 0.

[IT06] D. Irimia and M. Toner. Cell handling using microstructured membranes. *Lab on a Chip*, 6(3):345–352, 2006.

[Jak01] H. H. Jakobsen. Escape response of planktonic protists to fluid mechanical signals. *Marine Ecology-Progress Series*, 214:67–78, 2001. Times Cited: 25 Cited Reference Count: 39 English Article MAR ECOL-PROGR SER 437DG.

[Jak02] H. H. Jakobsen. Escape of protists in predator-generated feeding currents. *Aquatic Microbial Ecology*, 26(3):271–281, 2002. Times Cited: 14 Cited Reference Count: 32 English Article AQUAT MICROB ECOL 520MV.

[JDSCL04] C. C. Jao, A. Der-Sarkissian, J. Chen, and R. Langen. Structure of membrane-bound alpha-synuclein studied by site-directed spin labeling. *Proceedings of the National Academy of Sciences of the United States of America*, 101(22):8331–8336, 2004.

[JDYP+05] H. J. Jeong, Y. Du Yoo, J. Y. Park, J. Y. Song, S. T. Kim, S. H. Lee, K. Y. Kim, and W. H. Yih. Feeding by phototrophic red-tide dinoflagellates: five species newly revealed and six species previously known to be mixotrophic. *Aquatic Microbial Ecology*, 40(2):133–150, 2005. Times Cited: 23 Cited Reference Count: 62 English Article AQUAT MICROB ECOL 968QG.

[JFM06] D. Janasek, J. Franzke, and A. Manz. Scaling and the design of miniaturized chemical-analysis systems. *Nature*, 442(7101):374–380, 2006. Times Cited: 86 Cited Reference Count: 67 English Review NATURE 067CI.

[JIFH85] C. H. Johnson, S. Inoue, A. Flint, and J. W. Hastings. Compartmentalization of algal bioluminescence - autofluorescence of bioluminescent particles in the dinoflagellate gonyaulax as studied with image-intensified video microscopy and flow-cytometry. *Journal of Cell Biology*, 100(5):1435–1446, 1985. Times Cited: 37 Cited Reference Count: 39 English Article J CELL BIOL AGW28.

[JL02] A. R. Juhl and M. I. Latz. Mechanisms of fluid shear-induced inhibition of population growth in a red-tide dinoflagellate. *Journal of Phycology*, 38(4):683–694, 2002. Times Cited: 21 Cited Reference Count: 55 English Article J PHYCOL 590RU.

[JMHD04] D. Juncker, B. Michel, P. Hunziker, and E. Delamarche. Simultaneous detection of c-reactive protein and other cardiac markers in human plasma using micromosaic immunoassays and self-regulating microfluidic networks. *Biosensors and Bioelectronics*, 19(10):1193–1202, 2004.

[JR05] T. R. Jahn and S. E. Radford. The yin and yang of protein folding. *Febs Journal*, 272(23):5962–5970, 2005.

[Juh05] A. R. Juhl. Growth rates and elemental composition of alexandrium monilatum, a red-tide dinoflagellate. *Harmful Algae*, 4(2):287–295, 2005. Times Cited: 4 Cited Reference Count: 38 English Article HARMFUL ALGAE 899UA.

[JVL00] A. R. Juhl, V. Velazquez, and M. I. Latz. Effect of growth conditions on flow-induced inhibition of population growth of a red-tide dinoflagellate. *Limnology and Oceanography*, 45(4):905–915, 2000. Times Cited: 26 Cited Reference Count: 54 English Article LIMNOL OCEANOGR 323GZ.

[KKP+08] P. Kim, K. W. Kwon, M. C. Park, S. H. Lee, S. M. Kim, and K. Y. Suh. Soft lithography for microfluidics: a review. *Biochip Journal*, 2(1):1–11, 2008. Times Cited: 2 Cited Reference Count: 83 English Review BIOCHIP J 341DL.

[KNHW07] X. X. Kong, E. Nir, K. Hamadani, and S. Weiss. Photobleaching pathways in single-molecule fret experiments. *Journal of the American Chemical Society*, 129(15):4643–4654, 2007. Times Cited: 6.

[KRK92] D. Kamykowski, R. E. Reed, and G. J. Kirkpatrick. Comparison of sinking velocity, swimming velocity, rotation and path characteristics among 6 marine dinoflagellate species. *Marine Biology*, 113(2):319–328, 1992. Times Cited: 48 Cited Reference Count: 34 English Article MAR BIOL JA911.

[KVBA98] J. B. Knight, A. Vishwanath, J. P. Brody, and R. H. Austin. Hydrodynamic focusing on a silicon chip: Mixing nanoliters in microseconds. *Physical Review Letters*, 80(17):3863–3866, 1998. Times Cited: 292.

[Lat05] Rohr J. Latz, M.I. Glowing with the flow:ecology and applications of flow-stimulated bioluminescence. *Optics and Photonics News*, 16:40–45, 2005.

[LCG94] M. I. Latz, J. F. Case, and R. L. Gran. Excitation of bioluminescence by laminar fluid shear associated with simple couette-flow. *Limnology and Oceanography*, 39(6):1424–1439, 1994. Times Cited: 38 Cited Reference Count: 76 English Article LIMNOL OCEANOGR PP788.

[LCYL03] E. D. Levin, E. Chrysanthis, K. Yacisin, and E. Linney. Chlorpyrifos exposure of developing zebrafish: effects on survival and long-term effects on response latency and spatial discrimination. *Neurotoxicology and Teratology*, 25(1):51–57, 2003. Times Cited: 21 Cited Reference Count: 21 English Article NEUROTOXICOL TERATOL 661QN.

[LH97] Jane Lewis and Richard Hallett. Lingulodinium polyedrum (gonyaulax polyedra) a blooming dinoflagellate. *Oceanography and Marine Biology an Annual Review*, 35, 1997. Article English.

[LH99] P. H. Lenz and D. K. Hartline. Reaction times and force production during escape behavior of a calanoid copepod, undinula vulgaris. *Marine Biology*, 133(2):249–258, 1999. Times Cited: 27 Cited Reference Count: 64 English Article MAR BIOL 178ML.

[LHD00] P. H. Lenz, D. K. Hartline, and A. D. Davis. The need for speed. i. fast reactions and myelinated axons in copepods. *Journal of Comparative Physiology a-Neuroethology Sensory Neural and Behavioral Physiology*, 186(4):337–345, 2000. Times Cited: 25 Cited Reference Count: 46 English Article J COMP PHYSIOL A 320EK.

[LJ96] M. I. Latz and H. J. Jeong. Effect of red tide dinoflagellate diet and cannibalism on the bioluminescence of the heterotrophic dinoflagellates protoperidinium spp. *Marine Ecology-Progress Series*, 132(1-3):275–285, 1996. Times Cited: 12 Cited Reference Count: 33 English Article MAR ECOL-PROGR SER UD223.

[LJA+04] M. I. Latz, A. R. Juhl, A. M. Ahmed, S. E. Elghobashi, and J. Rohr. Hydrodynamic stimulation of dinoflagellate bioluminescence: a computational and experimental study. *Journal of Experimental Biology*, 207(11):1941–1951, 2004. Times Cited: 6 Cited Reference Count: 57 English Article J EXP BIOL 831CW.

[LKT+03] M. J. Levene, J. Korlach, S. W. Turner, M. Foquet, H. G. Craighead, and W. W. Webb. Zero-mode waveguides for single-molecule analysis at high concentrations. *Science*, 299(5607):682–686, 2003. Times Cited: 256.

[LKW+04] H. Lu, L. Y. Koo, W. C. M. Wang, D. A. Lauffenburger, L. G. Griffith, and K. F. Jensen. Microfluidic shear devices for quantitative analysis of cell adhesion. *Analytical Chemistry*, 76(18):5257–5264, 2004. Times Cited: 45 Cited Reference Count: 27 English Article ANAL CHEM 854UL.

[LL95] M. I. Latz and A. O. Lee. Spontaneous and stimulated bioluminescence of the dinoflagellate ceratocorys horrida (peridiniales). *Journal of Phycology*, 31(1):120–132, 1995. Times Cited: 23 Cited Reference Count: 62 English Article J PHYCOL QN482.

[LNR04] M. I. Latz, J. C. Nauen, and J. Rohr. Bioluminescence response of four species of dinoflagellates to fully developed pipe flow. *Journal of Plankton Research*, 26(12):1529–1546, 2004. Times Cited: 8 Cited Reference Count: 118 English Review J PLANKTON RES 900SB.

[LR99] M. I. Latz and J. Rohr. Luminescent response of the red tide dinoflagellate lingulodinium polyedrum to laminar and turbulent flow. *Limnology and Oceanography*, 44(6):1423–1435, 1999. Times Cited: 22 Cited Reference Count: 48 English Article LIMNOL OCEANOGR 229PA.

[LSBE03] E. A. Lipman, B. Schuler, O. Bakajin, and W. A. Eaton. Single-molecule measurement of protein folding kinetics. *Science*, 301(5637):1233–1235, 2003. Times Cited: 146.

[MB03] J. Moorthy and D. J. Beebe. In situ fabricated porous filters for microsystems. *Lab on a Chip*, 3(2):62–66, 2003.

[MBN+00] T. C. Merkel, V. I. Bondar, K. Nagai, B. D. Freeman, and I. Pinnau. Gas sorption, diffusion, and permeation in poly(dimethylsiloxane). *Journal of Polymer Science Part B-Polymer Physics*, 38(3):415–434, 2000. Times Cited: 147.

[MC92] A. F. Mensinger and J. F. Case. Dinoflagellate luminescence increases susceptibility of zooplankton to teleost predation. *Marine Biology*, 112(2):207–

210, 1992. Times Cited: 25 Cited Reference Count: 12 English Article MAR BIOL HC821.

[MD07] S. Mukhopadhyay and A. A. Deniz. Fluorescence from diffusing single molecules illuminates biomolecular structure and dynamics. *Journal of Fluorescence*, 17:775–783, 2007. Times Cited: 0.

[MDA+00] J. C. McDonald, D. C. Duffy, J. R. Anderson, D. T. Chiu, H. K. Wu, O. J. A. Schueller, and G. M. Whitesides. Fabrication of microfluidic systems in poly(dimethylsiloxane). *Electrophoresis*, 21(1):27–40, 2000. Times Cited: 724 Cited Reference Count: 80 English Review ELECTROPHORESIS 279VM.

[MESS05] M. M. Mielnik, R. P. Ekatpure, L. R. Saetran, and F. Schonfeld. Sinusoidal crossflow microfiltration device - experimental and computational flowfield analysis. *Lab on a Chip*, 5(8):897–903, 2005.

[MHVD+02] S. K. Mallipattu, M. A. Haidekker, P. Von Dassow, M. I. Latz, and J. A. Frangos. Evidence for shear-induced increase in membrane fluidity in the dinoflagellate lingulodinium polyedrum. *Journal of Comparative Physiology a-Neuroethology Sensory Neural and Behavioral Physiology*, 188(5):409–416, 2002. Times Cited: 12 Cited Reference Count: 35 English Article J COMP PHYSIOL A 579HV.

[ML07] E. M. Maldonado and M. I. Latz. Shear-stress dependence of dinoflagellate bioluminescence. *Biological Bulletin*, 212(3):242–249, 2007. Times Cited: 1 Cited Reference Count: 60 English Article BIOL BULL 180KI.

[MMS+07] G. Mehta, K. Mehta, D. Sud, J. W. Song, T. Bersano-Begey, N. Futai, Y. S. Heo, M. A. Mycek, J. J. Linderman, and S. Takayama. Quantitative measurement and control of oxygen levels in microfluidic poly(dimethylsiloxane) bioreactors during cell culture. *Biomedical Microdevices*, 9(2):123–134, 2007. Times Cited: 5.

[MO99] W. E. Moerner and M. Orrit. Illuminating single molecules in condensed matter. *Science*, 283(5408):1670–+, 1999. Times Cited: 454.

[Moe02] W. E. Moerner. A dozen years of single-molecule spectroscopy in physics, chemistry, and biophysics. *Journal of Physical Chemistry B*, 106(5):910–927, 2002. Times Cited: 163.

[Mor83] J. G. Morin. Coastal bioluminescence - patterns and functions. *Bulletin of Marine Science*, 33(4):787–817, 1983. Times Cited: 82 Cited Reference Count: 149 English Review BULL MAR SCI RZ119.

[MRS+99] A. D. Mehta, M. Rief, J. A. Spudich, D. A. Smith, and R. M. Simmons. Single-molecule biomechanics with optical methods. *Science*, 283(5408):1689–1695, 1999. Times Cited: 325.

[MS06] Marcos and R. Stocker. Microorganisms in vortices: a microfluidic setup. *Limnology and Oceanography-Methods*, 4:392–398, 2006. Times Cited: 0 Cited Reference Count: 27 English Article LIMNOL OCEANOGR-METHODS 121FC.

[MSS+06] D. J. Muller, K. T. Sapra, S. Scheuring, A. Kedrov, P. L. Frederix, D. Fotiadis, and A. Engel. Single-molecule studies of membrane proteins. *Current Opinion in Structural Biology*, 16(4):489–495, 2006. Times Cited: 33.

[MWJ06] X. Michalet, S. Weiss, and M. Jager. Single-molecule fluorescence studies of protein folding and conformational dynamics. *Chemical Reviews*, 106(5):1785–1813, 2006. Times Cited: 73.

[Net84] Durr G. Netzel, H. Dinoflagellare cell cortex. In D.L. Spector, editor, *Dinoflagellates*, pages 43–105. Academic Press, Orlando, Florida, 1984.

[NMBH91] M. T. Nicolas, D. Morse, J. M. Bassot, and J. W. Hastings. Colocalization of luciferin binding-protein and luciferase to the scintillons of gonyaulax-polyedra revealed by double immunolabeling after fast-freeze fixation. *Protoplasma*, 160(2-3):159–166, 1991. Times Cited: 24 Cited Reference Count: 30 English Article PROTOPLASMA FC295.

[NS79] T. Nawata and T. Sibaoka. Coupling between action potential and bioluminescence in noctiluca - effects of inorganic-ions and ph in vacuolar sap. *Journal of Comparative Physiology*, 134(2):137–149, 1979. Times Cited: 31 Cited Reference Count: 22 English Article J COMP PHYSIOL HX755.

[OW04] J. N. Onuchic and P. G. Wolynes. Theory of protein folding. *Current Opinion in Structural Biology*, 14(1):70–75, 2004.

[OW05] M. Oliveberg and P. G. Wolynes. The experimental survey of protein-folding energy landscapes. *Quarterly Reviews of Biophysics*, 38:245–288, 2005. Times Cited: 40.

[PF03] T. Preuss and D. S. Faber. Central cellular mechanisms underlying temperature-dependent changes in the goldfish startle-escape behavior. *Journal of Neuroscience*, 23(13):5617–5626, 2003. Times Cited: 19 Cited Reference Count: 53 English Article J NEUROSCI 697CF.

[PLF+05] N. J. Panaro, X. J. Lou, P. Fortina, L. J. Kricka, and P. Wilding. Micropillar array chip for integrated white blood cell isolation and pcr. *Biomolecular Engineering*, 21(6):157–162, 2005.

[PNG92] A. R. Pries, D. Neuhaus, and P. Gaehtgens. Blood-viscosity in tube flow - dependence on diameter and hematocrit. *American Journal of Physiology*, 263(6):H1770–H1778, 1992.

[PNH+05] F. Petersson, A. Nilsson, C. Holm, H. Jonsson, and T. Laurell. Continuous separation of lipid particles from erythrocytes by means of laminar flow and acoustic standing wave forces. *Lab on a Chip*, 5(1):20–22, 2005.

[Pol08] Gutierrez E. Levchenko A. Polinkovsky, M. *Lab on a Chip*, 2008.

[PQR+06] H. Y. Park, X. Y. Qiu, E. Rhoades, J. Korlach, L. W. Kwok, W. R. Zipfel, W. W. Webb, and L. Pollack. Achieving uniform mixing in a microfluidic device: Hydrodynamic focusing prior to mixing. *Analytical Chemistry*, 78(13):4465–4473, 2006. Times Cited: 15.

[RD95] S. G. Redkar and R. H. Davis. Cross-flow microfiltration with high-frequency reverse filtration. *Aiche Journal*, 41(3):501–508, 1995. Times Cited: 63 Cited Reference Count: 17 English Article AICHE J QN339.

[Rei94] W. H. Reinhart. Shear-dependence of endothelial functions. *Experientia*, 50(2):87–93, 1994. Times Cited: 40 Cited Reference Count: 88 English Review EXPERIENTIA MW476.

[RHFL02] J. Rohr, M. Hyman, S. Fallon, and M. I. Latz. Bioluminescence flow visualization in the ocean: an initial strategy based on laboratory experiments. *Deep-Sea Research Part I-Oceanographic Research Papers*, 49(11):2009–2033, 2002. Times Cited: 10 Cited Reference Count: 160 English Review DEEP-SEA RES PT I-OCEANOG RES 639FU.

[RLF+98] J. Rohr, M. I. Latz, S. Fallon, J. C. Nauen, and E. Hendricks. Experimental approaches towards interpreting dolphin-stimulated bioluminescence. *Journal of Experimental Biology*, 201(9):1447–1460, 1998. Times Cited: 31 Cited Reference Count: 80 English Article J EXP BIOL ZT233.

[RMH05] I. Rasnik, S. A. McKinney, and T. Ha. Surfaces and orientations: Much to fret about? *Accounts of Chemical Research*, 38(7):542–548, 2005. Times Cited: 33.

[RMH06] I. Rasnik, S. A. McKinney, and T. Ha. Nonblinking and longlasting single-molecule fluorescence imaging. *Nature Methods*, 3(11):891–893, 2006. Times Cited: 53.

[Rod02] B.F. Rodak. *Hematology: Clinical Principles and Applications*. W.B. Saunders, Philadelphia, 2nd edition, 2002.

[Roh99] Schoonmaker J. Losee J. Latz M.I. Hyman M. Rohr, J. Flow visualization in the ocean: implications of laboratory bioluminescence experiments. In *Oceans*, volume 1, pages 145–156. MTS/IEEE, 1999.

[RT92] D.C. Hohnadel R.F. Reiss R.C. Tilton, A. Balows. *Clinical Laboratory Medicine*. Mosby Year Bood, St. Louis, 1992.

[SAM+04] P. Sethu, M. Anahtar, L. L. Moldawer, R. G. Tompkins, and M. Toner. Continuous row microfluidic device for rapid erythrocyte lysis. *Analytical Chemistry*, 76(21):6247–6253, 2004.

[Sch05] B. Schuler. Single-molecule fluorescence spectroscopy of protein folding. *Chemphyschem*, 6(7):1206–1220, 2005. Times Cited: 50.

[SDA+02] A. D. Stroock, S. K. W. Dertinger, A. Ajdari, I. Mezic, H. A. Stone, and G. M. Whitesides. Chaotic mixer for microchannels. *Science*, 295(5555):647–651, 2002. Times Cited: 676 Cited Reference Count: 16 English Article SCIENCE 516PD.

[SDLR04] M. D. Stokes, G. B. Deane, M. I. Latz, and J. Rohr. Bioluminescence imaging of wave-induced turbulence. *Journal of Geophysical Research-Oceans*, 109(C1), 2004. Times Cited: 6 Cited Reference Count: 28 English Article J GEOPHYS RES-OCEANS 765LD.

[SF00] K. S. Seo and L. Fritz. Cell-wall morphology correlated with vertical migration in the non-motile marine dinoflagellate pyrocystis noctiluca. *Marine Biology*, 137(4):589–594, 2000. Times Cited: 7 Cited Reference Count: 30 English Article MAR BIOL 376CJ.

[SFJ+03] A. B. Singleton, M. Farrer, J. Johnson, A. Singleton, S. Hague, J. Kachergus, M. Hulihan, T. Peuralinna, A. Dutra, R. Nussbaum, S. Lincoln, A. Crawley, M. Hanson, D. Maraganore, C. Adler, M. R. Cookson, M. Muenter, M. Baptista, D. Miller, J. Blancato, J. Hardy, and K. Gwinn-Hardy. alpha-synuclein locus triplication causes parkinson's disease. *Science*, 302(5646):841–841, 2003. Times Cited: 685.

[SG05] C. Simonnet and A. Groisman. Chaotic mixing in a steady flow in a microchannel. *Physical Review Letters*, 94(13), 2005. Times Cited: 12 Cited Reference Count: 21 English Article PHYS REV LETT 915HN.

[SGF+05] J. W. Song, W. Gu, N. Futai, K. A. Warner, J. E. Nor, and S. Takayama. Computer-controlled microcirculatory support system for endothelial cell culture and shearing. *Analytical Chemistry*, 77(13):3993–3999, 2005. Times Cited: 28 Cited Reference Count: 28 English Article ANAL CHEM 942GL.

[SGJ+04] U. Seger, S. Gawad, R. Johann, A. Bertsch, and P. Renaud. Cell immersion and cell dipping in microfluidic devices. *Lab on a Chip*, 4(2):148–151, 2004.

[Ska87] Chien S. Skalak, R. *Handbook of Bioengineering*. McGraw-Hill, New York, New York, 1987.

[SM00] H. Schmid and B. Michel. Siloxane polymers for high-resolution, high-accuracy soft lithography. *Macromolecules*, 33(8):3042–3049, 2000.

[SMM+06a] P. Sethu, L. L. Moldawer, M. N. Mindrinos, P. O. Scumpia, C. L. Tannahill, J. Wilhelmy, P. A. Efron, B. H. Brownstein, R. G. Tompkins, and M. Toner. Microfluidic isolation of leukocytes from whole blood for phenotype and gene expression analysis. *Analytical Chemistry*, 78(15):5453–5461, 2006.

[SMM+06b] D. Sud, G. Mehta, K. Mehta, J. Linderman, S. Takayama, and M. A. Mycek. Optical imaging in microfluidic bioreactors enables oxygen monitoring for continuous cell culture. *Journal of Biomedical Optics*, 11(5), 2006. Times Cited: 2.

[SMR+05] A. Sin, S. K. Murthy, A. Revzin, R. G. Tompkins, and M. Toner. Enrichment using antibody-coated microfluidic chambers in shear flow: Model mixtures of human lymphocytes. *Biotechnology and Bioengineering*, 91(7):816–826, 2005.

[SP01] M. Sharan and A. S. Popel. A two-phase model for flow of blood in narrow tubes with increased effective viscosity near the wall. *Biorheology*, 38(5-6):415–428, 2001.

[Spe84] D.L. Spector. *Dinoflagellates*. Academic Press, San Diego, California, 1984.

[SPRR98] S. M. Stufflebeam, D. Poeppel, H. A. Rowley, and T. P. L. Roberts. Peri-threshold encoding of stimulus frequency and intensity in the m100 latency. *Neuroreport*, 9(1):91–94, 1998. Times Cited: 37 Cited Reference Count: 24 English Article NEUROREPORT YR471.

[SQ05] T. M. Squires and S. R. Quake. Microfluidics: Fluid physics at the nanoliter scale. *Reviews of Modern Physics*, 77(3):977–1026, 2005. Times Cited: 403 Cited Reference Count: 678 English Review REV MOD PHYS 972HB.

[SR70] E. Swift and C. C. Remsen. Cell wall of pyrocystis spp (dinococcales). *Journal of Phycology*, 6(1):79, 1970. Times Cited: 29 Cited Reference Count: 51 English Article J PHYCOL G0290.

[SSA04] H. A. Stone, A. D. Stroock, and A. Ajdari. Engineering flows in small devices: Microfluidics toward a lab-on-a-chip. *Annual Review of Fluid Mechanics*, 36:381–411, 2004. Times Cited: 513 Cited Reference Count: 150 English Review ANNU REV FLUID MECH 775LT.

[SST06] P. Sethu, A. Sin, and M. Toner. Microfluidic diffusive filter for apheresis (leukapheresis). *Lab on a Chip*, 6(1):83–89, 2006.

[Sta66] RF Staples. The distribution and characteristics of surface bioluminescence in teh oceans. Technical report, Naval Oceanography Office, 1966.

[SW03] S. K. Sia and G. M. Whitesides. Microfluidic devices fabricated in poly(dimethylsiloxane) for biological studies. *Electrophoresis*, 24(21):3563–3576, 2003. Times Cited: 285 Cited Reference Count: 81 English Review ELECTROPHORESIS 748JL.

[Swe86] B. M. Sweeney. The loss of the circadian-rhythm in photosynthesis in an old strain of gonyaulax-polyedra. *Plant Physiology*, 80(4):978–981, 1986. Times Cited: 7 Cited Reference Count: 12 English Article PLANT PHYSIOL C1046.

[SYMB05] S. S. Shevkoplyas, T. Yoshida, L. L. Munn, and M. W. Bitensky. Biomimetic autoseparation of leukocytes from whole blood in a microfluidic device. *Analytical Chemistry*, 77(3):933–937, 2005.

[Tet71] P. B. Tett. Relation between dinoflagellates and bioluminescence of sea water. *Journal of the Marine Biological Association of the United Kingdom*, 51(1):183, 1971. Times Cited: 28 Cited Reference Count: 40 English Article J MAR BIOL ASSN UK I5649.

[TI05] M. Toner and D. Irimia. Blood-on-a-chip. *Annual Review of Biomedical Engineering*, 7:77–103, 2005.

[TL07] T. Torres and M. Levitus. Measuring conformational dynamics: A new fcs-fret approach. *Journal of Physical Chemistry B*, 111(25):7392–7400, 2007. Times Cited: 7.

[TMLO00] P. Tamarat, A. Maali, B. Lounis, and M. Orrit. Ten years of single-molecule spectroscopy. *Journal of Physical Chemistry A*, 104(1):1–16, 2000. Times Cited: 160.

[TYO+06] Y. Tanaka, M. Yamato, T. Okano, T. Kitamori, and K. Sato. Evaluation of effects of shear stress on hepatocytes by a microchip-based system. *Measurement Science and Technology*, 17(12):3167–3170, 2006. Times Cited: 10 Cited Reference Count: 12 English Article MEAS SCI TECHNOL 112LW.

[UCT+00] M. A. Unger, H. P. Chou, T. Thorsen, A. Scherer, and S. R. Quake. Monolithic microfabricated valves and pumps by multilayer soft lithography. *Science*, 288(5463):113–116, 2000. Times Cited: 776 Cited Reference Count: 35 English Article SCIENCE 302VT.

[UF02] V. N. Uversky and A. Fink. Amino acid determinants of alpha-synuclein aggregation: putting together pieces of the puzzle. *Febs Letters*, 522(1-3):9–13, 2002. Times Cited: 33 Cited Reference Count: 54 English Review FEBS LETT 571BU.

[vDBL05] P. von Dassow, R. N. Bearon, and M. I. Latz. Bioluminescent response of the dinoflagellate lingulodinium polyedrum to developing flow: Tuning of sensitivity and the role of desensitization in controlling a defensive behavior of a planktonic cell. *Limnology and Oceanography*, 50(2):607–619, 2005. Times Cited: 5 Cited Reference Count: 41 English Article LIMNOL OCEANOGR 909BZ.

[vDL02] P. von Dassow and M. I. Latz. The role of ca2+ in stimulated bioluminescence of the dinoflagellate lingulodinium polyedrum. *Journal of Experimental Biology*, 205(19):2971–2986, 2002. Times Cited: 8 Cited Reference Count: 58 English Article J EXP BIOL 604ZZ.

[VG06] V. VanDelinder and A. Groisman. Separation of plasma from whole human blood in a continuous cross-flow in a molded microfluidic device. *Analytical Chemistry*, 78(11):3765–3771, 2006.

[VKS+08] J. Vogelsang, R. Kasper, C. Steinhauer, B. Person, M. Heilemann, M. Sauer, and P. Tinnefeld. A reducing and oxidizing system minimizes photobleaching and blinking of fluorescent dyes. *Angewandte Chemie-International Edition*, 47(29):5465–5469, 2008. Times Cited: 3.

[Vog81] S. Vogel. *Life moving fluids*. 1981.

[VPGT05] A. P. Vollmer, R. F. Probstein, R. Gilbert, and T. Thorsen. Development of an integrated microfluidic platform for dynamic oxygen sensing and delivery in a flowing medium. *Lab on a Chip*, 5(10):1059–1066, 2005. Times Cited: 13.

[VTdJ05] H. J. Vermeer, E. Thomassen, and N. de Jonge. Automated processing of serum indices used for interference detection by the laboratory information system. *Clinical Chemistry*, 51(1):244–247, 2005.

[WC81] E. A. Widder and J. F. Case. 2 flash forms in the bioluminescent dinoflagellate, pyrocystis-fusiformis. *Journal of Comparative Physiology*, 143(1):43–52, 1981. Times Cited: 25 Cited Reference Count: 17 English Article J COMP PHYSIOL LW864.

[WDHL00] T. M. Weatherby, A. D. Davis, D. K. Hartline, and P. H. Lenz. The need for speed. ii. myelin in calanoid copepods. *Journal of Comparative Physiology a-Sensory Neural and Behavioral Physiology*, 186(4):347–357, 2000. Times Cited: 18 Cited Reference Count: 37 English Article J COMP PHYSIOL A 320EK.

[Wei99] S. Weiss. Fluorescence spectroscopy of single biomolecules. *Science*, 283(5408):1676–1683, 1999. Times Cited: 827.

[Wei00] S. Weiss. Measuring conformational dynamics of biomolecules by single molecule fluorescence spectroscopy. *Nature Structural Biology*, 7(9):724–729, 2000. Times Cited: 240.

[WG04] Maxwell Myer Wintrobe and John P. Greer. *Wintrobe's clinical hematology.* Lippincott Williams and Wilkins, Philadelphia, 11th edition, 2004.

[WH98] T. Wilson and J. W. Hastings. Bioluminescence. *Annual Review of Cell and Developmental Biology*, 14:197–230, 1998. Times Cited: 172 Cited Reference Count: 163 English Review ANNU REV CELL DEV BIOL 147CX.

[Whi79] H. H. White. Effects of dinoflagellate bioluminescence on the ingestion rates of herbivorous zooplankton. *Journal of Experimental Marine Biology and Ecology*, 36(3):217–224, 1979. Times Cited: 40 Cited Reference Count: 22 English Article J EXP MAR BIOL ECOL GK064.

[Whi91] F.M. White. *Viscous fluid flow.* McGraw-Hill, New York, 1991.

[Whi06] G. M. Whitesides. The origins and the future of microfluidics. *Nature*, 442(7101):368–373, 2006. Times Cited: 283 Cited Reference Count: 65 English Editorial Material NATURE 067CI.

[Wid81] Case J.F. Widder, E. A. Bioluminescence excitation in a dinoflagellate. In K.H. Nealson, editor, *Bioluminescence Current Perspectives*, pages 125–132. Burgess Publishing, Minneapolis, Minnesota, 1981.

[WK72] J. J. Wine and F. B. Krasne. Organization of escape behavior in crayfish. *Journal of Experimental Biology*, 56(1):1, 1972. Times Cited: 216 Cited Reference Count: 37 English Article J EXP BIOL L9176.

[WKC+98] P. Wilding, L. J. Kricka, J. Cheng, G. Hvichia, M. A. Shoffner, and P. Fortina. Integrated cell isolation and polymerase chain reaction analysis using silicon microfilter chambers. *Analytical Biochemistry*, 257(2):95–100, 1998.

[WMG62] R. E. Wells, E. W. Merrill, and H. Gabelnick. Shear-rate dependence of viscosity of blood - interaction of red cells and plasma proteins. *Transactions of the Society of Rheology*, 6:19–24, 1962.

[WW02] R. J. Wakeman and C. J. Williams. Additional techniques to improve microfiltration. *Separation and Purification Technology*, 26(1):3–18, 2002.

[WZP+96] P. H. Weinreb, W. G. Zhen, A. W. Poon, K. A. Conway, and P. T. Lansbury. Nacp, a protein implicated in alzheimer's disease and learning, is natively unfolded. *Biochemistry*, 35(43):13709–13715, 1996. Times Cited: 508 Cited Reference Count: 41 English Article BIOCHEMISTRY-USA VP990.

[XW98] Y. N. Xia and G. M. Whitesides. Soft lithography. *Annual Review of Materials Science*, 28:153–184, 1998.

[YEF+06] P. Yager, T. Edwards, E. Fu, K. Helton, K. Nelson, M. R. Tam, and B. H. Weigl. Microfluidic diagnostic technologies for global public health. *Nature*, 442(7101):412–418, 2006. Times Cited: 99 Cited Reference Count: 59 English Review NATURE 067CI.

[YS05] M. Yamada and M. Seki. Hydrodynamic filtration for on-chip particle concentration and classification utilizing microfluidics. *Lab on a Chip*, 5(11):1233–1239, 2005.

[ZAN+06] R. Zhao, J. F. Antaki, T. Naik, T. N. Bachman, M. V. Kameneva, and Z. J. J. Wu. Microscopic investigation of erythrocyte deformation dynamics. *Biorheology*, 43(6):747–765, 2006. Times Cited: 4 Cited Reference Count: 38 English Article BIORHEOLOGY 120KR.

[ZC82] A. L. Zydney and C. K. Colton. Continuous-flow membrane plasmapheresis - theoretical-models for flux and hemolysis prediction. *Transactions American Society for Artificial Internal Organs*, 28:408–412, 1982.

[ZD88] M. J. Zoran and C. D. Drewes. The rapid tail withdrawal reflex of the tubificid worm, branchiura-sowerbyi. *Journal of Experimental Biology*, 137:487–

500, 1988. Times Cited: 8 Cited Reference Count: 21 English Article J EXP BIOL P3568.